Estimation of population receptive fields in human visual and auditory cortex

Kelly Chang

A dissertation
submitted in partial fulfillment of the
requirements for the degree of

Doctor of Philosophy

University of Washington

2022

Reading Committee:
Geoffrey M. Boynton, Chair
Ione Fine
John Pyles

Program Authorized to Offer Degree:
Psychology

University of Washington

Abstract

Estimation of population receptive fields
in human visual and auditory cortex

Kelly Chang

Chair of the Supervisory Committee:
Title of Chair Geoffrey M. Boynton
Psychology

Topographical organization is a foundation principle of human sensory cortices where the sensory neurons encode information from the physical world into orderly representational maps along sensory-specific dimensions. The visual system encodes spatial positions of the visual field, and the auditory system encodes the frequency of sounds. The representational maps are known as retinotopy and tonotopy, respectively. The population receptive field (pRF) model is a computational framework used to characterize the functional organization of sensory cortices. It is a popular method and has various applications in human neuroimaging research. In this dissertation, I demonstrate how the pRF model can be used to investigate various research interests. First, I use the pRF model as an encoding and decoding model of frequency in primary auditory cortex. Second, I examine neural plasticity in auditory cortex due to long-term visual deprivation by comparing pRF estimates of early blind individuals with normally sighted individuals. Third, I develop a novel stimulus protocol that increases reliability and minimize biases in pRF estimates of human visual cortex. Together, these studies demonstrate the applications of the pRF model as a powerful tool capable of understanding a wide range of phenomena in human sensory cortices.

TABLE OF CONTENTS

Page

List of Figures iv

List of Tables vi

Chapter 1: Introduction 1
1.1 Vision and Retinotopic Organization 1
1.2 Functional Magnetic Resonance Imaging 3
1.3 Phase-encoded Mapping 5
1.4 Population Receptive Field (pRF) Model 7
1.5 Audition and Tonotopic Organization 8
1.6 pRF Model Applications 12
1.7 Outline 14

Chapter 2: Reconstructing Tone Sequences from fMRI BOLD Responses within Human Primary Auditory Cortex 16
2.1 Introduction 16
2.2 Materials and Methods 18
2.2.1 MRI Data Acquisition and Analysis 19
2.2.2 Auditory Stimulus Presentation 20
2.2.3 pRF Estimation 20
2.2.4 Frequency Decoding 23
2.3 Results 25
2.4 Discussion 28
2.4.1 Encoding/Decoding Models of Sensory Cortex 28

Chapter 3: Early Blindness Shapes Cortical Representations of Auditory Frequency within Auditory Cortex 33

3.1 Introduction . . . 33
3.2 Materials and Methods . . . 34
3.2.1 Participants . . . 34
3.2.2 MRI . . . 35
3.2.3 Acquisition Protocol . . . 35
3.2.4 Auditory Stimulus Creation . . . 36
3.2.5 Auditory Stimulus and Task . . . 36
3.2.6 MR Data Preprocessing . . . 37
3.2.7 ROI Selection . . . 38
3.2.8 Population Receptive Field Analysis . . . 39
3.2.9 Statistical Analyses . . . 40
3.3 Results . . . 42
3.3.1 Auditory Cortex Size . . . 42
3.3.2 HRFs . . . 44
3.3.3 Response Amplitudes . . . 45
3.3.4 pRF Model Response Amplitudes . . . 45
3.3.5 Frequency Distributions . . . 47
3.3.6 Tuning Width . . . 49
3.4 Discussion . . . 53
3.4.1 Auditory Cortex Size . . . 53
3.4.2 Response Amplitudes . . . 54
3.4.3 Frequency Distributions . . . 55
3.4.4 Tuning Width . . . 55

Chapter 4: Optimizing Reliability and Measurement of Population Receptive Fields in Human Visual Cortex . . . 57
4.1 Introduction . . . 57
4.2 Methods . . . 60
4.2.1 Subjects . . . 60
4.2.2 MRI Acquisition . . . 61
4.2.3 Preprocessing . . . 61
4.2.4 Stimuli . . . 63
4.2.5 pRF Analysis . . . 65

4.2.6 pRF Size and Cortical Magnification Factor . . . 68
4.2.7 pRF Model Simulations . . . 69
4.2.8 Behavioral Analysis . . . 70
4.3 Results . . . 71
4.3.1 pRF Cortical Maps . . . 71
4.3.2 pRF Estimate Reliability . . . 71
4.3.3 Frequency of Estimated pRFs . . . 76
4.3.4 Effect of Stimulus Type on pRF Parameter Estimates . . . 77
4.3.5 pRF Size, Cortical Magnification Factor, and Eccentricity . . . 81
4.3.6 pRF Size Comparison as a Function of Eccentricity . . . 84
4.3.7 Variance Explained as a Function of Eccentricity . . . 85
4.3.8 pRF Simulations . . . 86
4.4 Discussion . . . 88
4.4.1 pRF Estimate Reliability . . . 88
4.4.2 pRF Estimate Differences by Stimulus Type . . . 89
4.4.3 Limitations . . . 90
4.4.4 Conclusion . . . 91

References . . . 92

Appendix A: Subject Information Tables . . . 114

Appendix B: ANOVA Tables . . . 117

LIST OF FIGURES

Figure Number		Page
1.1	Receptive fields of V1, V2, and V3 neurons in Macaque.	2
1.2	Linear properties of the HRF.	5
1.3	Retinotopic maps acquired from the phase-encoded method.	6
1.4	Flow chart of the pRF model estimation procedure	7
1.5	Retinotopic maps acquired from pRF model estimation.	9
1.6	Tonotopic maps from phase-encoded and pRF methods.	11
2.1	Tonotopic population receptive field (pRF) estimation	21
2.2	Tone identification performance	26
2.3	Tone sequence reconstruction	28
2.4	Histograms of voxel $rRMSE$ values for song-like sequences	29
3.1	Tonotopic maps in auditory cortex	43
3.2	Response amplitudes in auditory areas	46
3.3	The proportion of voxels successfully fit by frequency	48
3.4	Tuning width maps in auditory cortex	50
3.5	Mean pRF tuning width for within PAC	52
4.1	Example frames of fixed-bar and log-bar stimulus movies	64
4.2	Retinotopic maps of pRF parameters across stimulus types	72
4.3	pRF estimate intersession reliability in the foveal confluence and V1	73
4.4	pRF estimate intersession reliability in V2 and V3	74
4.5	pRF estimate intersession reliability by stimulus and visual areas	75
4.6	Difference in pRF polar angle estimates across visual areas	78
4.7	Difference in pRF eccentricity estimates across visual areas	78
4.8	Difference in pRF size estimates across visual areas	79
4.9	Difference in variance explained across visual areas	79

4.10 pRF size, cortical magnification factor, and population point image as a function of eccentricity 82
4.11 pRF size ratio as a function of eccentricity across visual areas 84
4.12 Variance explained as a function of eccentricity across visual areas 85
4.13 Simulated pRF size estimate comparisons to ground truth 87

LIST OF TABLES

Table Number Page

2.1 Tone sequence reconstruction accuracy 27

4.1 Summary of pRF estimate intersession reliability 75
4.2 Summary of pRF size and CMF equation parameters 83

A.1 Chaper 3 Subject demographics and clinical descriptions 115
A.2 Subject HRF parameters for Chaper 4 116

B.1 Intersession reliability of pRF estimates ANOVA table 118
B.2 Number of estimated pRFs ANOVA table 119
B.3 Difference in pRF estimates (fixed-bar – log-bar) ANOVA table 120
B.4 pRF size equation parameters by eccentricity and pRF size at 1° ANOVA table 121
B.5 CMF equation parameters by eccentricity and CMF size at 1° ANOVA table 122

DEDICATION

to my better half, Patrick

Chapter 1
INTRODUCTION

1.1 Vision and Retinotopic Organization

The visual world is complex and difficult to navigate, so an important signal that the human visual system needs to preserve is the spatial arrangement of the visual world. Spatial arrangement refers to the relationship between one portion in visual space relative to another position. The visual system preserves the scene's spatial layout, like a map that links the visual world with an internal biological representation. The visual system's organizational principle that maintains the spatial arrangement of the visual world is called retinotopic organization.

As the name implies, retinotopic organization starts in the retina. For humans, vision originates when an external source of light (i.e., the sun) emits light that is then reflected when it meets a surface or object in the physical world. The reflected light will be detected by photoreceptors in the human eye. Photoreceptors are specialized neurons located at the back of the human eye in the retina that activate in response to light. Photoreceptors tile the retina and encode spatial information based on where in the retina the photoreceptor is located. This signal propagates throughout the entire visual system where it eventually goes to visual cortex.

The interest in retinotopic mapping dates to case studies over a century ago that investigated visual field loss due to gunshot wounds that damaged visual cortex (Holmes, 1918; Lister & Holmes, 1916). The studies correlated the location of visual field loss with the damaged cortex location of multiple patients to draw the conclusion that there was a systematic mapping of the visual field to cortical location. Astoundingly, these studies were able to localize visual representations to the calcarine sulcus, where we now know primary visual

cortex (V1) resides.

Electrophysiological measurements in animals also advanced the understanding of retinotopic mapping. These studies presented stimuli that covered parts of the visual field and measured single- or multi-unit responses from early visual cortex. Retinotopic organization was examined by correlating each neuron's location in cortical space with the portion of visual space that evoked activity. The spatial extent in visual space that a neuron was responsive to is called the neuron's receptive field (RF). RFs are the units used to establish the link between the physical world and neural computations. By identifying a collection of neuronal RFs, it was possible to create retinotopic maps of preferred location in visual space (Figure 1.1).

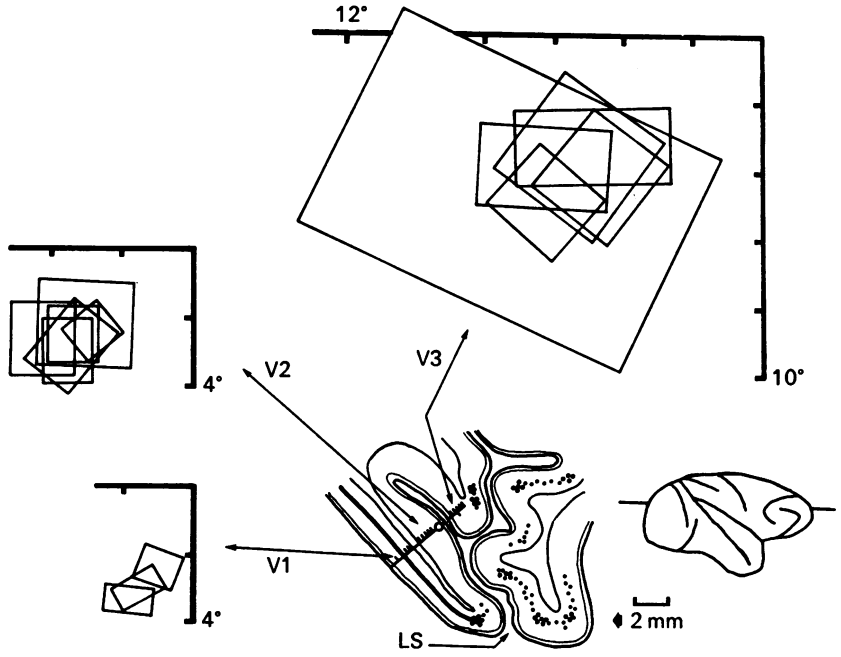

Figure 1.1: Receptive fields of V1, V2, and V3 neurons in Macaque. Image shows the relationship between recording site and RF representation of visual space. From Van Essen et al. (1984).

Next, was to consider the neuronal population response. It was possible that neuronal RFs properties would not translate to population level properties since it was unclear how signals from multiple cells would combine. Victor et al. (1994) demonstrated that population

responses were evoked by different spatial locations and orientations. Not only was the population responsive, but they were also tuned to these stimulus properties. Thus, establishing that neuronal populations also had receptive fields, or a population receptive field (pRF; Victor et al., 1994). This implied that RF properties carried over into the pRF properties.

Animal work provided the foundation for understanding retinotopic organization in humans once human-viable neural recording methods began to emerge. At the time, evidence of human retinotopic organization research was limited to electrocorticography (ECoG; Brindley & Lewin, 1968; Dobelle et al., 1979) and positron emission tomography (PET; Fox et al., 1987). ECoG measurements are collected from cerebrally implanted electrodes in surgery patients, which severely limited the sample population. Whereas PET studies were more accessible and could anatomically localize human visual cortex along with functional activation to visual stimuli. However, PET had poor signal-to-noise and poor spatial resolution. Fox et al. (1987) had to average the brains of six subjects and were only able to demonstrate broad activation in early visual cortex.

1.2 Functional Magnetic Resonance Imaging

By the early 1990s, magnetic resonance imaging (MRI) was gaining traction as a viable neuroimaging technology for human research. MRI is a noninvasive neuroimaging method that relies on differences in magnetic properties of tissue matter to generate images. Anatomical images of human tissue, like the brain, are collected as a series of 2D images, which when collated, reconstruct a 3-dimensional volume. Each voxel, or volumetric pixel, of the 3D volume could be reconstructed at higher resolution ($\sim$ 1-5 mm^3) as compared to PET ($\sim$ 10-15 mm^3). Nearly a century later, Horton and Hoyt (1991) used anatomical MRIs to compare visual field deficits in patients with visual cortex lesions to refine the original visual fields maps drawn by Lister and Holmes (1916). For anatomical images, MRI reconstruction algorithms emphasize the difference in magnetic properties of hydrogen because its produces images with high contrast between grey matter (neuronal cell bodies) and white matter (myelinated axons).

Ogawa et al. examined the relationship between blood oxygen levels and neuronal activity using MRI (Ogawa & Lee, 1990; Ogawa, Lee, Kay, et al., 1990; Ogawa, Lee, Nayak, et al., 1990). Their work showed that neuronal activity was followed by an increase in blood flow due to the additionally energy demand required for active neuronal activity. Blood can be considered to exist in two states, oxygenated or deoxygenated, based on its hemoglobin protein. In its oxygenated state, oxyhemoglobin contains oxygen molecules that provide cellular energy. As activity increases, neurons use oxygen from the oxyhemoglobin. This transforms the protein into its deoxygenated state, deoxyhemoglobin. Ogawa et al. demonstrated that by contrasting the relative difference in magnetic properties of oxyhemoglobin and deoxyhemoglobin, an MRI could acquire a signal that represented the changes in blood flow over time. The signal is called the blood-oxygen-level-dependent (BOLD) response and is an implicit measure of neuronal activity. The BOLD response is the foundation of modern functional magnetic resonance imaging (fMRI).

When an impulse, or brief stimulus, is presented, the resulting BOLD response takes a canonical form of a delayed increase from baseline cerebral blood levels, followed by a gradual decrease below baseline levels. The HRF has been described with the difference of two gamma functions (Friston et al., 1998) and systems of differential equations (Friston et al., 2000). But simply, the HRF approximates the form of a gamma distribution function (Boynton et al., 1996). Previous work demonstrated that the HRF behaves in a near-linear manner in response to stimulus input in human visual cortex (Boynton et al., 1996). This meant that stimuli at different strengths would produce similarly scaled HRFs. Different stimuli would each elicit an HRF that would add together to produce the BOLD response. Figure 1.2 shows the scaling and additivity properties of the HRF. By validating the properties of the HRF, statistical analyses that heavily depend on system linearity could be used moving forward to examine fMRI data.

MRI technology became a power tool for research on the human brain.

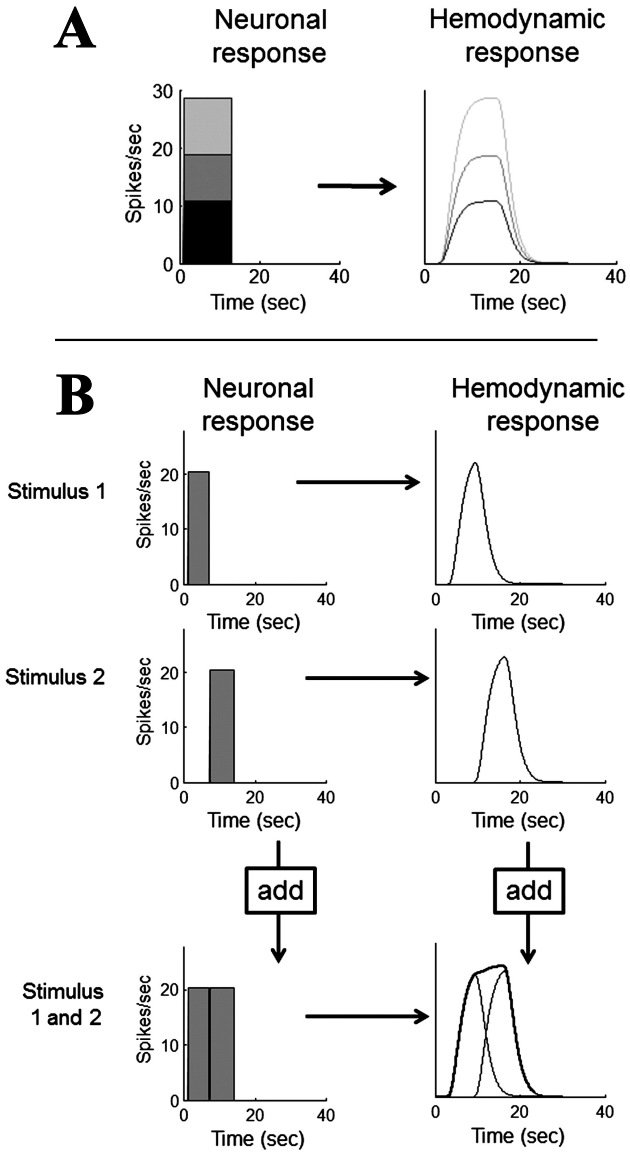

Figure 1.2: Linear properties of the HRF. (A) Scaling. (B) Additivity. Adapted from Boynton et al. (2012).

Anatomical MRI had good spatial resolution ($\sim$ 1-5 mm^3) so identifying distinct cortical morphology became possible and fMRI was able to measure functional responses over time ($\sim$ 0.5 Hz). When combined, fMRI signals could be sourced to anatomical locations in an individual's brain with high spatial specificity.

1.3 Phase-encoded Mapping

Using fMRI, research could investigate the retinotopic organization in human visual cortex. This led to the development of phase-encoded retinotopic stimuli to perform retinotopic mapping (DeYoe et al., 1994; Engel et al., 1994). Based on animal work, if specific portions of visual space contain stimuli, then corresponding regions of visual cortex would activate in response to the stimulation. Additionally, the fMRI signal would also match stimulus behavior because of the linear properties of the BOLD response. Engel et al. (1994) used a checkerboard stimulus shaped like a ring in visual space that expanded from the fovea to the periphery in a sinusoidal pattern. Given that stimulus behavior was known to start at the fovea and move to the periphery, the best phase offset of the BOLD response would correspond to central or peripheral parts of the visual field. This revealed the retinotopic organization of visual space eccentricity in human visual

cortex. Similarly, DeYoe et al. (1994) and Engel et al. (1997) used a checkerboard stimulus shaped like a wedge that rotated about the center of the visual field and the phase-encoded method to map the retinotopic organization of polar angle in human visual cortex. Using phase-encoded retinotopic mapping, it became possible to identify and delineate early visual cortex in V1, V2, and V3 based on polar angle representation (Figure 1.3; DeYoe et al., 1994; Engel et al., 1997; Sereno et al., 1995).

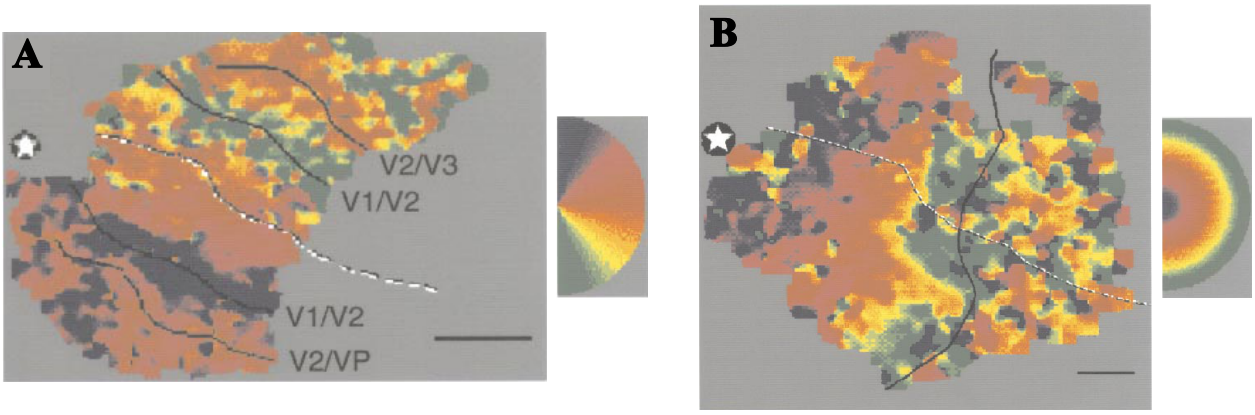

Figure 1.3: Retinotopic maps acquired from the phase-encoded method. (A) Polar angle map with black lines indicating the visual area boundaries. (B) Eccentricity map with the black line indicating region beyond the display. The star icon indicates the occipital pole, the dashed line indicated the calcarine sulcus. Adapted from Engel et al. (1997).

However, the phase-encoded analysis is a coarse measure of retinotopic organization. A more complete description of retinotopic organization would include identifying the most effective visual field position for each cortical location (Wandell et al., 2007). The phase-encoding method is only able to match the visual locations available within the presented stimulus set. While it would be possible to increase the stimulus set, the increased fMRI acquisition time would be too costly to justify multiple runs of minutely varying stimuli. This meant that the phase-encoded method was unable to precisely estimate the extent, or size, of the voxel's responsivity in visual space. Also, phase-encoding method estimated a phase delay to match the stimulus position and the BOLD response. If the

phase delay was miscalculated, this would result in shifted retinotopic maps. Another method would be required to fully characterize retinotopic maps in human visual cortex.

1.4 Population Receptive Field (pRF) Model

The population receptive field (pRF) model is a computational framework that defines the BOLD response as a combination of stimulus dynamics, pRF properties, and hemodynamics (Dumoulin & Wandell, 2008). The pRF model belongs to a class of encoding models that predict voxel-wise fMRI activity as evoked by a parameterized stimulus (Naselaris et al., 2011).

The pRF model assumes that each voxel's pRF has a preferred location in visual space that is differentially selective within its preferred location. The function that best describe this selectivity, or tuning, is a 2-dimension Gaussian. A 2D Gaussian is parameterized by its center and size

$$g\left(x,y\right)=\exp\left(-\left(\frac{\left(x-x_0\right)^2+\left(y-y_0\right)^2}{2\sigma^2}\right)\right) \tag{1.1}$$

where x_0 and y_0 represent the center in visual space and σ is the standard deviation. The stimulus is also parameterized in visual

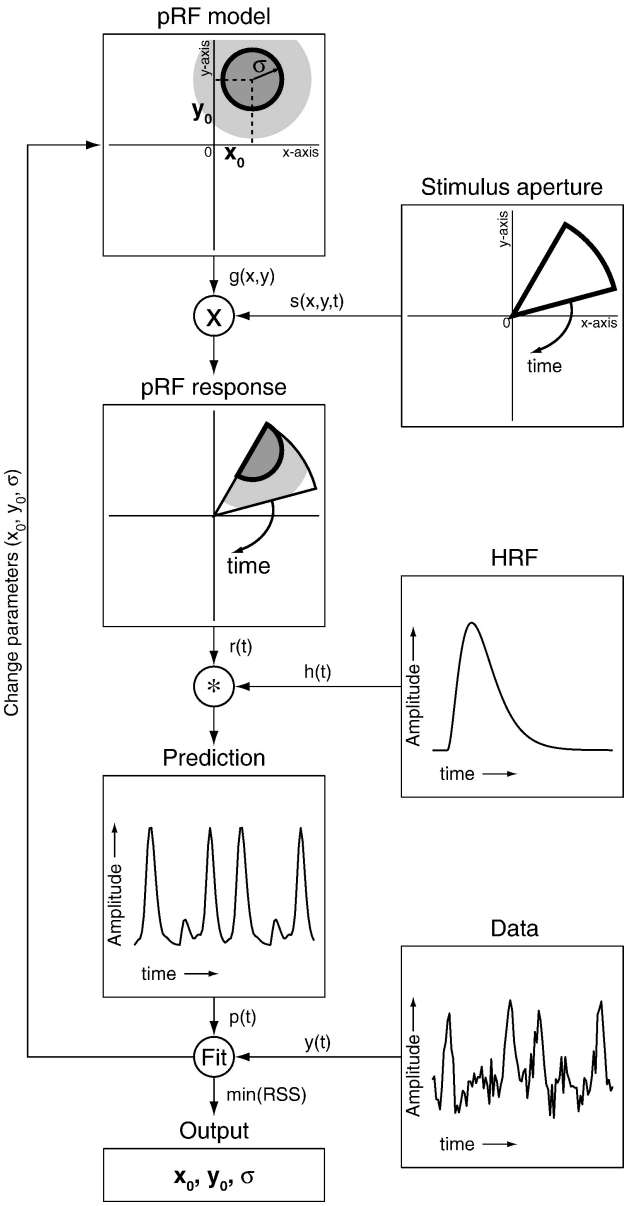

Figure 1.4: Flow chart of the pRF model estimation procedure. The pRF model is estimated for every voxel independently. From Dumoulin and Wandell (2008).

space over time as $s(x, y, t)$ where the stimulus can be either be present (1) or absent (0) at each visual location. By taking advantage of the near-linear properties of the BOLD response (Boynton et al., 1996), the pRF model defines the fMRI response, $r(t)$, in visual cortex to be the linear sum of the stimulus time course and a voxel's pRF convolved with the hemodynamic response function, $h(t)$. This can be formally stated as

$$r(t) = s(x, y, t)\, g(x, y) \circledast h(t) \tag{1.2}$$

The pRF model estimates the x_0, y_0, and σ parameters that minimizes the difference between the model predicted fMRI time course ($r(t)$, from Equation 1.2) and acquired BOLD responses from individuals. The pRF model and estimation procedure is outlined in Figure 1.4, which shows the original pRF model estimation pipeline from Dumoulin and Wandell (2008).

The estimated pRF location parameters, x_0 and y_0, are transformed into polar coordinates representing polar angle and eccentricity, where, with the pRF size parameter σ, are interpreted to be the maps that collectively describe retinotopic organization of human visual cortex (Figure 1.5). Dumoulin and Wandell (2008) demonstrated the pRF model produced location estimates on par with the phase-encoded method and produced an additional pRF size parameter. Furthermore, a corollary of Equation 1.2 was that the stimulus could now take any form. This marks is a striking difference from phase-encoded mapping procedure where stimuli were required to vary sinusoidally.

1.5 Audition and Tonotopic Organization

The notion that sensory systems are selective for aspects of their respective domain specific spaces is not unique to vision. While the definition of RFs may have come from vision, the definition can be generalized to be a specific region of sensory space that an appropriate stimulus would drive a response from a sensory neuron. Audition is another sensory modality where extensive research has been conducted on its functional organization.

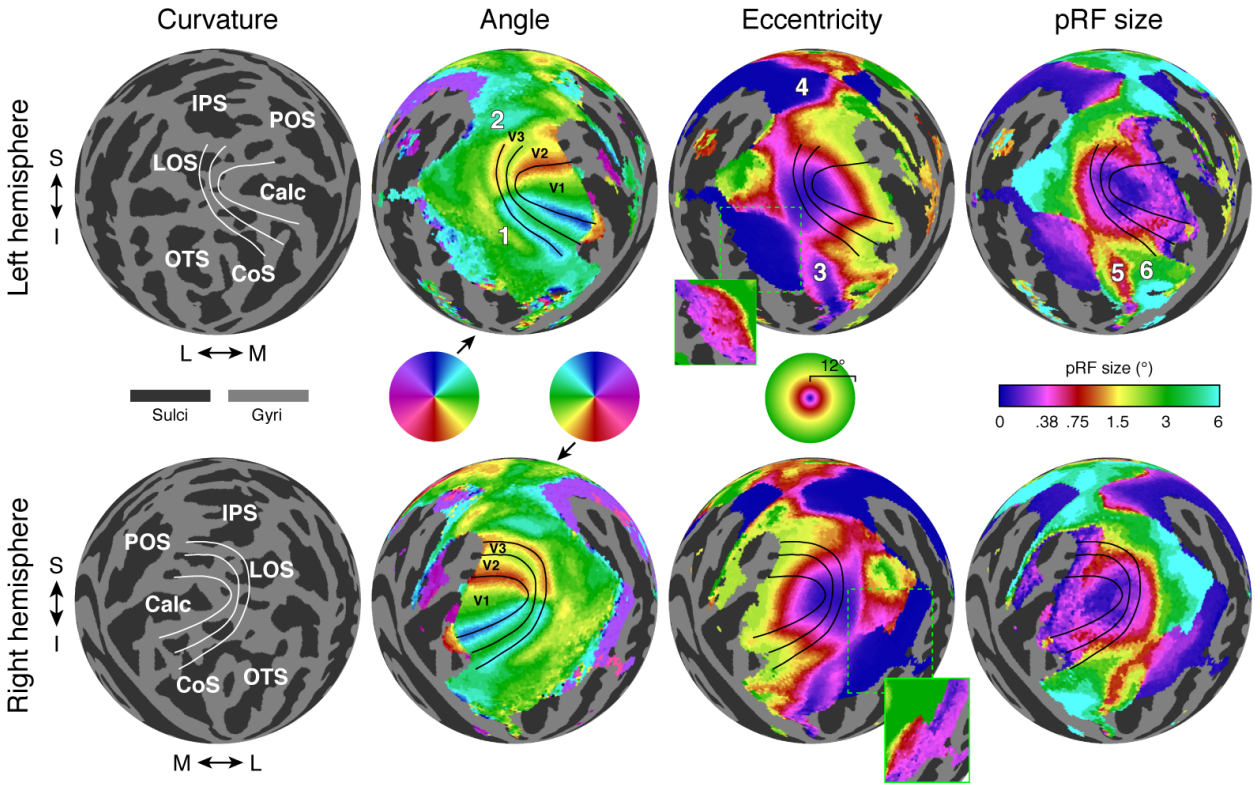

Figure 1.5: Retinotopic maps acquired from pRF model estimation. Data is from group averaged results. Black or white lines indicate visual area boundaries. Adapted from Benson et al. (2018).

Audition occurs when sound in the physical world is detected by hair cells in the human cochlea. Sounds are oscillations in the medium (i.e., air) that it travels through. The oscillations travel through the human ear to arrive at the cochlea. The cochlea is a spiral-shaped structure that is narrowest at its base and widest at its apex. Lined within the cochlea is the basilar membrane, which deceases in stiffness from base to apex. These two properties allow the inner ear to decompose incoming sound into its frequency components where higher frequencies are encoded at the base and lower frequencies are encoded at the apex. Inner ear hair cells are present throughout the basilar membrane and activated by the mechanical deflections caused by incoming frequencies. It is because of the position-based frequency filtering in the cochlea that the location of hair cell activity also transmits the frequency information of the auditory stimulus. This frequency-place organization that propagates

throughout the auditory system is known as cochleotopy, but is more often referred to as tonotopy in neuroimaging (Saenz & Langers, 2014).

Investigations into tonotopic organization in the auditory system parallels the investigations into retinotopic organization in the visual system. Electrophysiology recordings in animals were the first to report on tonotopic organization in the cochlea (for review, Clopton et al., 1974), subcortical structures like the inferior colliculus (Aitkin et al., 1970; Aitkin et al., 1972; Aitkin & Webster, 1971; Rose et al., 1963), and primary auditory cortex (A1; Goldstein et al., 1970) by recording neural activity to sounds of different frequencies. These studies established the existence of tonotopic structure maintained throughout the auditory system. When human neuroimaging methods became available, auditory related cortical activation could be seen in magnetoencephalography (MEG; Langner et al., 1997; Romani et al., 1982), PET (Lauter et al., 1985), and fMRI (Bilecen et al., 1998; Wessinger et al., 1997). Early neuroimaging work localized human primary auditory cortex centered on Heschl's gyrus (HG) located within the lateral sulcus.

When the phase-encoded method showed promising retinotopic map results, the auditory literature adapted the technique to perform tonotopic mapping in human auditory cortex. Talavage et al. (2004) presented auditory stimuli that repeatedly swept from high-to-low or low-to-high frequency as subjects were in an MRI scanner. They found tonotopic maps that were centered on HG that validated the phase-encoded methods for the auditory system. Subsequent, studies used the phase—encoded method to report extended tonotopic maps in secondary auditory cortices (Striem-Amit et al., 2011) and frequency representation reversal patterns that supported A1 area boundaries (Figure 1.6A; Da Costa et al., 2011) in human auditory cortex.

Eventually, this would also lead to adapting the pRF model to estimate tonotopic organization in human auditory cortex. The major advantage of the pRF method is that it is an explicit computational framework of stimulus input to fMRI response output (Wandell & Winawer, 2015). This means that the components of the pRF method (Equation 1.2, stimulus, pRF model function, HRF) can change form without having to change the esti-

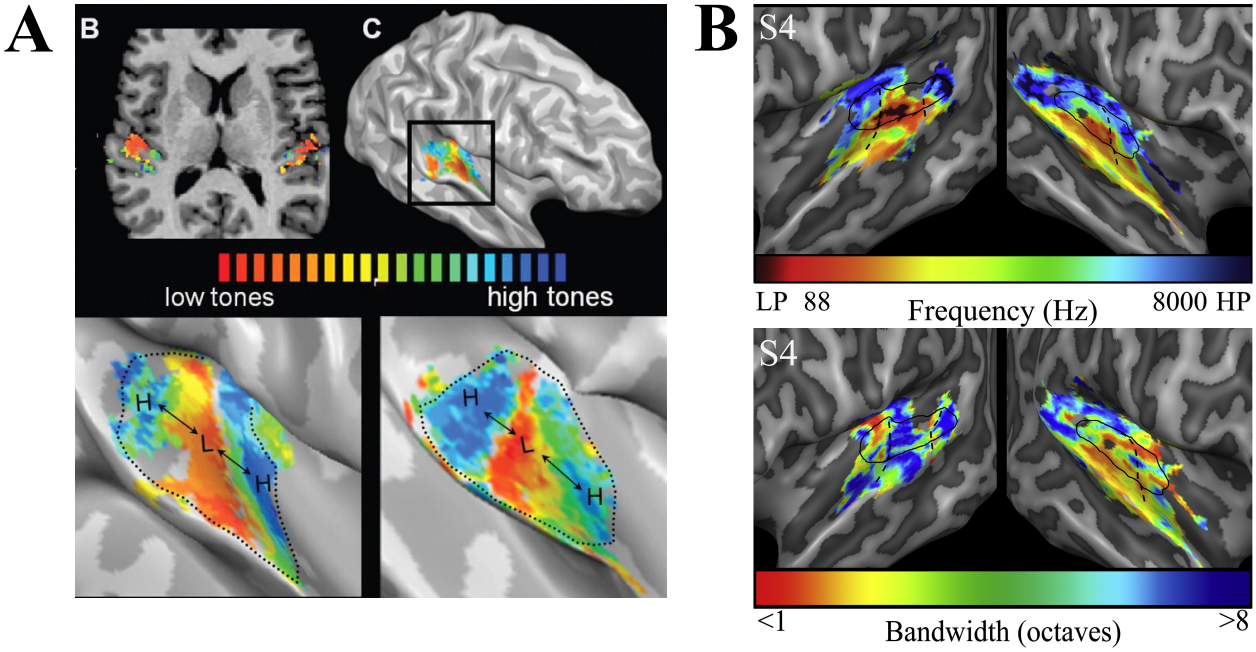

Figure 1.6: Tonotopic maps from phase-encoded and pRF methods. (A) Phase-encoded tonotopic maps for two example subjects, adapted from Da Costa et al. (2011). (B) pRF estimated (*upper*) frequency and (*lower*) bandwidth tonotopy maps from an example subject, adapted from Thomas et al. (2015).

mation procedure. To estimate auditory pRFs, Thomas et al. (2015) redefined the stimulus and pRF model function to be parameterized in log frequency space. The stimulus was a function of frequency over where 0s and 1s indicate the presence or absence of a tone burst at the indicated frequency. The pRF model was redefined as a 1-dimension Gaussian in $\log_{10}$ frequency and could be formally expressed as

$$g\left(f\right) = \exp\left(-\left(\frac{\left(f - f_0\right)^2}{2\sigma^2}\right)\right) \tag{1.3}$$

Where f_0 is the center of the Gaussian and σ is the standard deviation. The last step was to adjust Equation 1.2 to incorporate the redefined stimulus time course and pRF model function, so that the predicted fMRI response was

$$r(t) = s(f,t)\, g(f) \circledast h(t) \tag{1.4}$$

When estimated, f_0 is interpreted to represent the preferred frequency and σ is interpreted as the bandwidth of the frequency tuning. Thomas et al. (2015) demonstrated that the pRF framework was flexible and capable of estimating frequency-selective pRFs characterized the tonotopy organization in human auditory cortex. Figure 1.6B shows tonotopic maps estimated with the pRF method.

1.6 pRF Model Applications

The pRF model has been an invaluable tool in human vision research. One application has been to acquire pRF parameter estimates and compare them with known properties of visual cortex from physiological data. Dumoulin and Wandell (2008) compared pRF of size by eccentricity estimates with RF sizes and eccentricity from single- and/or multi-unit measurements. They confirmed that human pRF sizes increased as a function of eccentricity and along the visual hierarchy. Amano et al. (2009) expanded on this by retinotopically mapping hMT+, or human visual motion selective cortex. hMT+ was assumed to have retinotopic maps because of projections from early visual cortex and they verified that hMT+ had retinotopic maps of both hemifields and larger pRF sizes than early visual cortex across all eccentricities. The pRF method has even had success in estimating retinotopic maps in subcortical structures (DeSimone et al., 2015) and the cerebellum (van Es et al., 2019).

Another organizational property the pRF model examined was cortical magnification factor (CMF). Cortical magnification is an organizational principle where more cortical areas with small RFs is devoted to representing central vision and less cortical areas with larger RFs represent peripheral vision (Dow et al., 1981; Hubel & Wiesel, 1962, 1974; Van Essen et al., 1984). Then, CMF is the cortical surface distance between two points representing 1° distance in the visual field (Daniel & Whitteridge, 1961). Based on that definition, pRF estimates of preferred location and cortical distance measurements were used to calculate CMF in humans (Harvey & Dumoulin, 2011). The CMF metric has been used to characterize visual field

representation asymmetries (Silva et al., 2018), explain variability in visual task performance (Benson et al., 2021), and establish functional differences in amblyopia (Clavagnier et al., 2015).

Currently, the literature using the pRF model to investigate topographical organization human auditory cortex is in its nascent stage. Partially this is due to the lack of consensus regarding the where and which dimensions of representation are present in human auditory cortex besides frequency (Saenz & Langers, 2014). However, the pRF method is the right analysis to use to answer this question because it requires explicit parameterization of stimulus space. Recent work by Allen et al. (2022) marks the first study to use the pRF model to demonstrate maps representing tuning for frequency, timbre, and pitch.

The pRF model outputs parameterized results that allows for pRF estimates to be compared across conditions and populations of people. For example, the pRF method has been applied to study the effect of attention in visual (Kay et al., 2015; B. P. Klein et al., 2014; Sprague & Serences, 2013) and auditory (Lage-Castellanos et al., 2022) cortex. Interestingly, results differs between visual and auditory pRFs. In vision, increased attention demand increased pRF amplitudes and shifted pRF centers towards the attended location with little change to pRF size (Kay et al., 2015; B. P. Klein et al., 2014; Sprague & Serences, 2013) and the attentional effect also increases along the visual hierarchy. In contrast, the effect of attention on auditory pRFs demonstrate narrower tuning and decreased amplitudes although the attention effect also increased along the auditory hierarchy (Lage-Castellanos et al., 2022).

The pRF method has also been used to investigate neural plasticity. In the case of vision, studies examined if pRF's would remap locations in macular degeneration (MD) patients and sighted individuals with artificial scotomas. MD patients are individuals whose portion of retina that represents foveal vision has died thereby creating a blind spot called a scotoma. Thus, the portion of visual cortex that was used for foveal vision processing is no longer receiving incoming signals. Previous MRI studies reported activation in cortical regions that represent foveal vision in some MD patients with complete foveal vision loss when shown stimuli at the edge of their scotoma (Baker et al., 2005, 2008; Dilks et al., 2009,

2014). Although these studies had variable results, generally, they supported reorganization of visual cortex that represented the fovea to have been remapped to representing a parafoveal location in MD patients. However, Baseler et al. (2011) used the pRF model to estimate retinotopic maps of MD patients and found no evidence for cortical remapping. In the case of audition, the pRF model was used to estimate frequency-selective pRFs in hMT+ of early blind and sight recovery individuals (Huber, Jiang, et al., 2019). Huber, Jiang, et al. found that long-term visual deprivation could induce cross-modal cortical reorganization such that hMT+, which typically responds to visual motion, produced frequency tuned pRFs when estimated with moving auditory stimuli.

The original pRF model is a powerful and adaptable framework that has seen continued development of its computation elements. As stated, the pRF method can be readily adapted by redefining the parameterized stimulus and model space to estimate maps in other sensory domains like audition (Thomas et al., 2015), but also in the somatosensory system (Puckett et al., 2020; Schellekens et al., 2018, 2021; Wang et al., 2021). Studies have also incorporated non-linear computations into the pRF model, such as surround suppression (Zuiderbaan et al., 2012), compressive spatial (Kay et al., 2013) or temporal (Zhou et al., 2018) summation, or divisive normalization (Aqil et al., 2021). The effort to include non-linear computations are used to examine if known non-linear neuronal mechanisms would be reflected in the fMRI signal especially in higher order sensory areas. Substantial work has also explored the effects of different model fitting procedures, such as using a Bayesian approach (Zeidman et al., 2018), incorporating gaze-correction (Hummer et al., 2016), or changing error metrics and cost functions (Lage-Castellanos et al., 2020). Such efforts support pRF reliability (Benson et al., 2018; Lerma-Usabiaga et al., 2020; Senden et al., 2014; van Dijk et al., 2016) so that applications and comparisons of pRF estimates remain valid.

1.7 Outline

As previously stated, the pRF method can be used in a variety of ways to examine many research topics of interest. In this dissertation, I present my work that used the pRF model

to demonstrate the generalizability, applicability, and reliability of the pRF method as a computational model of functional organization in human visual and auditory cortex.

In Chapter 2, I show that the pRF model can reliably encode frequency representation in primary auditory cortex and use the frequency information to accurately decode novel stimulus sequences (Chang et al., 2017). This work validates the generalizability and predictive performance of the pRF model.

In Chapter 3, I demonstrate an application of the pRF model to examine neural plasticity in auditory cortex. Specifically, I examined neural plasticity in tonotopic representation in auditory cortex due to long-term visual deprivation (Huber, Chang, et al., 2019). To accomplish this, I compared pRF estimate differences from normally sighted versus early blind individuals. This work provided evidence towards systematic functional changes in early auditory processing.

In Chapter 4, I will return to the visual cortex and provide an improved stimulus protocol designed to minimize biases in pRF estimates. This stimulus design was created from the knowledge of cortical properties in visual cortex. I use a combination of modeling and simulation work to demonstrate the improvement provided with the use of this novel stimulus. Thus, providing more reliable and accurate pRF estimates of human visual cortex.

Chapter 2

RECONSTRUCTING TONE SEQUENCES FROM FMRI BOLD RESPONSES WITHIN HUMAN PRIMARY AUDITORY CORTEX

2.1 Introduction

A variety of blood-oxygen level dependent (BOLD) imaging studies have identified a pair of mirror-symmetric tonotopic gradients centered on Heschl's gyrus on the cortical surface, thought to be the human homologs of primary areas A1 and R (Da Costa et al., 2011; Formisano et al., 2003; Humphries et al., 2010; Moerel et al., 2012; Saenz & Langers, 2014; Woods et al., 2009). These maps have been replicated across diverse imaging paradigms (Da Costa et al., 2015; Langers, Sanchez-Panchuelo, et al., 2014; Moerel et al., 2018; Thomas et al., 2015) and a range of stimulus types including orderly frequency progressions (Da Costa et al., 2011; Langers, Krumbholz, et al., 2014; Striem-Amit et al., 2011; Talavage et al., 2004), random tone sequences (Thomas et al., 2015), and complex natural stimuli (Moerel et al., 2012).

However, while the overall pattern of frequency gradients is highly replicable, the accuracy with which these maps have modeled the actual frequency preferences of individual voxels is unclear. For example, several groups (Formisano et al., 2003; Humphries et al., 2010; Langers, Krumbholz, et al., 2014; Woods et al., 2009) have obtained robust tonotopic maps by evaluating BOLD responses to only a few discrete frequencies using a general linear model (GLM). However, these models fail to capture the explicit representation of frequency selectivity in the auditory cortex, which is thought to represent a wide range of auditory frequencies. Stimulus-specific biases can also alter the frequency preference assigned to a given fMRI voxel. Frequency "sweep" stimuli have been shown to induce a "traveling wave"

of BOLD activity across the cortex (Engel et al., 1994) that is susceptible to biases induced by habituation and/or expectation effects as well as spatio-temporal BOLD non-linearities (Binda et al., 2013; Thomas et al., 2015). The complex morphology and small size of auditory cortical areas makes them highly susceptible to these biases (Saenz & Langers, 2014). Consequently, while the general topographic organization of PAC seems to be robust to the stimulus that was used, the frequency assigned to a given voxel can vary dramatically depending on the stimulus, for example the direction of the frequency sweep that is used (Da Costa et al., 2011; Thomas et al., 2015).

More recently, somewhat more complex modeling approaches have been applied to characterizing the response selectivities of auditory areas. One influential class of models has utilized an approach whereby natural scene stimuli are parameterized into a feature space and regularized linear regression is used to characterize each voxel's response preference across this feature space (Kay et al., 2008; Naselaris et al., 2011; Nishimoto et al., 2011). The advantage of this approach is that it attempts to capture the complexity of cortical processing without explicitly imposing a preselected model (e.g., Gaussian tuning) upon the response selectivity profile for a given voxel (although the parameterization of the stimulus space must be appropriate). Voxel selectivity can be estimated as a weighted sum of the features to which the voxel responds. Recent papers using this approach have shown selectivity for, and interactions between, frequency, time, and spectro-temporal modulation (Moerel et al., 2018; Santoro et al., 2014).

The second class of models – the population receptive field (pRF) approach – has been equally influential. For this class, the response of the voxel is assumed to have a specific parameterized form (e.g., Gaussian tuning with log frequency) rather than allowing the stimulus to determine the selectivity profile. This provides an explicit function of voxel selectivity along the dimension(s) of interest (Dumoulin & Wandell, 2008; Zuiderbaan et al., 2012). Models of this class have tended to rely on relatively minimalist parameterizations (e.g., two parameters for a Gaussian in frequency space). Indeed, the popularity of this approach has rested in large part on its simplicity. One advantage is that it provides a clear

test of how well a specific parameterized model of individual voxel tuning properties can predict BOLD responses within a given area. As a result, estimated parameter values can easily be compared across a wide range of stimulus paradigms, cortical areas, and subject groups.

Previously, we applied the pRF approach to auditory cortex to measure the frequency selectivity for individual voxels (Thomas et al., 2015). Here, we present a method for examining whether our simple model of frequency tuning can predict responses to more natural, familiar, and predictable stimuli. Specifically, we examined whether tonotopic maps generated using randomized tones could be used to decode and reconstruct a sequence of tones on the basis of an individual subjects' BOLD responses over time. First, we characterized the tonotopic organization of each subject's auditory cortex by measuring auditory responses to randomized pure tone stimuli and modeling the frequency tuning of each fMRI voxel as a Gaussian in log frequency space. Next, we measured cortical responses in the same subjects to novel stimuli containing a sequence of tones based on the melodies "When You Wish Upon a Star" (Harline et al., 1940) and "Over the Rainbow" (Arlen & Harburg, 1939). These 'song-like' sequences were chosen because they include complex temporal dependencies as well as expectation effects, albeit over a very slow time scale. Then, using a parametric decoding method, we reconstructed the tones from these songs by determining what frequency would best maximize the correlation between predicted (based on our pRF models) and obtained BOLD activity patterns for each point in the stimulus time course.

2.2 Materials and Methods

Three right-handed subjects (2 male, 1 female, ages 27–46) participated in two fMRI sessions. Subjects reported normal hearing and no history of neurological or psychiatric illness. Written informed consent was obtained from all subjects and procedures, including recruitment and testing, followed the guidelines of the University of Washington Human Subjects Division and were reviewed and approved by the Institutional Review Board.

2.2.1 MRI Data Acquisition and Analysis

Blood-oxygen level dependent imaging was performed using a 3 Tesla Philips Achieva scanner (Philips, Eindhoven, The Netherlands; Goebel et al., 2006) at the University of Washington Diagnostic Imaging Sciences Center (DISC). Subjects were instructed to keep their eyes closed throughout all scans and foam padding was used to minimize head motion. fMRI data were acquired using a 32-channel head coil and a continuous EPI pulse sequence ($2.8 \times 2.8 \times 2.8$ mm^3, TR/TE = 2000/25 ms, flip angle = 60°, EPI-factor = 35, no slice gap). We used a continuous sequence designed with Philips SofTone software (SofTone factor of 4.0) to generate less acoustic scanner noise (Thomas et al., 2015).

Standard pre-processing of fMRI data was carried out using BrainVoyager QX software (version 2.3.1, Brain Innovation B.V., Maastricht, The Netherlands), including 3D motion correction, slice scan time correction, and temporal high-pass filtering. 3D motion correction was performed by aligning to all volumes to the first volume within a session on 9 parameters for translation, rotation, and scale. Slice scan time correction was performed using cubic spline interpolation with an ascending and interleaved order of the slice scan acquisition. Temporal high-pass filtering was performed at a cutoff of 2 cycles per scan. Functional data were aligned to a T1-weighted anatomical image acquired in the same session (MPRAGE, $1 \times 1 \times 1$ mm^3). The anatomical images acquired in the two sessions were aligned to each other and to each subject's 3D Talairach-normalized functional dataset. The BrainVoyager QX automatic segmentation routine was used to reconstruct the cortical surface and the resulting smooth 3D surface was partially inflated. For each subject, large anatomical regions of interest (ROIs) were selected from both hemispheres of the auditory cortical surface using drawing tools within BrainVoyager QX. Preprocessed time-course data for each 3D anatomical voxel within the volume ROI were then exported to MATLAB for further analysis.

2.2.2 Auditory Stimulus Presentation

Sound stimuli were generated in MATLAB using the Psychophysics Toolbox (www.psychtoolbox.org). Stimuli were delivered via MRI compatible insert earphones (S14; Sensimetrics), at a sampling rate of 44.1 kHz, with intensities calibrated to ensure flat frequency transmission from 100 to 8 kHz. After sound system calibration, stimulus sound intensities were adjusted according to a standard equal-loudness curve created for insert earphones (ISO 226: 2003) to approximate equal perceived loudness across all frequencies. Acoustic noise from the scanner was attenuated by expanding-foam ear tips as well as protective ear muffs placed over the ear following earphone insertion. Subjects reported hearing all stimuli at a clear and comfortable audible level, with roughly equal loudness across all tones.

2.2.3 pRF Estimation

To reduce the influence of spatiotemporal non-linearities on pRF estimates, we measured fMRI responses to randomized pure tone sequences consisting of 240 frequency blocks. As shown in Figure 2.1A, each block lasted 2 s and consisted 8 pure tone bursts of a single frequency. Each burst lasted either 50 or 200 ms in duration (inter-stimulus interval = 50 ms) and was presented in a pseudo-randomized order, resulting in a "Morse code" like pattern of tones. This served to increase the perceptual salience of the tone bursts over the background scanner noise. The frequencies presented in the blocks were equally spaced on a logarithmic scale, ranging from 88 to 8000 Hz. Each frequency block was presented only once per scan and block order was randomly shuffled for each scan. Following every 60 blocks was a 12 s silent pause. This silent period allows the pRF algorithm to better estimate the baseline fMRI response to scanner noise. Each subject participated in a single pRF estimation scanning session, consisting of 6 scans, each containing a different randomized sequence of the same 240 frequency blocks.

Following previously described methods, we used customized MATLAB software to estimate the frequency tuning curves for individual voxels based on a linear temporal model

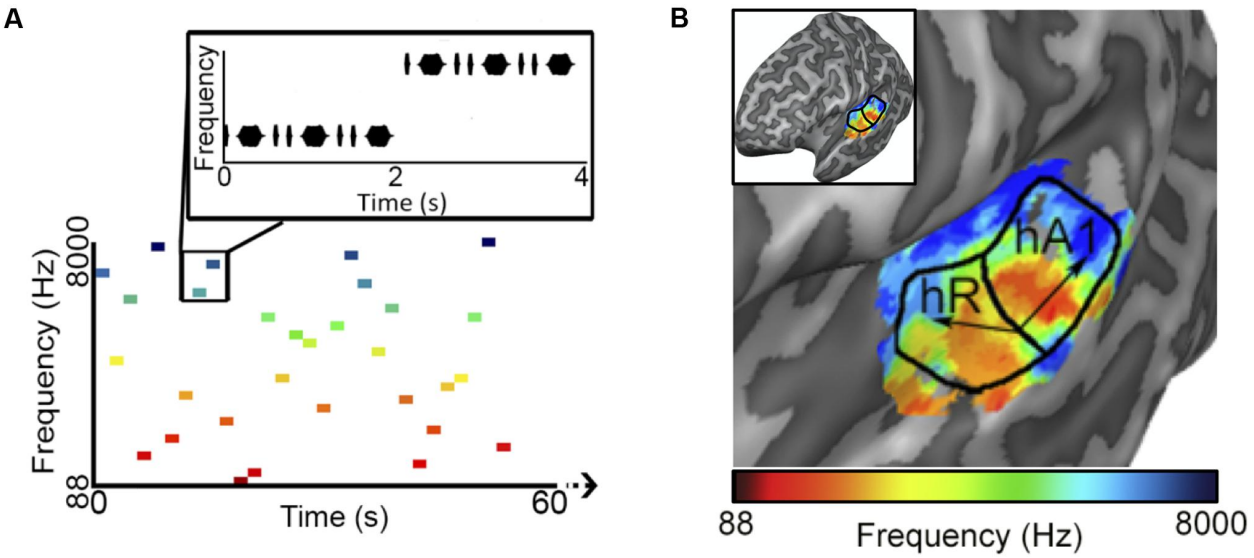

Figure 2.1: Tonotopic population receptive field (pRF) estimation. (A) The first 60 s of an example random sequence stimulus used during pRF estimation. Each block lasted 2 s and consisted of 8 pure tone bursts of a single frequency. Bursts lasted either 50 or 200 ms in duration (inter-stimulus interval = 50 ms) and were presented in a pseudo-randomized order. (B) Tonotopic and bandwidth maps for the left hemisphere of example Subject 1. As indicated by the black arrows, pRF frequency center (Hz) values formed two mirror-symmetric tonotopic gradients corresponding to the primary auditory fields A1 and R, outlined here by solid black lines. No clear organization was observed for pRF bandwidth (octaves) values (not shown).

of the fMRI BOLD response time course (Thomas et al., 2015). Briefly, analysis began by defining a stimulus time course, which indicates the presence or absence of a particular frequency over time. This stimulus time course was convolved with each subject's estimated hemodynamic response function (HRF) modeled as a gamma probability density function (Boynton et al., 1996). Each voxel's response was modeled using a 1-dimensional Gaussian function $g(f)$, defined over frequency (in log space). The center (f_0) of each Gaussian corresponds to the frequency of the voxel's maximum sensitivity, and the standard deviation (σ) corresponds to the range of frequencies that the voxel is sensitive to. Standard deviations are reported as bandwidth values by calculating the full width half maximum (FWHM) in terms

of octaves. A predicted fMRI time course was then generated for each voxel by calculating the linear sum of the overlap between the hemodynamically blurred stimulus time course and the pRF model. Finally, model fits for each voxel were obtained using a non-linear search algorithm that found the model parameters that maximized the correlation value (goodness-of-fit) between the voxel's pRF predicted time course and the acquired fMRI BOLD response time course (using Matlab's "fmincon" function).

The procedure described above included a few modifications from our original pRF analysis (Thomas et al., 2015). First, we included a static power-law non-linearity within the Gaussian model by including a free exponent parameter (n) to account for non-linear summation of the BOLD response according to the compressive spatial summation (CSS) model (Kay et al., 2013). The incorporation of this static non-linearity, which is applied after the initial fitting of the linear model, has been shown to more accurately explain BOLD activity and improve overall receptive field fits. This parameter was constrained to fall between 0 and 1. Second, we constrained the Gaussian standard deviation (σ) to values greater than 0.015 (chosen based on the resolution of the presented frequencies).

The drawing of the PAC region of interest was performed using both the functional data and following anatomical landmarks. A second independent observer verified the selection of the ROI.

After fitting, only voxels within PAC, with a pRF correlation value (goodness-of-fit) above 0.15 were retained for song decoding and reconstruction (533, 530, 244 voxels for subjects S1–S3, respectively). Results were robust to a wide range of correlation values. Critically, all voxels with pRF fits above this threshold within PAC were included in all further analyses, there was no further selection based on the ability to predict the song-like stimuli. Thus, there was no selection of voxels on the basis of their ability to generalize to a novel stimulus. As demonstrated in Figure 2.1B, pRF center (f_0) values formed two mirror-symmetric tonotopic gradients corresponding to the primary auditory fields A1 and R in both hemispheres of all subjects. No clear topographical organization within PAC was observed for either pRF bandwidth values (average bandwidth in octaves $\pm SD$, $S1 = 3.385 \pm 2.807$,

$S2 = 3.732 \pm 1.634$, $S3 = 2.219 \pm 1.201$), or exponent parameters (average value of $n \pm SD$; $S1 = 0.587 \pm 0.310$, $S2 = 0.611 \pm 0.228$, and $S3 = 0.726 \pm 0.318$).

2.2.4 Frequency Decoding

During a separate scanning session, we collected fMRI responses to two pure tone song-like sequences based on two familiar melodies: "When You Wish Upon a Star" (Wish) and "Somewhere Over the Rainbow" (Rainbow). Each song-like sequence was generated using 2 s frequency blocks with frequencies ranging from 880 to 2349 Hz (corresponding to the notes A5-D7 on the western music scale). Each 2 s block contained 13 tone bursts of the same frequency, each lasting 75 ms in duration (inter-stimulus interval = 75 ms). This created a vibrato-like effect which served to increase the perceptual salience of each block, without interrupting the melodic feel of the song-like sequence. A single presentation of each song-like sequence contained either 25 (Wish) or 23 (Rainbow) frequency blocks followed by 8 s of silence, and the entire presentation was repeated 8 times per scan. Averaged fMRI BOLD time courses were then generated for each song-like sequence by averaging data responses across the eight presentations within each scan, and across two scans of the same sequence type.

We decoded both song-like sequences by reconstructing each sequence one block at a time. To do this, we used the pRF models previously generated with the randomized tone sequences to generate predicted voxel activity patterns elicited for a set of 14 frequencies sampled from 88 to 8000 Hz in half-octave steps. The best fitting frequency from this set is then used as the initial parameter for a non-linear optimization fitting procedure (again, Matlab's "fmincon" function) that determined what frequency produced the predicted voxel activity pattern best correlated with the measured voxel activity pattern for each 2 s block. This process was then repeated for each block in the sequence, until all frequency blocks had been reconstructed. Finally, to account for the delayed hemodynamic blurring of BOLD signal a fixed temporal lag of 6 s was applied to the reconstructed sequence (Kay et al., 2008).

It is important to note that our method only depends on the frequency selectivity of individual voxels, not their physical locations within auditory cortex. This method is therefore not dependent upon any particular model (Moerel et al., 2015; Saenz & Langers, 2014) of frequency selectivity organization.

The quality of the reconstructed sequences was quantified in three ways: *Identification performance*, *reconstruction accuracy*, and *model reliability*.

Identification performance was assessed as the ability to correctly identify the actual song over other song-like sequences that contained similar statistical properties. For each reconstructed sequence, we applied an algorithm based on first-order Markov chains to randomly generate 1000 simulated (new sequences were generated for each subject) song-like sequences that reflected the frequency content and note-to-note probabilities of the Rainbow and Wish sequences. Other more advanced methods for generating simulated sequences exist, including probabilistic models of melodic intervals (Temperley, 2008, 2014). However, our model was generated using unpredictable stimuli, and did not incorporate any information about interval dependencies. Consequently, identification performance was unlikely to be significantly altered by the use of more realistic foil sequences. We then calculated the correlation (Pearson's r) between the reconstructed sequence and the actual sequence of tones, as well as for each of the simulated foils. Identification performance was defined as the number of times in which the actual sequence was correctly selected, on the basis of having a higher correlation with the reconstructed sequence than any of the 1000 simulated sequences.

Reconstruction accuracy was assessed as the ability to recreate each note in the actual sequence. This was calculated as the residual difference in cents (1200 cents per octave) between each note in the reconstructed and actual sequences. To determine if any systematic over or underestimation was present in the reconstructed sequences, we performed a two-tailed t-test on the means of the residual errors. Any mean that was significantly different from zero reflected an overall bias in reconstruction accuracy.

Model reliability was assessed using the metric of relative root mean square error ($rRMSE$, Rokem et al., 2015). For both song-sequences we normalized the root mean square error

(RMSE) value describing the difference between predicted and measured time series by the RMSE describing the difference between the time series of each of the two scans collected for that song-sequence. Thus, for each song:

$$rRMSE = \frac{(RMSE\,(TC_{pred}, TC_{scan1}) + RMSE\,(TC_{pred}, TC_{scan2}))}{2RMSE\,(TC_{scan1}, TC_{scan2})} \tag{2.1}$$

where TC_{scan1} and TC_{scan2} are the measured time course for the song-like sequence obtained in individual scans and TC_{pred} is the predicted time course for the song-like sequence, based on our pRF model (generated using random tones). This measure provides us with an index of the goodness-of-fit of our model, relative to measurement reliability. As described by Rokem et al. (2015), if the model has higher accuracy than test–retest accuracy then $rMSE < 1$. For simple cases of IID signals with zero-mean Gaussian noise, if the model perfectly captured the data then $rRMSE = \frac{1}{\sqrt{2}} = 0.707$.

2.3 Results

We began by determining the correlation between reconstructed and actual frequencies for each subject for both Rainbow and Wish (Figure 2.2A,B and Table 2.1) sequences. For all subjects, reconstructed sequences were well correlated with the actual sequences that were presented, indicating good reconstruction accuracy.

Figure 2.2C,D illustrate identification performance. Histograms containing the correlation between the reconstructed Rainbow (Figure 2.2C) and Wish (Figure 2.2D) sequences and 1000 simulated foils. The correlation value between the predicted and the actual sequence is represented by a black line in each histogram, indicating the correlation value for the actual sequence. Identification performance for both Rainbow and Wish was at near perfect levels for all three subjects, demonstrating that the identity of a tone sequence can be readily be decoded based on the similarity between the predicted BOLD response to that sequence of tones and the measured BOLD response.

Figure 2.3 displays the notes of the actual and reconstructed sequences of each subject on the five-line staff according to modern musical notation. Purely for illustration purposes, the

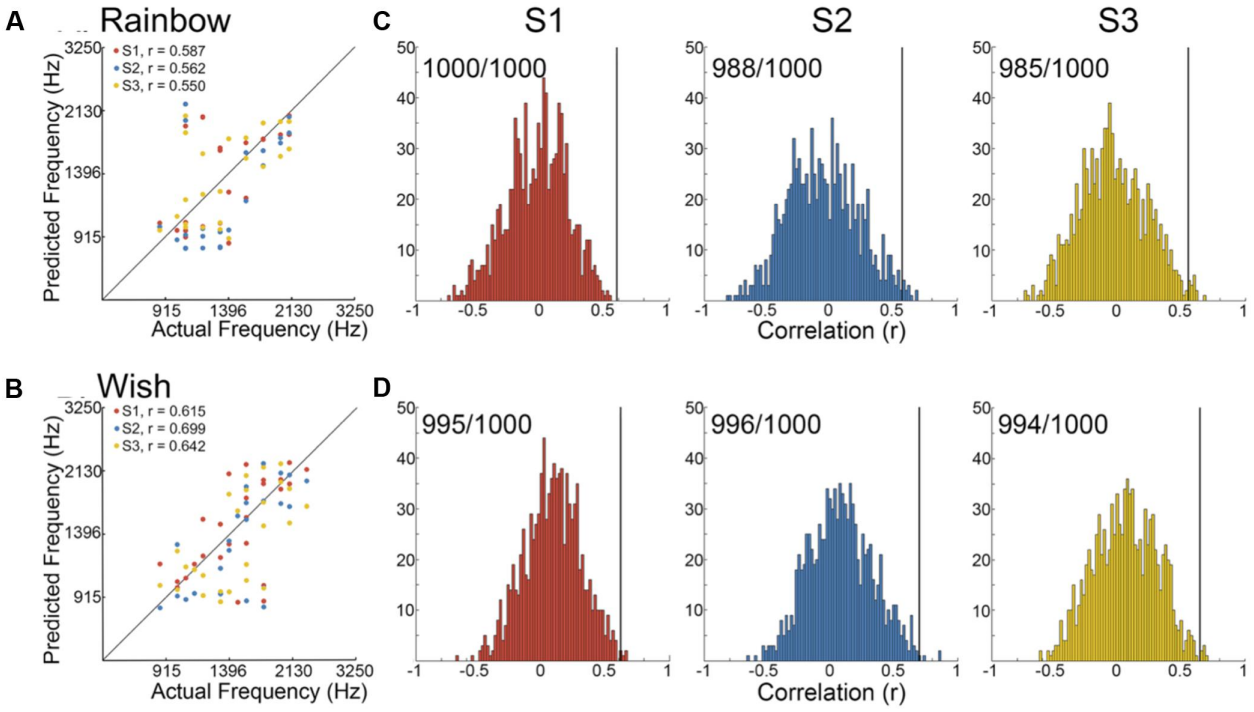

Figure 2.2: Tone identification performance. (A,B) Scatter plots showing the correlation between reconstructed and actual frequencies for each subject for both the Rainbow (A) and Wish (B) sequences, also shown Table 2.1 (C,D) Using a method based on a first order Markov chain algorithm, we simulated 1000 song-like sequences reflecting the frequency content and note-to-note probabilities of the Rainbow (C) and Wish (D) sequences. Histograms show the distribution of correlation values (Pearson's r) between each of the simulated sequences and either reconstructed sequence. The line in black designates the correlation value between the actual song-like sequences and the reconstructed sequences, indicating the degree to which the correct sequence had been successfully identified. The number of correct identifications (out of 1000) is reported for each reconstructed sequence. Colors correspond to individual subjects.

reconstructed frequencies in Figure 2.3 were rounded to the nearest semitone (12 semitones per octave), or "note." We also lowered all notes (actual and reconstructed) one octave for better representation on the treble clef. One way of assessing the precision of our pRF decoding method is by examining how accurately each song-like sequence was reconstructed in terms of musical intervals or cents. The standard deviations of the residual errors are reported in Table 2.1. Standard deviations ranged between 434 and 512 cents across subjects and songs (around three to four notes, or a third of an octave).

Subject	**Stimulus**	**Pearson's r**	**Residual Error (cents)**
S1	Rainbow	0.587	25.98 ± 465.44
	Wish	0.615	-30.71 ± 448.05
S2	Rainbow	0.562	-210.12 ± 512.17
	Wish	0.699	-215.54 ± 421.35
S3	Rainbow	0.550	14.60 ± 456.24
	Wish	0.642	-155.78 ± 434.02

Table 2.1: Model performance: Reconstruction accuracy. Correlation values (Pearson's r, also shown Figure 2.2) between reconstructed and actual frequency values, $M \pm 1\,SD$ of residual errors in cents between the reconstructed and actual frequencies.

We also examined whether the mean of the residual errors differed significantly from zero, which would reflect a systematic bias in reconstruction accuracy (Table 2.1). Of the six means, only one reached statistical significance with a two-tailed t-test (Subject 2, Wish, $t(24) = -215.54$ cents, $p = 0.0173$), non-significant after either Bonferroni or Bonferroni-Holm correction (Holm, 1979). Thus, there does not appear to be a systematic over or underestimation of reconstructed frequencies, at least as far as the power of our experimental design can provide.

Figure 2.4 shows that our model fits the novel song-sequences extremely accurately. The blue line shows $rRMSE = 1$, representing performance equal to test–retest reliability. For

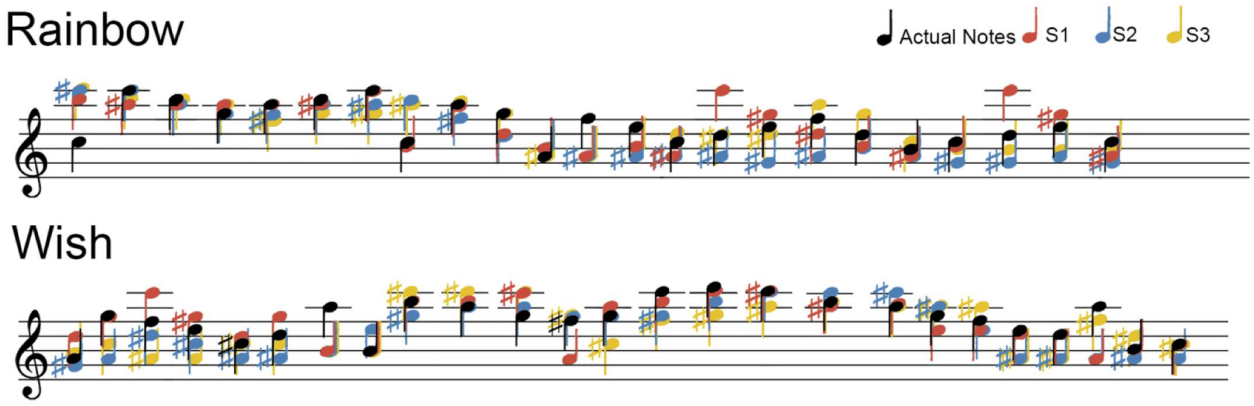

Figure 2.3: Tone sequence reconstruction. For easier visualization on a treble clef, all frequencies (Hz) were rounded the nearest semitone and lowered one octave. Actual notes from each song-like sequence are in black, while the color of notes in the reconstructed sequences corresponds to individual subjects.

all subjects and song-sequences most of the voxels had $rRMSE$ values < 1. Indeed, for 2 of the 3 subjects fewer than 1% voxels had $rRMSE$ values greater than 1. The red line shows $rRMSE = 0.707$: the expected performance value if the model was perfect (assuming zero-mean IID noise). The median $rRMSE$ values for all three subjects were close to the expected value of a perfect model, with only small room for improvement.

2.4 Discussion

Using a combined auditory pRF encoding/decoding approach, we found that we could accurately identify and reconstruct tone sequences over time on the basis of BOLD responses, thereby demonstrating the predictive accuracy of our model of frequency selectivity of PAC.

2.4.1 Encoding/Decoding Models of Sensory Cortex

A few previous studies have used linear classifier algorithms, trained to discriminate between stimulus categories based on patterns of activity across fMRI voxels, to classify speech content and speaker identity (Formisano et al., 2008) as well as the emotional content of speech (Ethofer et al., 2009). One limitation of such classification approaches is that they are

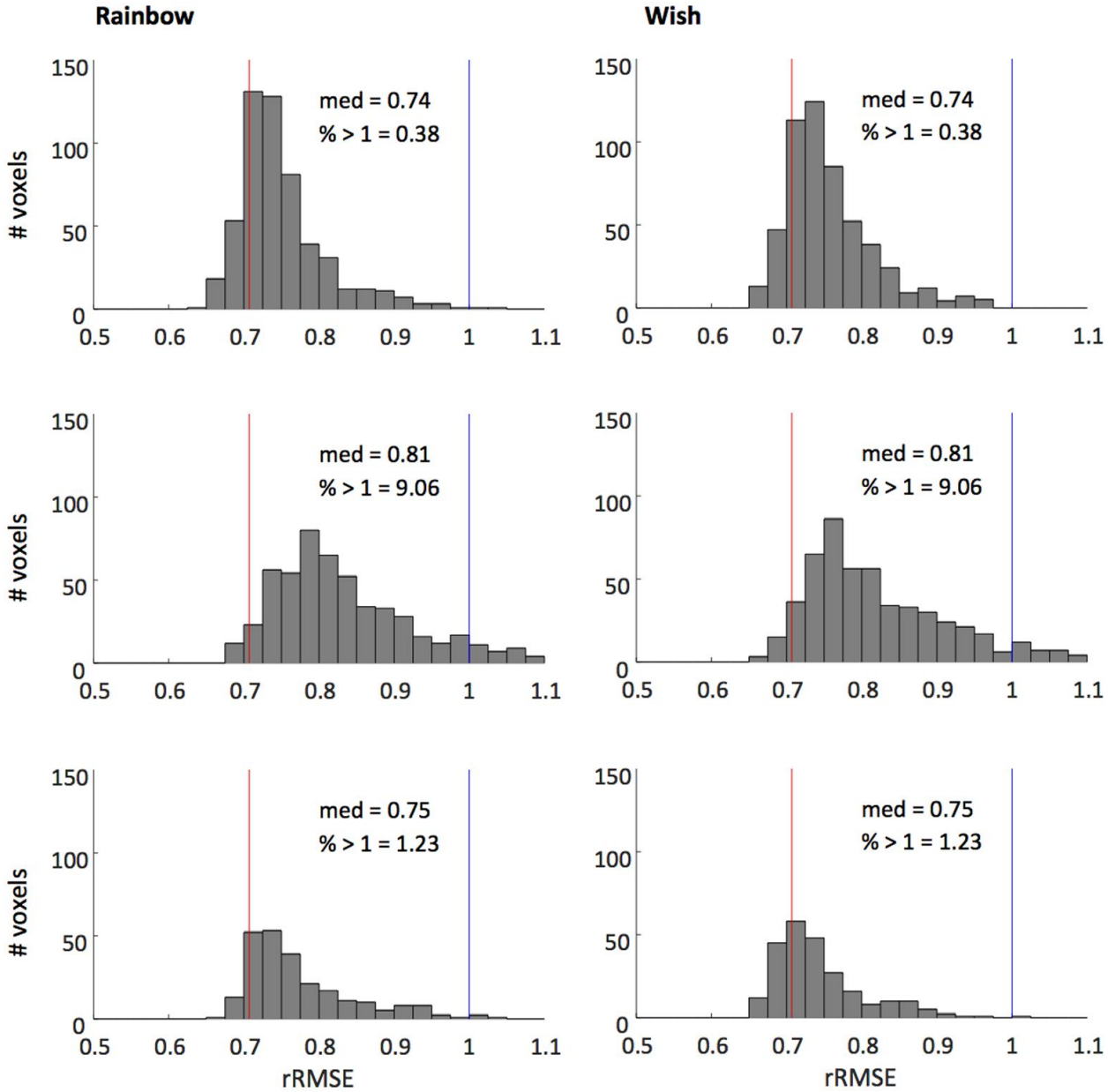

Figure 2.4: Histograms of voxel $rRMSE$ values for 2 song-like sequences and 3 subjects. The population receptive field model predicts the data better than test–retest reliability (blue line, $rRMSE = 1$) in almost all voxels. Median $rRMSE$ values are close to the expected performance of a perfect model (red line, $rRMSE = 0.707$). Inset text show median $rRMSE$ and the percentage of voxels > 1.

limited to candidate stimulus sets and cannot be generalized to substantially novel stimuli (Naselaris et al., 2011). Moreover, linear classifiers do not provide insight into the feature space of functional organization within auditory cortex (see, Naselaris & Kay, 2015, for discussion).

Another fundamental difference between our study and the linear classification studies described above, is that linear classifiers select the components in the response state with the greatest predictive value. Critically, for both identification and reconstruction we used all voxels within PAC whose responses could be fit by the pRF model. Thus, identification performance did not assess whether any voxels in PAC could successfully identify the tone sequence that was presented, but rather assessed whether the collective responses of voxels within PAC as a whole carries reliable and generalizable information about the tone sequence.

As described in the Section "Introduction," there currently exist two classes of models that are designed to carry out encoding/decoding that is generalizable to novel stimuli. The first relies on a parameterization of the stimulus space through single-voxel encoding (Kay et al., 2008; Moerel et al., 2014; Naselaris et al., 2009; Nishimoto et al., 2011; Santoro et al., 2014) and multivariable model-based approaches (Miyawaki et al., 2008; Santoro et al., 2017). Two previous studies (Moerel et al., 2018; Santoro et al., 2017) have used this approach to examine decoding and reconstruction performance for 1 s natural auditory scenes. In both studies responses to a training set were used to estimate each voxel's sensitivity to a range of spectrotemporal features. Sensitivity was described on the basis of models of varying degrees of complexity, ranging from simple frequency to a 4D model that included frequency, spectral modulation, temporal modulation and time. In the Moerel et al. (2018) study the model was assessed by computing the correlation between the models predicted time course to a given sound and the measured time courses to the remainder of the test sounds. In the Santoro et al. (2017) study, voxel responses to a test set, in conjunction with the voxel weightings across the feature space, were used to reconstruct the features of each test stimulus.

Our model belongs to the second class of models – our goal was to specifically model the response selectivity of the voxel with an assumed Gaussian selectivity profile. Our stimuli

and model only varied along the dimension of frequency, because we wanted to examine the pRF approach using a dimension whose representation within PAC is reasonably well characterized. Having shown that our model can identify what song-like sequence a person had been listening to with high reliability, we also demonstrate that a pRF model of tonotopic organization in the human primary auditory cortex can also reconstruct the sequence of tones played over time. Our encoding pRF model was used to describe the frequency selectivity of individual voxels in each subject's primary auditory cortex (Thomas et al., 2015). Then we applied a parametric decoding method on our pRF model to identify and reconstruct tone sequences. We examined the reliability and validity of our tonotopic encoding model in a variety of quantitative ways. Identification performance was virtually perfect. Reconstruction accuracy of single tones was also excellent, we were able to reconstruct the tones of the song-like stimuli for all three subjects within a half of an octave or less, with little evidence of systematic biases in frequency estimation. Finally, and importantly, our $rRMSE$ estimate of model accuracy suggests that our model, despite being much simpler than these other models, is nearly perfect: the model (generated using random tones) predicted the time course of song-sequences far better than test–retest reliability. Indeed, $rRMSE$ estimates of model performance suggested that our model performed close to optimally, despite these novel stimuli containing a more restricted range of frequencies, greater temporal dependencies, and (presumably) expectation effects. This suggests that, for the stimuli used here, these factors did not radically alter the tonotopic information carried by individual voxels.

As described above, other studies have shown that neurons in auditory cortex respond selectively to other stimulus dimensions, including spectral and temporal modulation, time and loudness (Barton et al., 2012; Baumann et al., 2011; Langner et al., 1997, 2009; Moerel et al., 2012, 2013, 2015, 2018; Sadagopan & Wang, 2009; Santoro et al., 2014, 2017; Schönwiesner & Zatorre, 2009; Uppenkamp & Röhl, 2014). However, while recent studies (Moerel et al., 2018; Santoro et al., 2017) make it clear that voxels vary in their responsivity across these various dimensions, there is still much to be learned about how topographical selectivity for these other dimensions vary within primary and secondary auditory areas, and

whether there are systematic differences in selectivity across these various dimensions across different cortical areas. Discovering parameterizations that can simplify this multidimensional space by summarizing voxel selectivity across multiple dimensions would be a natural extension of our approach. At some point it is likely that our approach (building up from simple stimuli and simple models) and that of other groups using more complex stimuli and models (Moerel et al., 2018; Santoro et al., 2017) will converge at an optimal level of model complexity.

One promising future direction will be inclusion of the effects of temporal regularities. The stimuli used to develop our pRF model did not contain any first or second order statistical regularities, and thus our model does not capture the effects of attention, expectation, or longer-term habituation (our model did include response compression) on the BOLD response, despite these factors being known to strongly modulate auditory cortex responses (Da Costa et al., 2013; Thomas et al., 2015). However, as described above, we were able to use pRFs based on responses to unpredictable stimuli to reconstruct the fMRI time courses to predictable song-like stimuli with nearly equal accuracy as for the unpredictable stimuli.

Other promising future directions include using a large number of subjects to examine variability in the population, using these methods to link cortical responses to perceptual experience for ambiguous auditory stimuli, examining whether cortical representations can predict behavioral performance in both typical and atypical populations, and examining the effects of frequency-selective attention (Da Costa et al., 2013; Woods et al., 2009).

Chapter 3

EARLY BLINDNESS SHAPES CORTICAL REPRESENTATIONS OF AUDITORY FREQUENCY WITHIN AUDITORY CORTEX

3.1 Introduction

It has long been held that early blindness leads to enhanced perception of auditory stimuli, and a number of behavioral studies have linked early-onset blindness to superior pitch perception (Gougoux et al., 2004; Voss & Zatorre, 2011; Wan et al., 2010). However, the neural basis of any such enhancements is not known. Heightened frequency discrimination as a result of blindness early in life could potentially be mediated by compensatory plasticity within deprived occipital cortex. Indeed, Kujala et al. (1992) observed that neural responses to pure tones, measured using EEG, were shifted posteriorly in a group of blind subjects, and subsequent MEG measurements further suggested these responses might be localized to occipital cortex (Kujala et al., 1995). Using fMRI, Watkins et al. (2013) observed responses to pure tones within area hMT+, an area typically associated with visual motion perception, in a subset of individuals with anophthalmia. More recently, (Huber, Jiang, et al., 2019) demonstrated that responses with hMT+ are selective for both auditory frequency and motion as a result of early blindness.

Enhanced auditory performance as a result of blindness might also be mediated by plasticity within auditory areas. Previous MEG results in congenitally blind individuals suggested an expanded tonotopic representation within a region identified as primary auditory cortex (Elbert et al., 2002), with responses to 500 and 4000 Hz tones being separated more widely on the cortical surface in blind relative to sighted individuals. An expanded tonotopic map might permit a finer frequency resolution. Indeed, expansion in the representation of specific auditory frequencies has been linked to superior discrimination performance after extensive

training (Recanzone et al., 1993). However, a few studies have reported an attenuated response to pure tone auditory stimuli in the temporal lobe of early blind individuals (Gougoux et al., 2009; Stevens & Weaver, 2009; Watkins et al., 2013). This has been interpreted as reflecting either increased "efficiency" of processing within the intact modality (Gougoux et al., 2009; Stevens & Weaver, 2009) or reduced participation in auditory processing, perhaps due to function being "usurped" by reorganized occipital cortex, as may occur for auditory motion processing (Dormal et al., 2015; Jiang et al., 2014).

Here, we used fMRI and population receptive field (pRF) modeling (Dumoulin & Wandell, 2008) in acoustic frequency space (Thomas et al., 2015) to characterize the effects of blindness on primary auditory cortex within a group of individuals with early blindness, including a subset of individuals with anophthalmia, in whom the eyes fail to develop. In blind individuals, we see evidence for a more refined representation of auditory frequency within auditory cortex.

3.2 Materials and Methods

3.2.1 Participants

Appendix A.1 provides subject details. Data were collected at two research sites: the University of Washington (UW; Seattle) and Oxford University (Oxford, UK). At the UW, data were collected using two protocols (static and motion, described below). Four early blind individuals (2 females) and four age-matched controls (static: 2 females; motion: 3 females) completed both the static and motion protocols. Two control subjects were repeated across protocols, whereas the remaining control subjects completed one protocol or the other, due to scheduling constraints.

At the University of Oxford, data were collected using the motion paradigm with participants with anophthalmia ($N = 5$, 1 female) and an age-matched control group ($N = 9$, 3 females). All subjects reported normal hearing, and no history of neurological or psychiatric illness.

At each site, the study was approved by the Institutional Review Board, and all subjects provided written informed consent.

3.2.2 MRI

Overhead lighting was dimmed during MRI acquisition, and subjects were instructed to keep their eyes closed throughout testing. Foam padding was used to minimize head motion. A closed-circuit camera system was used to monitor compliance, and all subjects successfully followed instructions and kept eyes closed during all functional scans.

3.2.3 Acquisition Protocol

UW data were collected using a 3T Achieva scanner (Philips) at the UW Diagnostic Imaging Sciences Center using a 32-channel head coil. In the static session, four functional scans were acquired using a standard EPI sequence (36 slices, TR/TE = 2000/25 ms, flip angle = 80°, no slice gap). After discarding the first 5 timeframes, each scan consisted of 255 volumes at an effective voxel size of 3 mm^3 isotropic (FOV = 240 × 240 × 108 mm^3, matrix size = 80 × 80 × 36). In the motion session, 4 functional scans were acquired using a standard EPI sequence (30 slices, TR/TE = 2000/25 ms, flip angle = 80°, no slice gap). After discarding the first 5 timeframes, each scan consisted of 144 volumes at an effective voxel size of 2.75 × 2.75 × 3.00 mm^3 (3 mm in-plane; FOV = 220 × 220 × 90 mm^3, matrix size = 80 × 80 × 30).

Oxford data were acquired with a 7T scanner (Siemens) at the Oxford Centre for Functional MRI of the Brain using a 32-channel head coil. In each session, six functional scans were acquired using a multishot EPI sequence (64 slices, TR/TE = 2488/27.8 ms, flip angle = 85°, no slice gap) with in-plane acceleration using parallel imaging (GRAPPA factor = 2; Griswold et al., 2002) and through-slice acceleration using multiband imaging (MB factor = 2; Moeller et al., 2010). Each scan consisted of 116 volumes at an effective voxel size of 1.2 mm^3 isotropic (FOV = 192 × 192 × 76.8 mm^3, matrix size = 160 × 160 × 64).

3.2.4 Auditory Stimulus Creation

Auditory stimuli were generated in MATLAB (The MathWorks) using the Psychophysics Toolbox (www.psychtoolbox.org) and custom MATLAB software, and were delivered via insert earphones. Auditory stimuli were delivered using MR-compatible Sensimetrics S14 earphones (Sensimetrics) at both research sites.

All stimuli were presented at a sampling rate of 44.1 kHz. Auditory calibration was performed using a standard, two-step procedure. We began by compensating for frequency-specific distortions in the earphone output, adjusting stimulus intensities to ensure flat frequency transmission from 100 Hz to 8 kHz. Next, stimulus sound intensities were adjusted according to a standard equal-loudness curve created for insert earphones (ISO 226) to approximate equal perceived loudness across frequency. Actual sound intensities (65–83 dB SPL) were matched to the perceived loudness of a 1 kHz tone (reference frequency) at 70 dB SPL. Acoustic noise from the scanner was attenuated by expanding-foam ear-tips, as well as protective earmuffs placed over the ear following earphone insertion. Subjects confirmed that all tones were clearly audible, and of approximately equal loudness across the frequency range.

3.2.5 Auditory Stimulus and Task

As described in Appendix A.1, all 4 early blind UW subjects participated in both the static and the motion protocols. All 5 Oxford anophthalmic subjects only participated in the motion protocol.

Motion Stimuli

Stimuli consisted of bandpass noise burst pairs centered at each of 7 frequencies (100–3162 Hz, stimulus bandwidth of ~ 0.8 octaves), presented in pseudo-randomized blocks that lasted 2 s. The auditory motion within each block was simulated using interaural time difference and consisted of a pair of identical 1 s bursts (treated as a single event) traveling at 30 m/s

from left to right, or vice versa, along a fronto-parallel plane 10 m in front of the listener. Subjects were asked to monitor the stimulus frequency and report via button press each time the same exact frequency-band noise burst pair was repeated (1-back task, 10% of trials). The task ensured that the subjects maintained attention for the duration of the scan. Catch trials were included in all analyses.

Static Stimuli

Stimuli were blocks of pure tone bursts, which varied in auditory frequency (88–8000 Hz, sampled in half-octave steps). Each 2 s stimulus block contained eight pure tone bursts of the same frequency. Tone durations were alternated in pseudorandomized order, switching durations at least 4 times during each 2 s block, resulting in a "Morse code"-like pattern of long and short tones, which served to increase the perceptual salience of the stimuli over the regular pattern of background scanner noise (Da Costa et al., 2011; Thomas et al., 2015).

Each run consisted of a series of sequences of 3–4 ascending or descending half-octave steps, with the starting frequency and sequence (ascending vs descending) selected pseudo randomly at the beginning of each sequence. The pseudo randomization ensured that the distribution of presented frequencies between 88 and 8000 Hz was uniform, and that there were equal numbers of ascending and descending sequences. Subjects were asked to monitor the stimulus frequency and report via button press each time the same exact frequency was repeated (1-back task, 10% of trials). The task ensured that the subjects maintained attention for the duration of the scan. Catch trials were included in all analyses.

3.2.6 MR Data Preprocessing

Standard preprocessing of fMRI data was performed using BrainVoyager QX software (version 2.3.1, Brain Innovation; Goebel et al., 2006), including slice scan time correction, 3D motion correction, and temporal high-pass filtering (cutoff = 2 cycles). Parameters generated during motion correction were recorded to ensure that subject motion within a scan did not account for pRF tuning parameters, as described below.

Functional data were aligned to the T1-weighted anatomical image acquired in the same session (MPRAGE, 1 mm^3) and resampled to 3 mm^3 resolution. The BrainVoyager QX automatic segmentation routine was used to reconstruct the cortical surface at the white-gray matter border (with hand-editing to minimize segmentation errors) and the resulting smooth 3D surface was partially inflated.

3.2.7 ROI Selection

Auditory cortex borders were drawn generously based on purely anatomical criteria to include all voxels within a contiguous region of auditory cortex between the lateral border on the crown of the superior temporal gyrus, the medial border within the fundus of the lateral sulcus, the posterior border of the supramarginal gyrus, and the anterior border of the most anterior portion of the temporal lobe.

The primary auditory cortex (PAC) ROI was defined using a combination of anatomical and functional criteria (Thomas et al., 2015). For simplicity, we refer here to the pair of tonotopic gradients comprising hA1 and hR as PAC. In primates, the auditory core area contains up to three tonotopic subdivisions, A1, R, and RT (Hackett, 2008; Hackett et al., 1998), which have been localized to the medial two-thirds of Heshl's gyrus (Dick et al., 2012; Rademacher et al., 2001). Human neuroimaging studies have identified at least two tonotopic gradients, presumed to be the human homologs of areas A1 and R (Da Costa et al., 2011, 2015; Formisano et al., 2003; Humphries et al., 2010; Langers & van Dijk, 2011; Moerel et al., 2012; Striem-Amit et al., 2011; Thomas et al., 2015). We identified PAC as consisting of two mirror-symmetric tonotopic gradients, meeting at a low-frequency reversal on the crown of Heschl's gyrus. Based on this tonotopic map and the underlying anatomy, for each subject, a PAC ROI was defined as a contiguous patch of cortical surface spanning Heschl's gyrus and containing both tonotopic gradients. Anterior and posterior borders were drawn along the outer high-frequency representations of the tonotopic maps, and lateral and medial borders were conservatively drawn to include only the medial two-thirds of Heschl's gyrus. Although this ROI selection method cannot isolate auditory core from auditory belts

areas that share the same tonotopic gradients, it does provide a consistent PAC definition for individual subjects across distinct acquisition and stimulus types (Da Costa et al., 2015; Thomas et al., 2015).

Large regions outside PAC also show evidence of frequency tuning. However, because there is still uncertainty about how tuning profiles relate to subdivisions of secondary auditory areas (Barton et al., 2012; Moerel et al., 2014; Santoro et al., 2017; Schönwiesner & Zatorre, 2009), we treat regions outside PAC as a single ROI. Our secondary auditory areas ROI was simply defined as voxels within the auditory cortex ROI that were not within PAC.

3.2.8 Population Receptive Field Analysis

Preprocessed fMRI data were analyzed using methods described in detail in Thomas et al. (2015). In brief, we assumed a Gaussian sensitivity profile of unit amplitude on a log auditory frequency axis for each voxel. Using custom software written in MATLAB, we found, for each voxel, the center (f_0) and SD (σ) of the Gaussian that when multiplied by the stimulus over time and convolved with an HRF (see below) produced a predicted time course that best correlated with the voxel's measured time course. For each voxel, the best-fitting value of f_0 is interpreted as that voxel's preferred frequency, while the best-fitting value of σ is interpreted as the tuning bandwidth.

Based on Boynton et al., 1996, we modeled the auditory HRF as a gamma function, with initial parameters $n = 3$, tau (τ) $= 1.5$, and delay (δ) $= 1.8$. We then used an iterative procedure to obtain individual HRF estimates. For each subject, we iteratively looped three times between two steps: (1) optimizing f_0 and σ while holding HRF parameters fixed, (2) optimizing τ and δ while holding f_0 and σ fixed. This HRF optimization was only performed on a subset of the data, using voxels with an initial fitted correlation value > 0.25. Median τ and δ parameters were used to approximate each individual's HRF across the entire auditory cortex ROI. We then refit the pRF parameters (f_0 and σ) for all voxels within the auditory cortex ROI, using these individually fitted HRF parameters. After finding the best fitting values of f_0 and σ, we used linear regression to find the amplitude value, a, that minimized

the root mean square error between predicted and obtained time courses.

After fitting, only voxels that met the following criteria were retained for further analysis: (1) the correlation between the observed fMRI time course and the time course predicted by the best-fitting pRF (our goodness-of-fit index) was > 0.20; (2) the center (f_0) of the best fitting pRF fell within the range of tested values (44–16,000 Hz for the static stimulus; and 50–6324 Hz for the motion stimulus); and (3) the SD (σ) of the best fitting pRF was > 0.1 $\log_{10}$ units and < 2 $\log_{10}$ units. For comparison, the presented frequencies in the static condition were separated by 0.15 $\log_{10}$ units, and each motion band center was separated by 0.25 $\log_{10}$ units. (4) Because amplitude values were positively skewed, we identified pRF fits with outlying amplitude values nonparametrically. We excluded voxels where the amplitude of the best fitting pRF did not fall between $(Q1 - 3 \times IQR)$ and $(Q3 + 3 \times IQR)$, where $Q1$, and $Q3$ refer to the first and third quartiles, and IQR is the interquartile range. Within PAC, acceptable amplitudes fell between 0 and 6.1414 (6.8945% of voxels excluded). Within secondary cortex, acceptable amplitudes fell between 0 and 5.4163 (3.2319% voxels excluded).

3.2.9 Statistical Analyses

Estimating pRF Fit Significance

pRF model fits were compared against a null model created using a randomized stimulus representation. In the case of the static stimulus, to preserve the temporal structure within individual stimulus blocks, we randomized the stimulus block order while retaining the ascending or descending series structure within each block. For each permutation, we calculated the false discovery rate based on $r > 0.2$, μ, σ, and a within acceptable ranges, as described in Materials and Methods. False discovery rates were calculated based on 100 permutations. Within auditory cortex, collapsed across all subjects and datasets; this stimulus-label permutation generated a mean false discovery rate of 11.2617% for a correlation threshold of $r > 0.2$. This threshold excluded voxel responses that were clearly noise.

Group Differences

Group differences were assessed using multifactor ANOVA using MATLAB and the Statistics Toolbox (Release 2016a). Datasets (UW static, UW motion, Oxford motion), group (blind vs sighted), and hemisphere (when included) were treated as independent variables. In all cases, we tested for the normality of the residuals with visual inspection and the Shapiro–Wilk test for normality.

For ANOVAs containing all three datasets, we first performed exploratory analyses using the 4 early blind and 2 sighted subjects who participated in both the static and the motion conditions as separate subjects. We then confirmed that the presence of these repeated subjects was not statistically critical by performing separate ANOVAs on the motion datasets only (which contained no repeated subjects). The results for the motion dataset only analyses are reported whenever they differed from those obtained using all three datasets.

Comparisons of pRF frequency distributions of across groups were performed using a bootstrapping procedure, based on the χ^2 test of independence. This test compares the obtained frequency distributions for each group with those that would be obtained if the frequency distribution were independent of group assignment. Significance values were obtained by comparing the real χ^2 values with those obtained by bootstrapping simulated distributions, created using random assignment of subjects across the two groups (1000 simulations).

Comparison across Datasets

To minimize site-based differences, an individualized HRF was estimated for each subject before pRF fitting, as described above (Thomas et al., 2015). pRF model estimates of tuning parameters f_0 and σ are expected to be reasonably robust to differences in SNR associated with collecting data at both Oxford and UW. Amplitude values, a would be expected to differ significantly across different protocols (motion vs static), MR imaging protocols or site.

Differences between motion and static stimuli could also potentially influence estimates of

f_0 and σ. For the motion stimulus, we used a more restricted stimulus set that spanned seven frequency bands, within a range of frequencies for which interaural time difference cues are equally strongly effective, so pRF estimates of f_0 could only reliably be estimated within a smaller frequency range. The reduced frequency range of the motion stimulus would also be expected to increase uncertainty in the estimate of σ, especially for smaller values. Finally, it is possible that interactions between motion sensitivity and frequency tuning could alter pRF estimates across the two stimuli due to recruitment of different neuronal populations.

3.3 Results

Figure 3.1 shows tonotopic maps in auditory cortex for 4 example subjects. Tonotopic organization did not differ significantly across datasets: for subjects who participated in both UW motion and UW static scans the mean voxelwise cross-correlation (Pearson's r) between the two datasets was 0.7457 in PAC and 0.4874 in secondary AC, values similar to previous studies examining replicability across different stimulus and acquisition protocols on the same UW scanner (Thomas et al., 2015).

3.3.1 Auditory Cortex Size

As described in the Introduction, previous MEG results have suggested that early blindness may result in a 1.8-fold expansion of early auditory areas (Elbert et al., 2002), although a reduction in the number of frequency selective voxels in auditory cortex has also been reported (Stevens & Weaver, 2009).

We began by examining PAC size by using all the voxels within the hand-drawn PAC ROI as our dependent measure. Group differences were assessed using an ANOVA with dataset, hemisphere, and blindness as fixed effects and the number of voxels within PAC as the dependent measure. This revealed an effect of dataset ($F(2, 48) = 17.45$, $p < 0.0001$), but no effect of blindness ($F(1, 48) = 0.86$, $p = 0.3579$), or hemisphere ($F(1, 48) = 0.02$, $p = 0.878$). There was a significant interaction between blindness and dataset ($F(2, 48) = 3.71$, $p = 0.0319$). A post hoc Tukey–Kramer test showed that the UW static dataset resulted

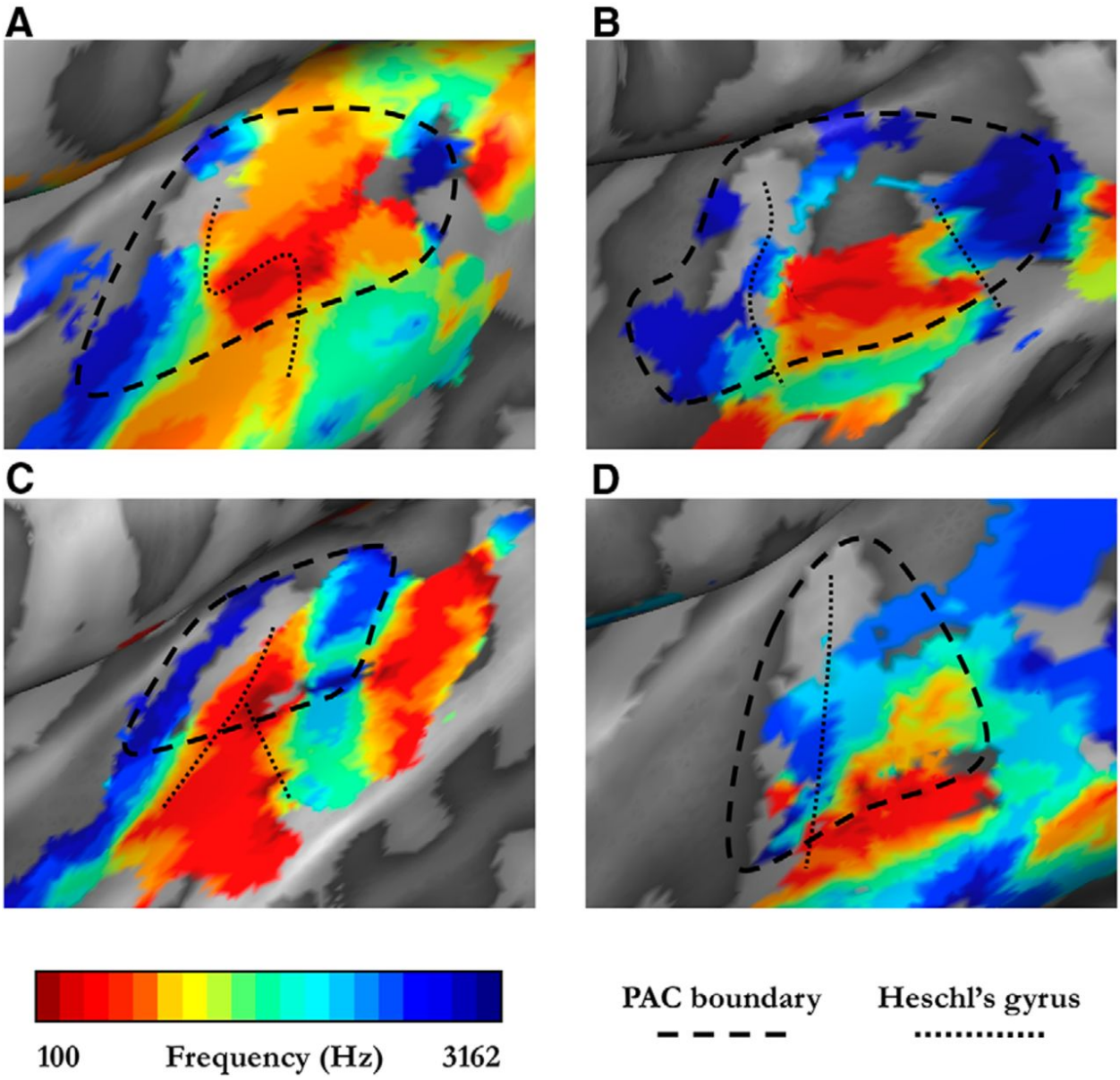

Figure 3.1: Tonotopic maps in auditory cortex. pRF frequency estimates (for successfully fitted voxels, see Materials and Methods) are shown for the left hemisphere for 2 sighted subjects (A, B), and example individuals who were early blind (C) or anophthalmic (D). Maps are shown for both the static (A, C) and the motion (B, D) stimulus. Black dashed line indicates the estimated boundary of PAC for each subject. Black dotted line indicates the location of Heschl's gyrus. To maximize visual similarity, given that the motion stimulus had a smaller frequency range (100–3162 Hz) than the static stimulus (88–8000 Hz), the color map is restricted to the frequency range of the motion stimulus.

in a significantly larger definition of PAC than both the UW motion and Oxford motion datasets. This might be due to a difference in scanner quality, voxel acquisition size, and/or stimuli (e.g., the wider frequency range). No other interactions were significant.

We also assessed group differences in the number of voxels which were successfully fit in PAC and secondary auditory areas ($r > 0.2$, μ, σ, and a within acceptable ranges, as described in Materials and Methods). In the early blind/anophthalmic group, the mean number of successfully fit voxels in the UW static, UW motion, and Oxford motion conditions were 191, 208.25, and 52.8, respectively. In the control group, the mean number of voxels were 147.75, 167.5, and 113.33, respectively. We found no evidence for an effect of blindness on the number of frequency-tuned voxels within either PAC or secondary auditory areas.

Within PAC, we once again found an effect of dataset ($F(2, 48) = 9.97$, $p = 0.0002$), but no effect of blindness ($F(1, 48) = 0.13$, $p = 0.7241$) or hemisphere ($F(1, 48) = 0.11$, $p = 0.7461$). No other interactions were significant. Within secondary auditory areas, we found an effect of dataset ($F(2, 48) = 7.06$, $p = 0.002$), but no effect of blindness ($F(1, 48) = 0.46$, $p = 0.5021$) or hemisphere ($F(1, 48) = 0.19$, $p = 0.6681$). No interactions were significant. For both PAC and secondary auditory areas, post hoc Tukey–Kramer tests suggested that the effect of dataset was driven by a smaller number of voxels within PAC passing threshold for Oxford anophthalmic individuals. This was likely due to an interaction between reduced signal-to-noise in the Oxford dataset (due to the smaller acquisition voxel size) and lower pRF amplitudes in blind individuals, see below.

3.3.2 HRFs

A wide variety of studies have found metabolic differences in occipital cortex between early blind and sighted individuals (Coullon et al., 2015; De Volder et al., 1997; Veraart et al., 1990; Wanet-Defalque et al., 1988; Weaver et al., 2013). To examine potential differences in auditory cortex hemodynamics across blind and sighted subjects, we performed a mixed-design ANOVA with dataset and blindness as fixed effects and the time-to-peak of the estimated HRF as the dependent measure. We found no main effect of dataset ($F(2, 24) =$

0.08, $p = 0.9197$), no effect of blindness ($F(1, 24) = 0.21$, $p = 0.6479$), and no significant interactions on the time-to-peak of the hemodynamic function within the auditory cortex ROI.

3.3.3 Response Amplitudes

As described in the Introduction, a number of studies report an attenuated response to pure tone stimuli versus silence in the temporal lobe of blind individuals (Gougoux et al., 2009; Stevens & Weaver, 2009; Watkins et al., 2013) when comparing responses with pure tones versus silence (GLM: sound versus silence).

As shown in Figure 3.2A, C, we find that early blind and anophthalmic participants have significantly smaller β weights than sighted subjects, within both PAC and secondary auditory areas. Within PAC using a mixed-design ANOVA with dataset, hemisphere, and blindness as fixed effects and the GLM response to sound versus silence as the dependent measure, we found no main effect of dataset ($F(2, 48) = 1.56$, $p = 0.2197$), an effect of blindness ($F(1, 48) = 5.63$, $p = 0.0218$), no effect of hemisphere ($F(1, 48) = 0.01$, $p = 0.9366$), and no significant interactions. Within secondary auditory cortical areas, we found no main effect of dataset ($F(2, 48) = 0.92$, $p = 0.4039$), a marginally significant effect of blindness ($F(1, 48) = 3.66$, $p = 0.0618$), no effect of hemisphere ($F(1, 48) = 0.05$, $p = 0.824$), and no significant interactions.

3.3.4 pRF Model Response Amplitudes

One concern is that β weights for pure tones versus silence might potentially reflect narrower tuning (as found for our blind individuals, see below) rather than reduced responsiveness; narrower tuning would be expected to result in a smaller region of cortex responding to any given narrowband stimulus, thereby reducing measured activation in a GLM model. An advantage of our pRF approach is that it separately represents tuning width and response amplitude. As shown in Figure 3.2B, D, pRF response amplitudes are smaller in blind versus sighted subjects within both PAC and secondary auditory cortex. Group differences in pRF

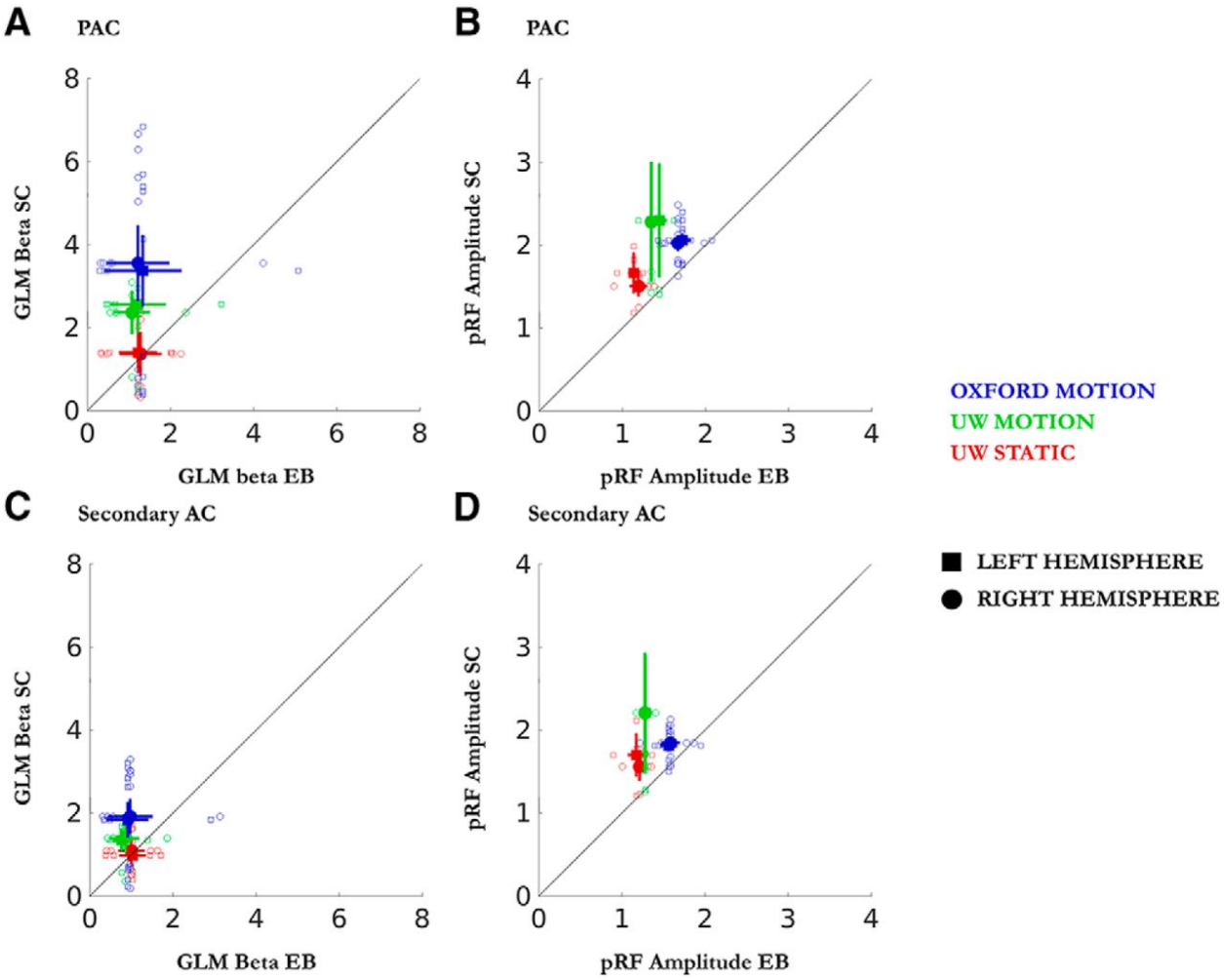

Figure 3.2: Response amplitudes in auditory areas. Blue represents Oxford motion results. Green represents UW motion results. Red represents UW static results. Square and circular symbols represent left and right hemispheres, respectively. (A) PAC GLM results. x and y axes represent mean blind and sighted subject β weights, respectively. (B) PAC pRF results. x and y axes represent mean blind and sighted subject pRF amplitudes, respectively. (C, D) Secondary auditory cortex GLM and pRF results. Error bars indicate single SEM.

amplitudes were assessed using an ANOVA with dataset, hemisphere, and blindness as fixed effects and pRF amplitude as the dependent measure. Within PAC, this revealed a main effect of dataset ($F(2, 46) = 3.92$, $p = 0.0268$), an effect of blindness ($F(1, 46) = 12.8$, $p = 0.0008$), no effect of hemisphere ($F(1, 46) = 0.11$, $p = 0.7468$), and no significant interactions. A post hoc Tukey–Kramer test showed that the UW static dataset resulted in a significantly smaller pRF response amplitudes than the Oxford motion dataset. This could be due to a difference in scanner quality, voxel acquisition size, and/or stimuli.

Within secondary auditory areas, we found no main effect of dataset ($F(2, 46) = 1.62$, $p = 0.2098$), an effect of blindness ($F(1, 46) = 12.33$, $p = 0.001$), no effect of hemisphere ($F(1, 46) = 0$, $p = 0.9544$), and no significant interactions.

3.3.5 Frequency Distributions

The distribution of frequency preferences within PAC and secondary AC across early blind (red) and sighted subjects (gray) is shown in Figure 3.3. For each dataset, a bootstrapped χ^2 test of independence was used to examine the relation between blindness and the number of voxels in each frequency bin (6 bins for the motion datasets, 13 bins for the static dataset), by assigning subjects randomly across groups. Using this analysis, within PAC, we saw no effect of blindness on the distribution of frequency preferences for any of the three datasets: Oxford motion, $\chi^2(6, N = 14) = 77.3865$, $p = 0.2710$; UW motion, $\chi 2(6, N = 8) = 57.6207$, $p = 0.3330$; and UW static, $\chi 2(13, N = 8) = 117.6774$, $p = 0.3070$. Within secondary AC, we similarly found no effect of blindness on the distribution of frequency preferences: Oxford motion, $\chi 2(6, N = 14) = 87.5279$, $p = 0.2110$; UW motion, $\chi 2(6, N = 8) = 75.7219$, $p = 0.3590$; and UW static, $\chi 2(13, N = 8) = 93.8221$, $p = 0.1870$.

Previous work comparing scanner sequences that differed in their acoustic properties suggests that, although acoustic scanner noise does not result in noticeable systematic misestimation of frequency values near the peak of the scanner noise, it may reduce the number voxels that are successfully fit by the pRF model, thereby biasing the frequency distributions (Thomas et al., 2015). We therefore performed an additional post hoc χ^2 analysis of

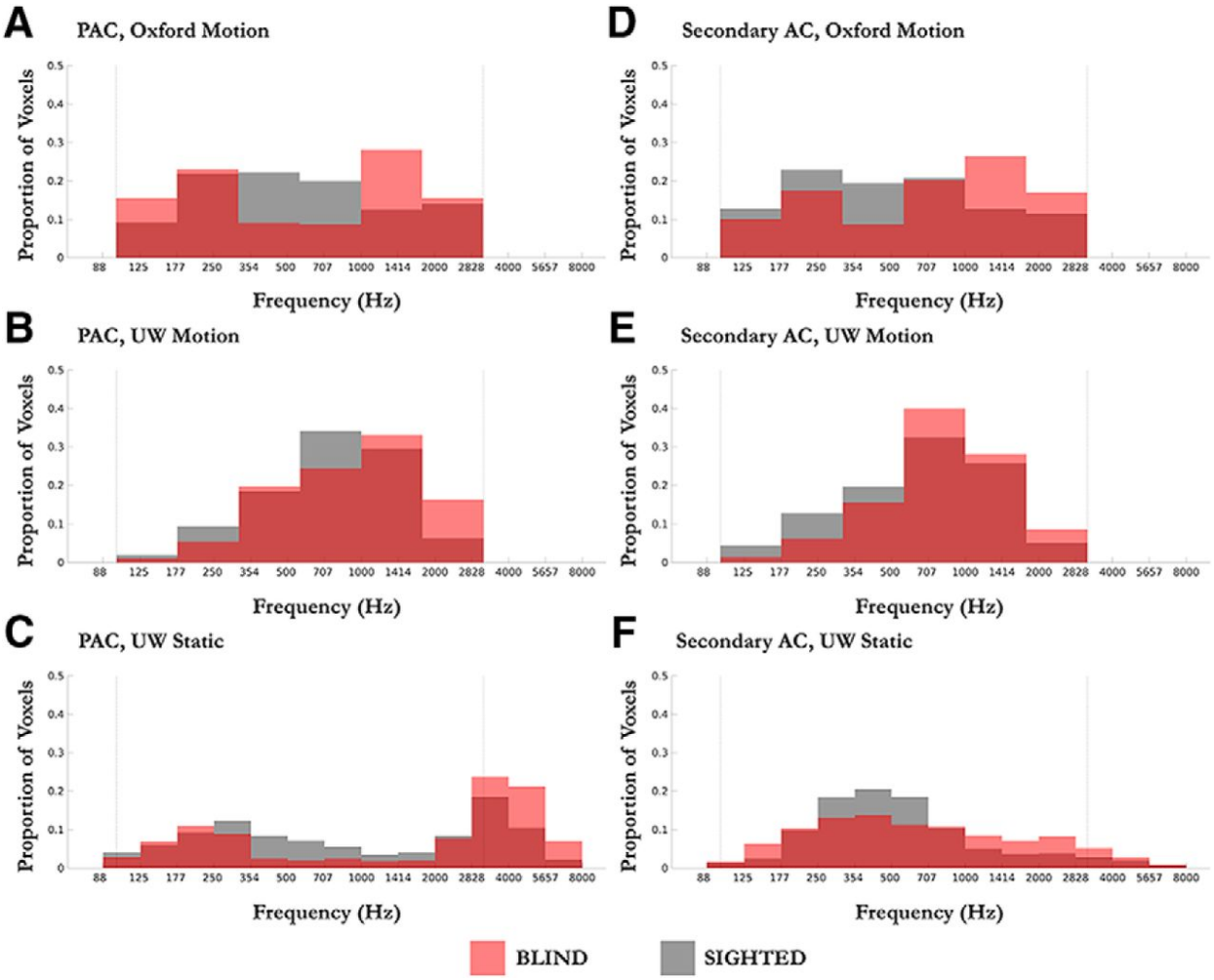

Figure 3.3: The proportion of voxels successfully fit using the pRF model by frequency, based on half-octave bins (6 bins for the motion datasets, 13 bins for the static dataset). Red represents blind subjects. Gray represents sighted subjects. (A–C) Probability distributions within PAC. (D–F) Probability distributions within secondary auditory areas. (A, D) Dotted lines indicate the frequency range that was shared across motion and static datasets.

independence examining whether the number of voxels falling inside or outside the 350–2000 Hz frequency range associated with masking by acoustic noise in the scanner was affected by blindness. Within PAC, we saw an effect of blindness only for the UW static dataset: Oxford motion, $\chi 2(1, N = 1284) = 0.5618$, $p = 0.4535$; UW motion, $\chi 2(1, N = 1503) = 2.0701$, $p = 0.1502$; and UW static, $\chi 2(1, N = 1355) = 73.1261$, $p = 0.0000$. Within secondary AC, we found an effect of blindness for all three datasets: Oxford motion, $\chi 2(1, N = 2062) = 11.3067$, $p = 0.0008$; UW motion, $\chi 2(1, N = 2257) = 12.6840$, $p = 0.0004$; and UW static, $\chi 2(1, N = 1898) = 10.8173$, $p = 0.0010$. This result might reflect a differential sensitivity to masking effects from scanner noise across blind and sighted populations. However, given that this effect was more consistently observed in secondary AC, it might also reflect a distribution of frequency preferences in blind subjects that is less heavily clustered toward frequencies in the 250–3000 Hz range (see Discussion).

3.3.6 Tuning Width

Tuning width for each voxel was characterized with Q as given by the following formula:

$$Q = \frac{f_0}{FWHM} \tag{3.1}$$

where the FWHM is the estimated Gaussian profile from the pRF model in frequency space. Figure 3.4 shows Q on the cortical surface in the same example subjects as shown in Figure 3.1.

To examine differences in tuning width across blind and sighted subjects, we performed an ANOVA with dataset, blindness, and hemisphere as fixed effects and Q value as the dependent measure. This was done using all successfully fitted voxels for both PAC and auditory cortex.

Within PAC, we found a main effect of dataset ($F(2, 46) = 27.28$, $p < 0.0001$), an effect of blindness ($F(1, 46) = 8.1$, $p = 0.0066$), no effect of hemisphere ($F(1, 46) = 0.56$, $p = 0.4569$), and no significant interactions. A post hoc analysis showed that blindness

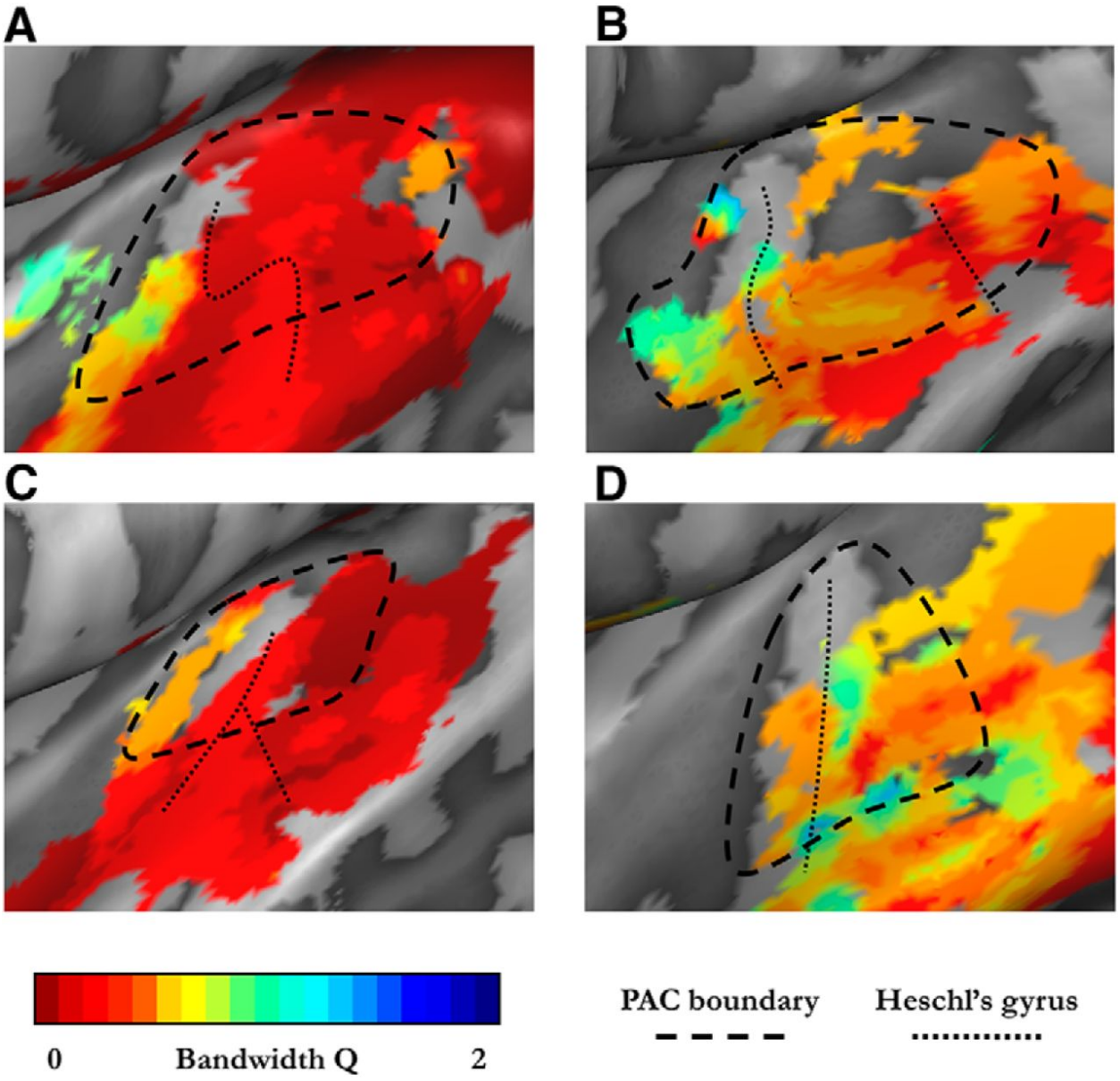

Figure 3.4: Tuning width maps in auditory cortex. Q estimates (for successfully fitted voxels, see Materials and Methods) are shown for the left hemisphere for 2 sighted subjects (A, B), and example individuals who are early blind (C) and anophthalmic (D). Maps are shown for both the static (A, C) and the motion (B, D) stimulus. Black dashed line indicates the estimated anterior/posterior boundary of PAC for each subject. Black markers represent the location of Heschl's gyrus.

resulted in significantly larger Q values (narrower tuning; Figure 3.5).

Within secondary auditory areas, we found a main effect of dataset ($F(2, 44) = 29.19$, $p < 0.0001$), no effect of blindness ($F(1, 44) = 3.55$, $p = 0.066$), no effect of hemisphere ($F(1, 44) = 1.12$, $p = 0.2954$), and no significant interactions. The larger Q size in anophthalmic subjects for the Oxford motion stimulus was marginally significant in either PAC and was nonsignificant in secondary auditory cortices, but may reflect a population difference that our sample size was too small to reveal.

For both PAC and secondary auditory cortical areas, post hoc Tukey–Kramer tests showed that the Oxford motion dataset resulted in significantly larger Q values than either of the other two datasets, as can be seen in Figure 3.5 This is likely due to the smaller acquisition voxel size in this dataset because a smaller voxel presumably reflects a more homogeneous neural population of tuning preferences (Dumoulin & Wandell, 2008).

Visual inspection and statistical analyses did not reveal any consistent relationship between tuning width (Q values) and frequency that was reliable across datasets, or reliably different across blind and sighted subjects.

Estimated population tuning widths are presumably influenced both by the breadth of underlying individual neural tuning curves and by the dispersion of frequency preferences within each voxel. For each voxel, we estimated "frequency dispersion" as the median difference in center frequency between that voxel and all adjacent voxels, normalized by the Euclidean distance in millimeters between the voxels on the cortical surface. Group differences were assessed using an ANOVA with dataset, hemisphere, and blindness as fixed effects and dispersion within PAC as the dependent measure. Within PAC, we found a main effect of dataset ($F(2, 45) = 71.73$, $p < 0.0001$), an effect of blindness ($F(1, 45) = 5.79$, $p = 0.0203$), no effect of hemisphere ($F(1, 45) = 0.21$, $p = 0.6527$), and a significant interaction between dataset and blindness ($F(2, 45) = 3.43$, $p = 0.0411$). No other interactions were significant. Within secondary auditory areas, we found a main effect of dataset ($F(2, 46) = 101.38$, $p < 0.0001$), no effect of blindness ($F(1, 46) = 0.39$, $p = 0.5353$), no effect of hemisphere ($F(1, 46) = 0.01$, $p = 0.9046$), and no significant interactions.

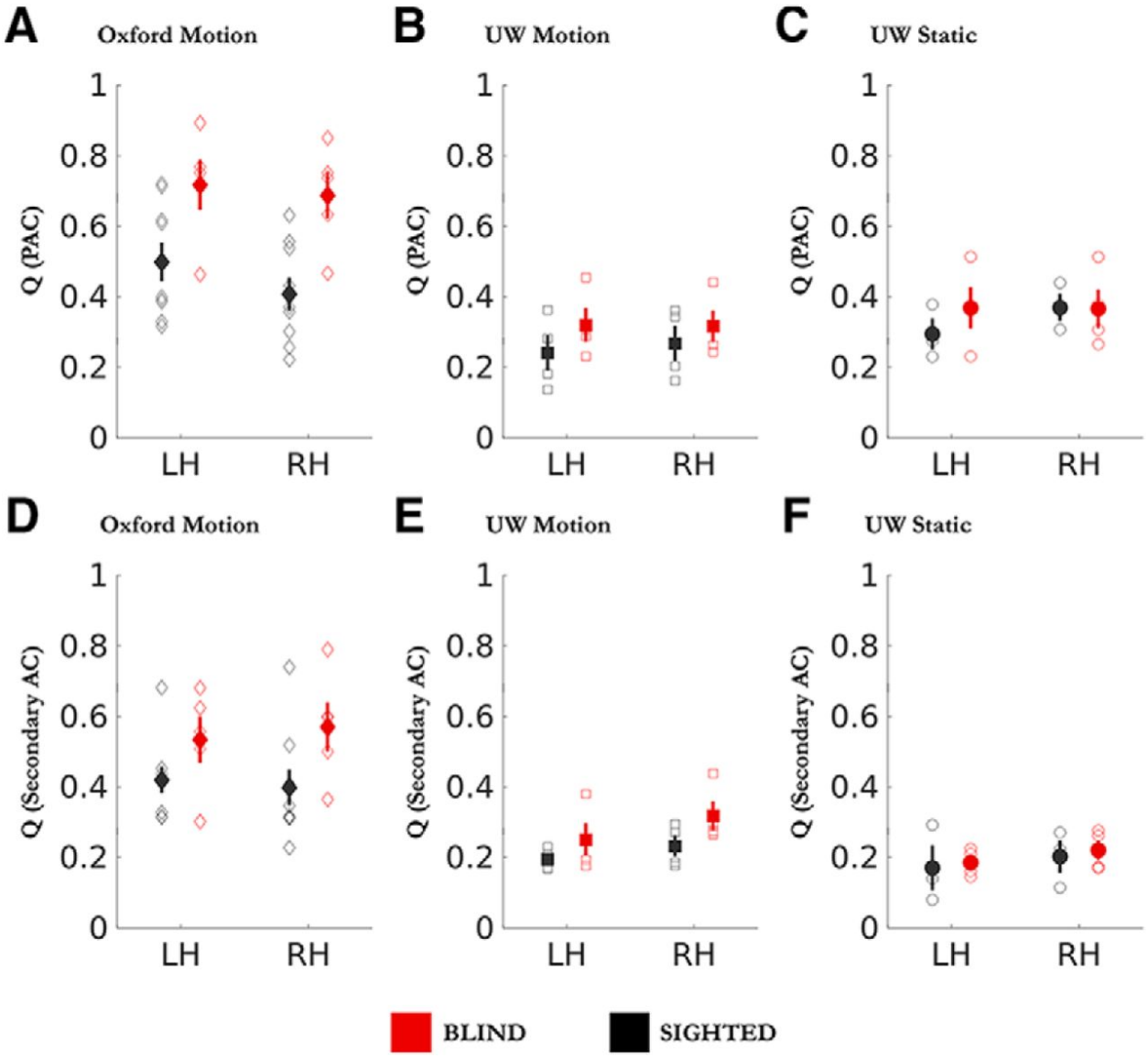

Figure 3.5: Mean pRF tuning width for each dataset within PAC (A–C) and secondary auditory cortex (D–F) for left (LH) and right (RH) hemispheres. Mean pRF size was calculated for each subject. Symbols represent group means with single SEMs calculated across subjects.

Finally, we examined whether differences in Q within PAC could be explained by differences in frequency dispersion using multivariate linear regression with dataset, hemisphere, frequency dispersion, and blindness as fixed effects and Q as the dependent measure. As might be expected, frequency dispersion was a strong predictor of Q ($b = -1.5799$, $p < 0.0001$), with high dispersion values predicting low Q values. However, we still found significantly higher Q values in blind individuals ($b = 0.1446$, $p < 0.0001$), even after including frequency dispersion as an independent factor.

3.4 Discussion

Here we examined whether blindness early in life alters the representation of frequency information within auditory cortex. Using an adaptation of the population receptive field model, we were able to disentangle voxel level tuning widths from response amplitudes. We find evidence that early blindness results in narrower bandwidths, reduced pRF amplitudes, and may alter the distribution of frequency preferences within auditory cortex. We did not see any effect of blindness on the size or the hemodynamic responsivity of PAC and secondary AC.

3.4.1 Auditory Cortex Size

Here, we failed to find evidence for an expanded tonotopic representation of PAC or secondary auditory areas as suggested by previous MEG data (Elbert et al., 2002). One possibility is that the apparent increase in source separation of high and low frequencies in early blind subjects that was noted previously by Elbert et al. (2002) was driven by differences in tuning bandwidth. Broader bandwidths in sighted subjects would be expected to result in a correspondingly larger cortical area of activation for any given auditory frequency. This might, in turn, have reduced the apparent source separation of high and low frequencies (Josef Golubic et al., 2011). Moreover, the known variability in cortical folding within Heschl's gyrus (Da Costa et al., 2011) would be expected to complicate estimates of PAC size, especially given that dipole estimates in the study by Elbert et al. (2002) were based

on a best fitting local sphere rather than individual anatomies. However, it remains possible that a future study with a larger sample might reveal subtle differences in the structure of PAC and/or secondary AC. Indeed, Atilgan et al. (2017) recently reported reduced surface area in subregions of secondary auditory cortex for congenitally blind subjects, along with evidence for greater bilateral similarity between cortical thickness and surface area in both early and late blind subjects throughout the entire superior temporal plane.

3.4.2 Response Amplitudes

A number of previous studies have reported an attenuated response to pure tone stimuli versus silence in the temporal lobe of blind individuals (Gougoux et al., 2009; Stevens & Weaver, 2009; Watkins et al., 2013) when comparing responses to pure tones versus silence. Reduced responses have been interpreted as reduced participation in auditory processing, perhaps due to increased "efficiency" of processing within the intact modality or due to function being "usurped" by a reorganized occipital cortex (Dormal et al., 2015; Jiang et al., 2014). One concern is that these previous results might have reflected narrower tuning rather than reduced responsiveness because narrower tuning would be expected to result in a smaller of region of cortex responding to any given narrowband stimulus, which would reduce the measured activation in a sound versus silence GLM. If blind individuals have neurons that are more narrowly tuned for more complex spectrotemporal modulations (more specialized "feature detectors"), this would reduce the population response to any given pure tone or bandpass stimulus. It is known that secondary auditory areas contain neurons that have multidimensional tuning that reflect complex spatiotemporal properties of the stimulus (Allen et al., 2018; De Angelis et al., 2018; Moerel et al., 2013, 2018; Santoro et al., 2014, 2017; Schönwiesner & Zatorre, 2009), and previous work suggests an increase in the proportion of spatially tuned cells within anterior auditory association areas in visually deprived cats (Korte & Rauschecker, 1993). An advantage of our pRF approach is that it allows an independent representation tuning width and response amplitude. Here, we replicated previous findings showing reduced β weights, and similarly found reduced pRF

amplitudes as a result of early blindness. We then separately examined frequency tuning bandwidth in each group, as described below.

3.4.3 Frequency Distributions

Previous work in monkeys has shown that frequency representations within PAC can be altered by experience (Recanzone et al., 1992, 1993), with a shift toward trained frequencies. Given that blind subjects rely on auditory frequency for a wider range of tasks than sighted individuals, we thought it possible that we might see a difference in frequency representations across the two groups. In our initial analysis, we did not see evidence for an alteration in the distribution of frequency preferences as a result of blindness within either PAC or secondary auditory areas. However, a post hoc analysis revealed fewer voxels falling in the 350–2000 Hz range within PAC for the UW static dataset, and for all three datasets within secondary AC. This result might reflect a differential sensitivity to masking effects of acoustic scanner noise across blind and sighted populations. However, given that this effect was more consistently observed in secondary AC, it might also reflect a distribution of frequency preferences in blind subjects that is less heavily clustered toward frequencies that fall in the 250–3000 Hz range, perhaps driven by the use of auditory cues with broad spectral content, such as acoustic echoes produced by mouth sounds or a cane (Norman & Thaler, 2017).

3.4.4 Tuning Width

Blind individuals had significantly narrower voxelwise tuning for auditory frequency within both left and right PAC. We do not believe that the narrowing in pRF tuning width within PAC that we observed in blind individuals was due to differences in the gradient of preferred frequency across the cortical surface. As described above, both PAC/auditory cortex size and the dispersion of frequencies within PAC were similar across both subject groups, and visual inspection revealed no systematic gradient differences. Nor, given the similarity in the measured hemodynamic responses between our subject groups, do we believe that these differences are due to group differences in hemodynamic coupling. It seems more likely

that our PAC results either reflect (1) a narrowing in the tuning bandwidth of individual neurons or (2) a more refined local organization, such as a reduction in the amount of scatter in frequency preference across a scale of < 3 mm. Consistent with the notion that these differences might reflect differences in neural tuning within individual neurons, Petrus et al. (2014) have shown that adult-onset visual deprivation over 6–8 d sharpens the frequency tuning of individual neurons within A1 in the mouse. Moreover, the same brief period of visual deprivation leads to more refined interlaminar connections (Meng et al., 2015, 2017), highlighting the capability for rapid remodeling of auditory frequency representations, even after the closure of the canonical critical period.

We did not see differences is tuning bandwidth within secondary AC as a result of early blindness. However, we used relatively simple stimuli and a simple Gaussian pRF model, and these areas are known to have complex spectrotemporal tuning functions (Barton et al., 2012; Moerel et al., 2013, 2014, 2018; Santoro et al., 2014, 2017; Schönwiesner & Zatorre, 2009). Future work, using more naturalistic stimuli and more complex analysis models, will be important for more fully characterizing the effects of blindness on auditory tuning in these secondary areas.

In conclusion, here we provide some of the first evidence for systematic changes in neural tuning within human auditory cortex as a result of blindness. It remains to be seen whether the changes described here reflect a developmental adaptation to early blindness, the ongoing effects of visual deprivation, and/or differential auditory demands that result from being blind. Future work could examine these questions by addressing whether adult-onset blindness, short-term visual deprivation, and/or auditory training can alter frequency tuning within auditory cortex, and whether, in adult sight-recovery subjects, the effects of long-term visual deprivation on auditory cortex are reversed with the reinstatement of vision.

Chapter 4

OPTIMIZING RELIABILITY AND MEASUREMENT OF POPULATION RECEPTIVE FIELDS IN HUMAN VISUAL CORTEX

4.1 Introduction

A fundamental component of vision research using functional magnetic resonance imaging (fMRI) is the investigation of functional organization within visual cortex known as retinotopic organization. In the last two decades, population receptive field (pRF) mapping (Dumoulin & Wandell, 2008) has emerged as the leading retinotopic mapping technique. Using the pRF method, it has become possible to estimate individual retinotopic maps of pRF location and size.

The pRF model has seen numerous applications in research such as examining spatial attention dynamics (Kay et al., 2015; B. P. Klein et al., 2014; Sprague & Serences, 2013), changes due to neural plasticity (Baseler et al., 2011; Haak et al., 2012; Huber, Chang, et al., 2019), and assessing clinical diagnoses (Brewer & Barton, 2012; Schwarzkopf et al., 2014). The pRF method has become a useful tool because pRF estimates can be used to make inferences about the mapping between neuronal computation and the physical world. For the applications of the pRF model to be meaningful, we rely on the accuracy and stability of the pRF model estimates.

Previous work has investigated the stability of pRF estimates and shown that pRF location estimates are highly stable (Benson et al., 2018; Senden et al., 2014; van Dijk et al., 2016; Zeidman et al., 2018). However, pRF size estimates were shown to be less stable under different retinotopic mapping conditions, such as stimulus configurations (Alvarez et al., 2015; Binda et al., 2013; Infanti & Schwarzkopf, 2020; Linhardt et al., 2021) and model

fitting procedures (Lage-Castellanos et al., 2020; Zeidman et al., 2018).

There are two major hypotheses as to why the instability occurs for pRF size estimates. The first hypothesis supposes that the spatio-temporal properties of the mapping stimulus introduce nonlinearities into the fMRI signal that the pRF model is unable to account for, such as top-down influences (Binda et al., 2013; Infanti & Schwarzkopf, 2020; Senden et al., 2014). Under this logic, studies approached this issue by designing stimulus protocols that were spatio-temporally independent (Binda et al., 2013) or preferred randomized presentation sequences (Senden et al., 2014). A recent investigation by Infanti and Schwarzkopf (2020) revealed that spatio-temporal properties did influence pRF size estimates, but mostly due to the stimulation cycle duration rather than stimulus configuration.

The second hypothesis supposes that the relationship between pRF size, cortical magnification factor (CMF), and eccentricity, influences pRF size estimate stability (Alvarez et al., 2015; Linhardt et al., 2021). Cortical magnification is an organizational principle of visual cortex under which many neurons with small receptive fields are devoted to representing central vision and fewer neurons with larger receptive fields represent peripheral vision (Hubel & Wiesel, 1962, 1974). The relationship between CMF and eccentricity has been described as a logarithmic decay (Daniel & Whitteridge, 1961; Horton & Hoyt, 1991; Sereno et al., 1995) and the relationship between pRF size and eccentricity can be described as a linear increase (Dumoulin & Wandell, 2008). Both pRF size and CMF can be measured in humans with the pRF method (Clavagnier et al., 2015; Harvey & Dumoulin, 2011).

From these relationships, it could be inferred that smaller pRFs should have a different optimal stimulation pattern than larger pRFs. For example, within V1 there are pRFs that range from 0.25° to 1° in radius, which converts to a factor of 16 difference in covered area. Therefore, the amount and duration of stimulation required to elicit a stable fMRI response from a smaller pRF should be a scaled version of a stimulus that would evoke a similar response from a larger pRF. Under this logic, most pRF studies that used traditional retinotopic mapping stimuli with a fixed size would produce uneven stimulation across the visual field, resulting in unstable pRF estimates that are biased towards receptive field sizes

optimally matching the chosen stimulus size.

This logic could also explain why it has been difficult to estimate pRFs from foveal regions of interest. While it is possible to estimate pRFs that represent foveal vision, the pRF estimates located in foveal regions are often unreliable and have poor model fits (Linhardt et al., 2021; Schira et al., 2007). Given that the fovea is overrepresented in human primary visual cortex (Azzopardi & Cowey, 1993), if CMF is not accounted for, it is likely that a disproportionate number of larger pRFs would be overrepresented in successfully estimated pRFs due to poor signal from smaller pRFs.

One method used to address the relationship between pRF size, CMF, and eccentricity has been to combine stimulus configurations where each stimulus type is optimized for either smaller or larger pRFs (Benson et al., 2018; Linhardt et al., 2021). This method has shown success for estimating smaller pRFs, especially for central vision. However, it comes with a trade-off with acquisition time because of the additional run time to acquire multiple stimulus configurations. Another method has been to design stimuli scaled to match CMF. Previously explored CMF-scaled stimuli consist of a multifocal stimulus (Binda et al., 2013), combined wedge and ring stimuli, and logarithmically-scaled bar stimuli (Alvarez et al., 2015).

A multifocal stimulus chunks the visual field into sectors along the polar angle and CMF-scaled eccentricity steps and uses a m-sequence to determine which sectors are simultaneously presented to minimize spatio-temporal correlations (Binda et al., 2013; Vanni et al., 2005). The multifocal stimulus was able to produce smaller pRF estimates than a fixed size drifting bar stimulus but showed reduced goodness-of-fit for model performance. A multifocal stimulus also required longer presentation durations per stimulus frame to maximize signal-to-noise (SNR) which increased acquisition time. Alvarez et al. (2015) tested two CMF-scaled stimuli: (1) combined wedge and ring and (2) a logarithmically-scaled bar stimulus. The first stimulus type presented a rotating wedge and expanding/contract ring simultaneously rather than across separate runs. The second stimulus type presented a logarithmic bar that changed its width as a function of eccentricity. Only the logarithmic bar was able to produce smaller pRFs than the fixed size drifting bar stimulus across multiple visual areas, but it

also suffered from lack of goodness-of-fit for model performance. The authors scaled their logarithmic bar to mimic CMF, but the implementation scaled the entire bar width based on the bar's center eccentricity location. This choice meant that the portion of the stimulus that extended into the periphery was adjusted to match scaling for a location in the center of vision, which could explain the poor model fits.

I hypothesize that CMF has a significant influence on pRF size estimate stability. To test this hypothesis, pRF estimates in human early visual cortex are compared during the presentation of a fixed size drifting bar stimulus and a novel, logarithmically-distorted drifting bar stimulus. The distorted bar developed for this study warps the entire bar as a logarithmic function of eccentricity. This stimulus combined the best aspects of previously used stimulus configurations: (1) better model accuracy and reliability, like a drifting bar stimulus and (2) smaller pRF size estimates, like other CMF-scaled stimuli. Below, I present evidence that the fixed size drifting bar stimulus resulted in a systemic bias towards larger pRF sizes. The logarithmically-distorted bar produced more reliable pRF estimates as well as smaller pRF size estimates. These differences were especially prominent in regions of cortex that represented central vision across all visual areas. These results support the influence of cortical magnification on the fMRI response and pRF size estimate stability, as well as present an advancement towards an optimal pRF mapping procedure from which pRFs can be reliability measured.

4.2 Methods

4.2.1 Subjects

Retinotopic datasets were acquired for a total for 12 subjects (6 females, 6 males), ages 20 – 38 (M = 28.67, SD = 5.66). MRI data were acquired on a Siemens 3T Prisma with a 64-channel phase-array head coil at the University of Washington Center for Human Neuroscience (CHN). All subjects participated in 2 one-hour sessions of scanning within 1-2 weeks between each session. All participants had normal or corrected-to-normal visual

acuity.

4.2.2 MRI Acquisition

The protocol included a 3D multi-echo volumetric navigator guided T1-weighted (T1w) and T2-weighted (T2w) images acquired at 0.8 mm^3 isotropic resolution (FOV = 166.4 × 240 × 256 mm^3, matrix size = 208 × 300 × 320; Tisdall et al., 2012).

BOLD data was acquired using a T2*-weighted 2 mm^3 isotropic multiband gradient-echo (multiband acceleration = 4), echo-planar imaging sequences (TR/TE = 1200/30 ms, flip angle = 64° FOV = 212 × 212, matrix size = 106 × 106, 56 oblique axial slices). Each run collected 305 volumes (approximately 6.1 minutes) and subjects participated for a total of 12 runs with 6 runs per stimulus condition across two sessions. Additionally, a pair of opposite phase-encoded EPI references were acquired for each session.

4.2.3 Preprocessing

The dataset was processed using the fMRIPrep-21.0.1 pipeline (Esteban et al., 2019). The T1w image was corrected for intensity non-uniformity (INU) with N4BiasFieldCorrection (Tustison et al., 2010), distributed with ANTs 2.3.3 (Avants et al., 2008), and used as T1w-reference throughout the workflow. The T1w-reference was then skull-stripped with a Nipype implementation of the antsBrainExtraction.sh workflow (from ANTs), using OASIS30ANTs as target template. Brain tissue segmentation of cerebrospinal fluid (CSF), white-matter (WM) and gray-matter (GM) was performed on the brain-extracted T1w using FSL's fast segmentation tool (Zhang et al., 2001). Brain surfaces were reconstructed using FreeSurfer recon-all (Dale et al., 1999), and the brain mask estimated previously was refined with a custom variation of the method to reconcile ANTs-derived and FreeSurfer-derived segmentations of the cortical gray-matter of Mindboggle (A. Klein et al., 2017).

A B0-nonuniformity map (or fieldmap) was estimated based on two (or more) echo-planar imaging (EPI) references with topup from FSL (Andersson et al., 2003). A fieldmap was

estimated for each session and the correction was applied to all functional data within the collected session.

Head-motion parameters with respect to the BOLD reference were estimated before any spatiotemporal filtering using mcflirt (Jenkinson et al., 2002) and were expanded with the inclusion of temporal derivatives and quadratic terms for each parameter (Satterthwaite et al., 2013). The estimated fieldmap was then aligned with rigid-registration to the target EPI (echo-planar imaging) reference run. The field coefficients were mapped on to the reference EPI using the same transform. BOLD runs were slice-time corrected to 0.549 s (0.5 of slice acquisition range 0 s - 1.1 s) using 3dTshift from AFNI (Cox & Hyde, 1997). The BOLD reference was then co-registered to the T1w reference using bbregister (FreeSurfer) which implements boundary-based registration (Greve & Fischl, 2009). Co-registration was configured as a rigid-body transformation with six degrees of freedom. The BOLD time-series was then resampled onto subject-specific surface space in a non-gridded resampling performed using mri_vol2surf (FreeSurfer).

A set of physiological regressors were extracted to allow for component-based noise correction (CompCor; Behzadi et al., 2007). Principal components are estimated after high-pass filtering the preprocessed BOLD time-series (using a discrete cosine filter with 128 s cut-off) for the anatomical variant (aCompCor). Probabilistic masks of the CSF and WM were generated in anatomical space. The implementation differs from that of Behzadi et al. in that instead of eroding the masks by 2 pixels on BOLD space, the aCompCor masks were a mask of pixels that likely contain a volume fraction of GM. This mask is obtained by dilating a GM mask extracted from the FreeSurfer's aseg segmentation, and it ensures components are not extracted from voxels containing a minimal fraction of GM. Finally, these masks are resampled into BOLD space and binarized by thresholding at 0.99 (as in the original implementation). Components are also calculated separately within the WM and CSF masks.

All BOLD data underwent temporal high-pass filtering (Fourier GLM, cut-off: 3 cycles) and were denoised with 24 head-motion parameters (rigid-body, temporal derivative,

quadratic terms; Satterthwaite et al., 2013) and the first 5 aCompCor (WM + CSF) components (Behzadi et al., 2007).

4.2.4 Stimuli

Retinotopic mapping stimuli were constructed with a slowly moving aperture containing an 8 Hz contrast reversing checkerboard texture. Apertures and textures were generated at a resolution of 540×540 pixels and were constrained to the central 16° diameter circular region of the display. The display was uniform gray outside the aperture.

Aperture Design

The experiment consisted of twelve functional runs where two different types of stimulus apertures were presented (fixed-bar and log-bar, Figure 4.1). The stimulus completed 8 sweeps across the display within a run where each sweep started from a randomly chosen direction. Each run began with a 2 s blank period, this was followed by 8 sweeps each lasting 45 s and ended with a 4 s blank period. This resulted in a total duration of 366 s per run.

Three randomly seeded runs of the fixed-bar stimulus were generated and then transformed into the log-bar stimulus. Each session consisted of 3 runs of the fixed-bar stimulus and 3 runs of the log-bar stimulus.

Fixed-bar Stimuli

We created a variation of the drifting bar from Dumoulin and Wandell (2008), called the fixed-bar stimulus in this study. The fixed-bar stimulus was 2° in width and extended 16° within the apertured region of the display. The stimulus uniformly travelled at 0.4 $^\circ/s$ across the display from a randomly determined starting direction.

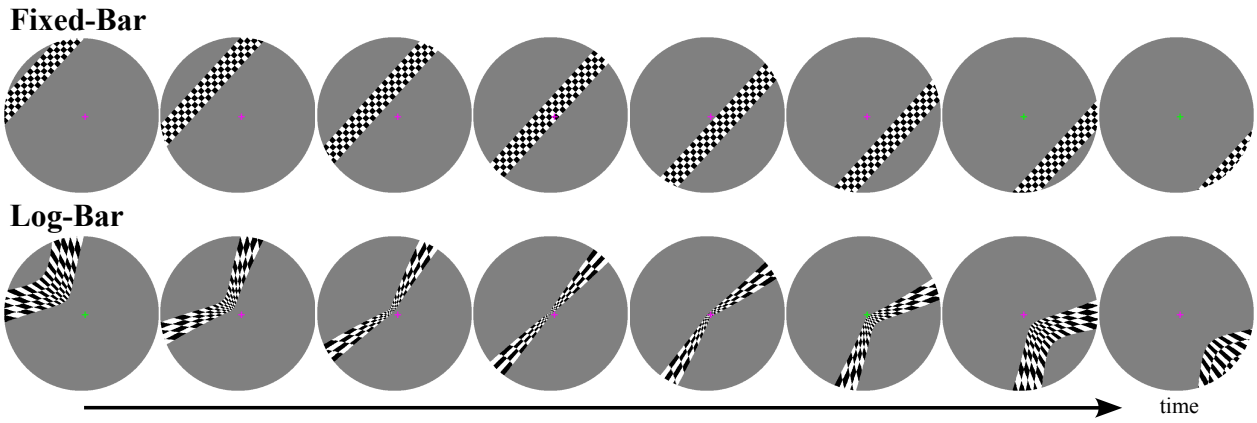

Figure 4.1: Frames from the fixed-bar and log-bar stimuli presented to subjects. The log-bar stimuli were produced by distorting the respective fixed-bar frame along the eccentricity axis as described in Equation 4.1. Subjects were instructed to fixate on the central cross and report with a button-press when the cross changed colors.

Log-bar stimuli

To create the logarithmically-distorted drifting bar (log-bar) stimuli, the fixed-bar stimulus was distorted along its eccentricity axis, expressed as

$$r_{log} = \ c \cdot \log\left(1 + k \cdot r_{fixed}\right) \tag{4.1}$$

where r_{log} is the eccentricity value of the log bar stimulus, c is a scalar to the distortion, k is the distortion factor, and r_{fixed} is the eccentricity value of the fixed bar stimulus. For this experiment, $k = 5$ and $c = \frac{r_{aperature} - \varepsilon}{\log(k \cdot r_{aperature})}$, where $r_{aperature} = 8$ was the maximum radial eccentricity of the display and $\varepsilon = 0.05$ was an adjustment factor to ensure the log-bar extended the full width of the aperture after distortion.

Experimental Design and Task

A small cross ("+") was presented at the center of the display and was present continuously throughout the experiment. The color of the cross switched from green to magenta on average 15 times per run, with a minimum switch delay of 3.2 s between each trial. Subjects were

instructed to maintain fixation on the cross and to press a response button whenever the color of the cross changed. The purpose of the task was to encourage fixation for the entire duration of the scan.

Stimuli were presented on a BOLDscreen32 LCD monitor (Cambridge Research Systems, Rochester, UK) monitor. The monitor operated at a resolution of 1920×1080 at 60 Hz with a viewing distance of 133 cm. An Intel i7 MacMini running MATLAB R2022a (MathWorks Inc., Natick, MA) controlled custom stimulus presentation code based on Psychtoolbox-3 (Brainard, 1997; Kleiner et al., 2007; Pelli, 1997). Behavioral responses were recorded using a button box (Current Designs, Haverford, PA, USA).

4.2.5 pRF Analysis

ROI selection

Initial visual cortex region selection for pRF fitting was performed by aligning each subjects' anatomical surface with Benson's atlas of visual cortex using the neuropythy software (Benson & Winawer, 2018). Afterwards, V1, V2, and V3 were extracted and dilated to ensure the ROIs encompassed the edges of each visual area. This process created an early visual cortex region of interest for each subject and hemisphere that was fed into the pRF fitting process.

Benson's atlas was used again after pRF fitting to fine-tune the visual area boundaries with the inclusion of subject's pRF information from all stimulus types and runs. Finally, a manual examination and editing was performed to create V1, V2, and V3 ROIs for each individual.

Additionally, an anatomical definition of the foveal confluence was drawn by dilating a seed placed at the occipital pole to be at least 350 mm^2 in surface area. This procedure defined the foveal confluence ROI for each individual as a contiguous, circular patch centered on the occipital pole.

Stimulus Preprocessing

Prior to model fitting, we preprocessed the stimulus movies. The stimulus movies were binarized for each stimulus frame, such that 0 s indicated the absence of the stimulus and 1 s indicated the presence of the stimulus at each pixel value. To reduce computational burden, each frame was downsampled from 540 $\times$ 540 pixels to 108 $\times$ 108-pixel resolution. Then, to match the temporal resolution of the fMRI data, the movies were downsampled to 366 frames. Model fitting was performed in units of degrees of visual angle.

Hemodynamic response function (HRF)

We modeled subjects' hemodynamic response function with SPM's gamma function (Friston et al., 1998). The HRF is characterized by 6 parameters expressed as

$$h\left(t\right) = \frac{\beta_1^{\alpha_1} t_*^{\alpha_1 - 1} \exp\left(-\beta_1 t_*\right)}{\Gamma\left(\alpha_1\right)} - \frac{\beta_2^{\alpha_2} t_*^{\alpha_2 - 1} \exp\left(-\beta_2 t_*\right)}{c\Gamma\left(\alpha_2\right)}, \quad t_* = t - \delta \tag{4.2}$$

where δ is the onset delay in seconds, α_1 is the time to peak response in seconds, α_2 is the time to undershoot response in seconds, β_1 is the response dispersion, β_2 is the undershoot dispersion, and c is the response-to-undershoot ratio. An HRF function was estimated for each subject and their hemispheres. This estimation resulted in 12 subjects $\times$ 2 hemispheres $=$ 24 sets of HRF parameters (Appendix A.2).

pRF Model

Each vertex was modeled as an isometric 2-D Gaussian with 3 parameters of interest. The model function was expressed as

$$G\left(x, y; \mu_x, \mu_y, \sigma\right) = \exp\left(-\left(\frac{\left(x - \mu_x\right)^2 + \left(y - \mu_y\right)^2}{2\sigma^2}\right)\right) \tag{4.3}$$

where μ_x and μ_y is the center of the 2-D Gaussian and σ is the standard deviation of the 2-D Gaussian. The parameters that represent the center of the 2-D gaussian, μ_x and μ_y, were

transformed from cartesian coordinates to polar coordinates, polar angle and eccentricity, after pRF estimation.

pRF Estimation

The pRF method states that the fMRI time series for each vertex is the linear sum of the stimulus time series and the vertex's pRF model convolved with the subject's HRF. For each vertex, the pRF model can be formally expressed as

$$\hat{r}(t) = S(x, y, t)\, G(x, y; \mu_x, \mu_y, \sigma) \circledast h(t) \tag{4.4}$$

where $\hat{r}(t)$ is the predicted fMRI time series, $S(x, y, t)$ is the stimulus movie, $G(x, y; \mu_x, \mu_y, \sigma)$ is a 2-D Gaussian, and $h(t)$ is the hemodynamic response function.

Using custom MATLAB software, pRF estimates for each vertex were determined to be the values that maximized the correlation between the predicted and actual fMRI time course. This can be formally stated as

$$\arg \max_{\mu_x, \mu_y, \sigma} corr\left(r(t), \hat{r}(t)\right) \tag{4.5}$$

where $r(t)$ is the actual fMRI time course and $\hat{r}(t)$ is the predicted time course (Equation 4.4). The pRF estimation yields four parameters of interest: pRF center location (μ_x, μ_y), pRF size (σ), and amount of variance in the fMRI time series that is explained by the pRF model prediction (R^2).

Model Fitting

We conducted pRF model fitting in two stages. First, a coarse parameter grid-search was performed with seeds for pRF centers (μ_x, μ_y) linearly sampled from $-8°$ to $8°$ in 20 steps. Seeds for pRF size (σ) were linearly spaced from 1 to 5 in 20 steps. The pRF size seeds were chosen to be larger than expected because Lage-Castellanos et al. (2020) reported steeper convergence gradients for pRF size when starting from larger values, irrespective of true pRF size. A predicted time course was generated for each seed and correlated with the actual

fMRI time course. The seed most correlated with the actual time course was chosen for the initial starting parameters for the next stage.

Second, we estimated each subject's HRF for each hemisphere by holding the pRF parameters from the grid-search fixed and fitting for the 6 HRF (δ, α_1, α_2, β_1, β_2, c) parameters. Next, we held the HRF parameters constant and fit the pRF parameters. This process was repeated for three iterations of HRF fitting to ensure parameters converge on a stable solution. To limit computation time, the HRF estimation process was carried out on 15% of the vertices that had variance explained that exceeded 20%. Median (across all vertices past threshold) HRF parameters were used to provide an estimate of that individual's HRF.

After subject HRFs were estimated, the final stage of pRF estimation was performed. The best starting seed parameters were calculated from the coarse grid-search procedure and then a nonlinear minimization routine (MATLAB's fminsearch) was conducted to find the final pRF estimates.

pRF estimates were fit separately for each stimulus type (fixed-bar and log-bar) and for each session or collapsed across sessions (i.e., session 1, session 2, or together). This procedure resulted in 12 subjects $\times$ 2 hemispheres $\times$ 2 stimulus types $\times$ 3 session configurations = 144 sets of pRF estimates.

After pRF fitting, the Cartesian coordinates of the pRF center (μ_x, μ_y) were transformed into polar coordinates (polar angle and eccentricity). Only vertices with estimated pRF centers that were less than 8° eccentricity (i.e., within the display), had a pRF size greater than 0.05° , and exceeded 10% of the variance explained model were retained for subsequent analyses.

4.2.6 pRF Size and Cortical Magnification Factor

pRF size estimates were obtained from the pRF model fitting procedure described above. CMF was calculated for each vertex by dividing the local cortical distance by the local change in pRF location (Clavagnier et al., 2015; Harvey & Dumoulin, 2011). At each vertex along a subject's reconstructed surface, local cortical distance (in mm) was calculated as the

mean geodesic distance of neighbor vertices from the current vertex. Local pRF location distance (in degrees) was calculated as the average distance of estimated pRF location of the neighboring vertices from the current vertex. Only pRFs with fits that exceeded 10% variance explained were included in the calculation.

We also define the relationship between pRF size, CMF, and eccentricity following the procedures in Harvey and Dumoulin (2011). In brief, the relationship between pRF size and eccentricity can be fit with the following equation:

$$y = ax + b \tag{4.6}$$

where y is pRF size, x is eccentricity, a is the slope, and b is the intercept. The relationship between CMF and eccentricity can be fit with the following equation:

$$y = \frac{1}{cx + d} \tag{4.7}$$

where y is CMF, x is eccentricity, c is the shape of the decay, and d is the eccentricity shift. The population point image (pPI) was defined as the pRF size multiplied with the CMF. This can be formally expressed as the product of Equation 4.6 and 4.7 to be:

$$y = \frac{ax + b}{cx + d} \tag{4.8}$$

where y is the population point image and x is eccentricity.

To compute the parameters for 4.6 and 4.7, eccentricity was discretized into 50 linearly spaced bins from 0° to 8° and corresponding pRF sizes and CMF were averaged within each eccentricity bin. Subject data was fit by minimizing the sum of squared error weighted by the inverse of the standard error of the mean for each eccentricity bin.

4.2.7 pRF Model Simulations

To establish a ground-truth comparison for fixed-bar and log-bar stimulus performance, we generated simulated pRFs based on Equation 4.4.

First, we defined a unique set of 4800 pRF locations by sampling polar angle coordinates from 0° to 345° directions in 15° steps and logarithmically sampling from 0.01° to 8° eccentricity in 200 steps. pRF size was determined by a linear relationship between a pRF's eccentricity value and pRF size. The formal definition is as follows: size $= 0.15r + 0.1$, based on Himmelberg et al. (2021).

fMRI time courses were then generated for each simulated pRF and for each stimulus aperture type. Lastly, Gaussian noise was added to the simulated time courses to match average variance explained of the collected fMRI dataset. The simulated time course was then passed to the pRF fitting procedure and pRFs parameters were estimated for each stimulus aperture separately. This process of fitting the simulated pRFs was repeated 12 times for each stimulus aperture. After the pRFs were estimated, the same thresholds from the human data were also applied to the simulated pRF estimates.

4.2.8 Behavioral Analysis

The subjects' responses to the color detection task were examined across 12 functional runs. Performance was defined as

$$\text{Performance} = \frac{n_{hit} - n_{miss}}{n_{total}} \cdot 100 \tag{4.9}$$

where n_{hit} is the number of successful color change detections (defined as a button press within 1 s of a color change), n_{miss} indicates the number of additional responses without a color change, and n_{total} indicates the total number of color changes. Average behavioral performance was 96.39% and the interquartile range (central 50%) of performance values across subjects was $[95.28\%, 98.89\%]$.

4.3 Results

4.3.1 pRF Cortical Maps

We obtained pRF parameter estimates of polar angle, eccentricity, pRF size, and variance explained for all subjects. Figure 4.2 shows example pRF parameter maps for the cortical surface of a single subject, separately for each stimulus type.

4.3.2 pRF Estimate Reliability

We assessed the reliability of pRF estimates derived from each stimulus type to compare model performance under different stimulation conditions. The data were split by stimulus type and session, producing 4 sets of pRF estimates for each subject (2 stimulus types $\times$ 2 sessions) .

We quantified pRF estimate intersession reliability according to the procedures outlined in van Dijk et al. (2016). In summary, the Spearman's rank correlation coefficient was calculated between pRF parameter estimates from session 1 and session 2 of the same stimulus type vertex-by-vertex for eccentricity and pRF size. As polar angle is a circular statistic, we used the circular correlation coefficient (Jammalamadaka & Sengupta, 2001, p. 176) to compute reliability for polar angles estimates. Correlation coefficients were transformed into Fisher's z-scores (Fisher, 1915) to convert the non-normal correlation sampling distribution into a standardized statistic.

Figure 4.3 and 4.4 shows the point density plots comparing the pRF estimate reliability of all parameters (polar angle, eccentricity, and pRF size) for the fixed-bar and log-bar stimuli within the foveal confluence, V1, V2, and V3.

We ran a mixed-effects ANOVA on the intersession reliability for each pRF parameter (polar angle, eccentricity, and pRF size) as dependent variables, treating subject as a random-effects variable, and hemisphere, stimulus aperture, and ROI as fixed-effect variables (see Appendix B.1 for full results).

Figure 4.5 and Table 4.1 report the average intersession reliability for polar angle, eccen-

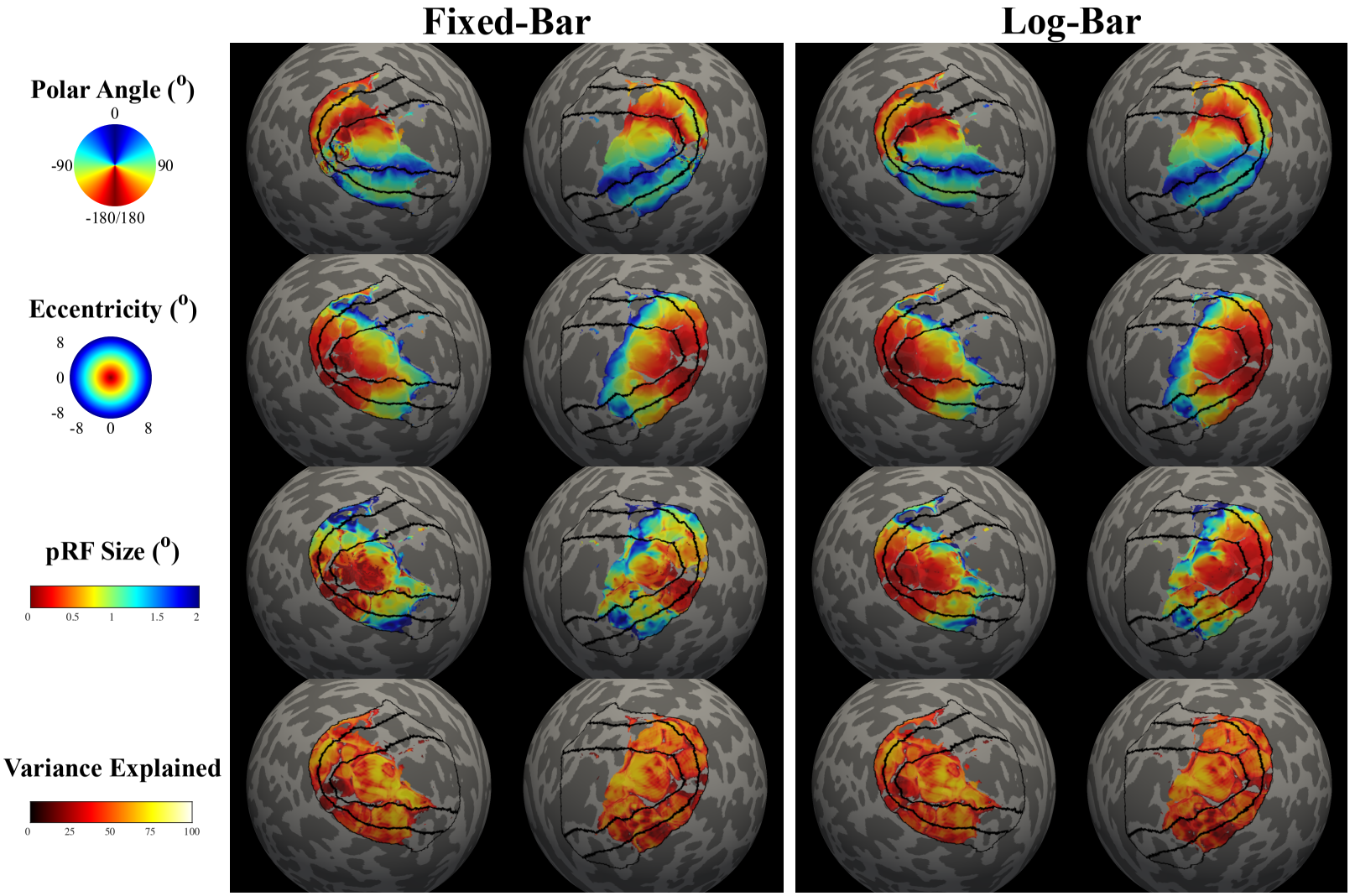

Figure 4.2: Retinotopic maps of pRF parameters across stimulus types from an example subject. pRF parameters maps overlaid on an example subject's cortical surface warped into a sphere. The columns represent the session average (6 runs) using the fixed-bar and log-bar stimuli. The black lines delineate V1, V2, and V3. All values are thresholds to 10% variance explained.

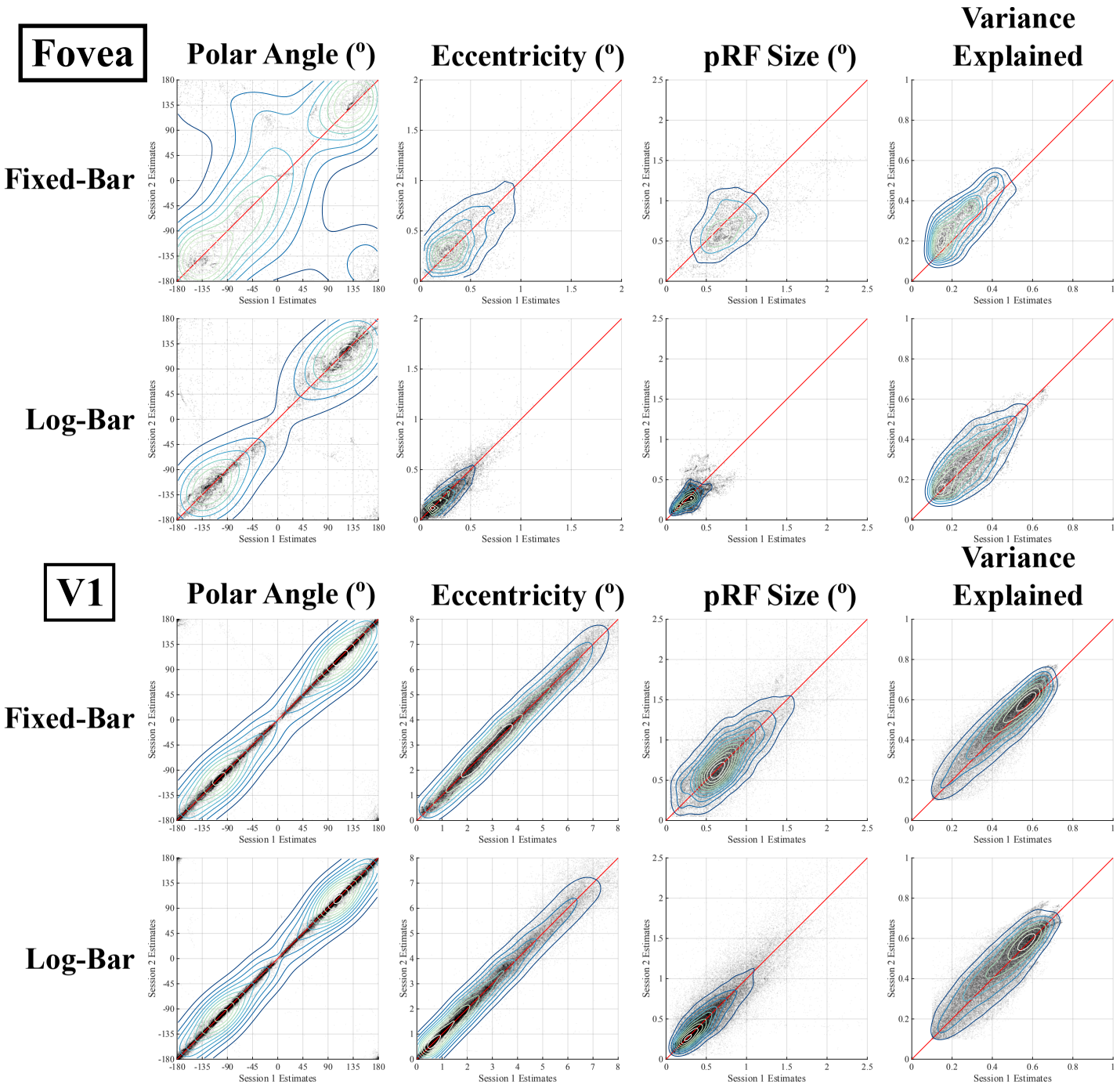

Figure 4.3: Point density plots of pRF estimate intersession reliability in the foveal confluence and V1. Data from all subjects collapsed over hemisphere is shown. Isodensity lines (green/blue) and the identity line (red) are drawn.

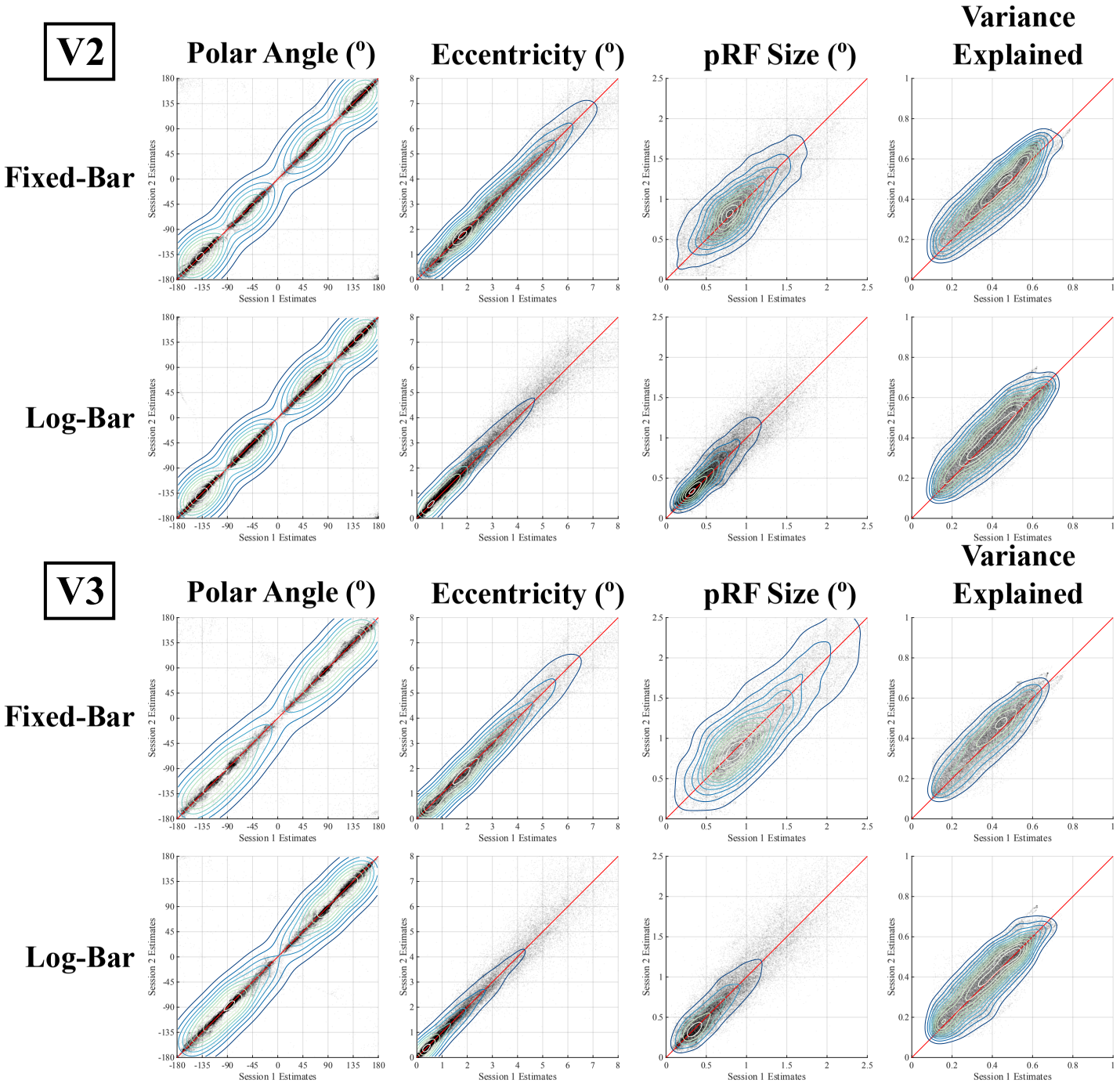

Figure 4.4: Point density plots of pRF estimate intersession reliability in V2 and V3. Same configurations as Figure 4.3.

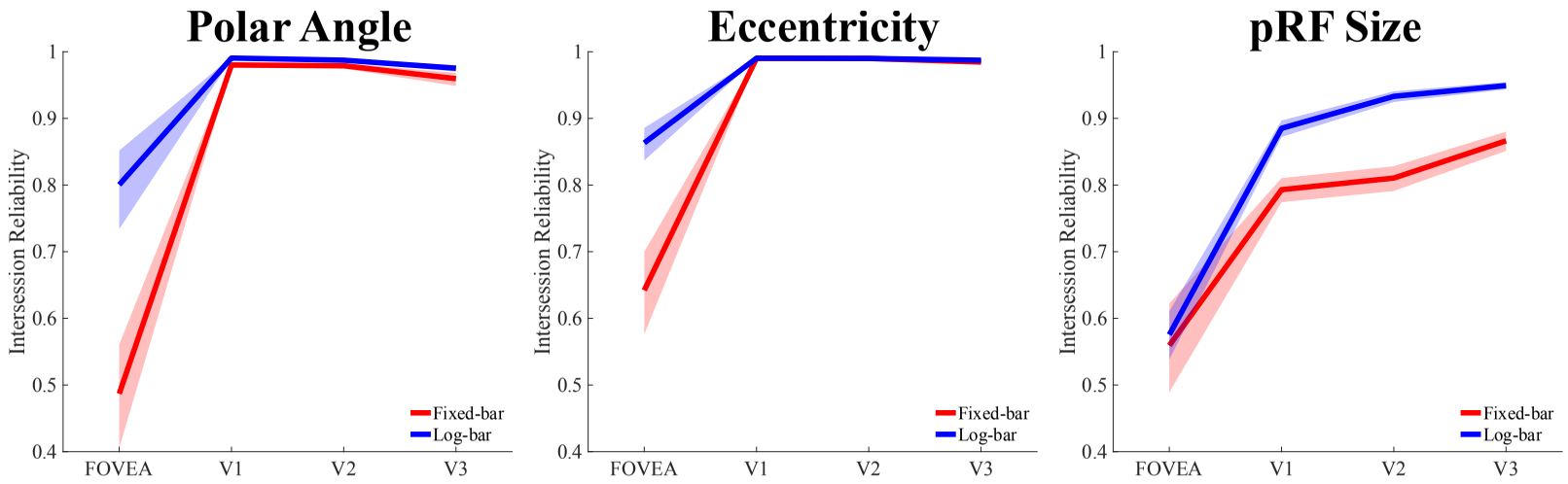

Figure 4.5: Intersession reliability for pRF parameter estimates of polar angle, eccentricity, and pRF size across visual areas. Solid lines (red = fixed-bar, blue = log-bar) represent the intersession correlation coefficient average over subjects and filled regions represent ±1 standard error of the mean.

	Fovea		**V1**		**V2**		**V3**	
	fixed-bar	log-bar	fixed-bar	log-bar	fixed-bar	log-bar	fixed-bar	log-bar
Polar Angle	0.49 (0.10)	0.80 (0.16)	0.98 (0.09)	0.99 (0.09)	0.98 (0.10)	0.99 (0.11)	0.96 (0.12)	0.98 (0.09)
Eccentricity	0.64 (0.10)	0.86 (0.10)	0.99 (0.06)	0.99 (0.04)	0.99 (0.05)	0.99 (0.04)	0.98 (0.06)	0.99 (0.05)
pRF Size	0.56 (0.10)	0.58 (0.05)	0.79 (0.05)	0.89 (0.06)	0.81 (0.05)	0.93 (0.06)	0.87 (0.06)	0.95 (0.06)

Table 4.1: Summary of intersession reliability of pRF estimates of polar angle, eccentricity, and pRF size across visual areas. Values are formatted as M (SEM).

tricity, pRF size for the fixed-bar and log-bar stimulus across all ROIs.

There was a main effect of stimulus type on polar angle ($F(1, 165) = 32.0187$, $p < 0.0001$), eccentricity ($F(1, 165) = 15.0649$, $p = 0.0001$), and pRF size ($F(1, 165) = 106.2833$, $p < 0.0001$). A Tukey-Kramer analysis showed that polar angle, eccentricity, and pRF size estimates were more reliable for the log-bar than the fixed-bar stimulus.

There was a main effect of ROI on polar angle ($F(1, 165) = 146.2925$, $p < 0.0001$), eccentricity ($F(1, 165) = 345.5603$, $p < 0.0001$), and pRF size ($F(1, 165) = 141.2880$, $p < 0.0001$) estimate reliability. A Tukey-Kramer analysis revealed that the foveal confluence ROI was consistently the least reliable for all parameters, relative to V1, V2, and V3.

There was an interaction effect of stimulus type and ROI for eccentricity ($F(3, 165) = 9.3316, p < 0.0001$) and pRF size ($F(3, 165) = 0.6909$, $p < 0.0001$) intersession reliability. For eccentricity estimates, a Tukey-Kramer analysis showed that eccentricity intersession reliability within the foveal confluence derived from the fixed-bar stimulus were the least reliable combination as compared with all other stimulus and ROI combinations. For pRF size estimates, a Tukey-Kramer analysis showed that pRF size was more reliable for the log-bar than fixed-bar stimulus for all ROIs except the foveal confluence.

The fixed-bar and log-bar intersession reliability were excellent for pRF estimates of polar angle and eccentricity in V1, V2, and V3. pRF size reliability was better for the log-bar stimulus than the fixed-bar stimulus in V1, V2, and V3. In the foveal confluence, the log-bar stimulus had better intersession reliability for polar angle and eccentricity estimates, but similar reliability as the fixed-bar stimulus for pRF size.

4.3.3 Frequency of Estimated pRFs

We compared the number of estimated pRFs that passed threshold. We performed a mixed-effects ANOVA with the number of estimated vertices as the dependent variable, treating subject as a random-effects variable, and hemisphere, stimulus type, and ROI as fixed-effects variables. Only significant results are reported in-text (see Appendix B.2 for full results).

There was a main effect of stimulus type on number of estimated pRFs, $F(1, 165) = 53.31$,

$p < 0.0001$. A Tukey-Kramer analysis revealed that the fixed-bar stimulus estimated fewer pRFs than the log-bar stimulus. There was a main effect of ROI on number of estimated pRFs, $F(3, 165) = 541.63$, $p < 0.0001$. A Tukey-Kramer analysis revealed that V1, V2, V3, and the foveal confluence had the most to least number of estimated pRFs.

On average across all comparison conditions, 434.75 ($SD = 212.8711$) vertices were successfully estimated only by the log-bar stimulus. Of these vertices, the estimated eccentricity ($M = 1.5420$, $SD = 1.0391$) and pRF size ($M = 0.4991$, $SD = 0.2961$) indicated that these vertices were ones responsible for central vision.

4.3.4 Effect of Stimulus Type on pRF Parameter Estimates

We examined the changes in pRF parameter estimates due to stimulus type. The pRF parameters were estimated separately for each stimulus aperture, collapsing across session, to produce 2 sets of pRF estimates for each subject in this analysis.

For each parameter (polar angle, eccentricity, pRF size, and variance explained), we performed a mixed-effects ANOVA with the difference between the parameter estimates (fixed-bar − log-bar) as the dependent variable and treating subject as a random-effects variable and hemisphere and ROI as fixed-effects variables. Only significant results are reported in-text (see Appendix B.3 for full results).

Polar Angle

There were no significant effects of any condition on polar angle estimate differences (Figure 4.6).

Eccentricity

There was a significant main effect of hemisphere ($F(1, 77) = 8.0386$, $p = 0.0058$) and ROI ($F(3, 77) = 30.3408$, $p < 0.0001$) on eccentricity estimate differences (Figure 4.7). Bonferrroni-corrected post-hoc paired t-tests ($\alpha' = \frac{0.01}{6} = 0.0017$) revealed that eccentricity

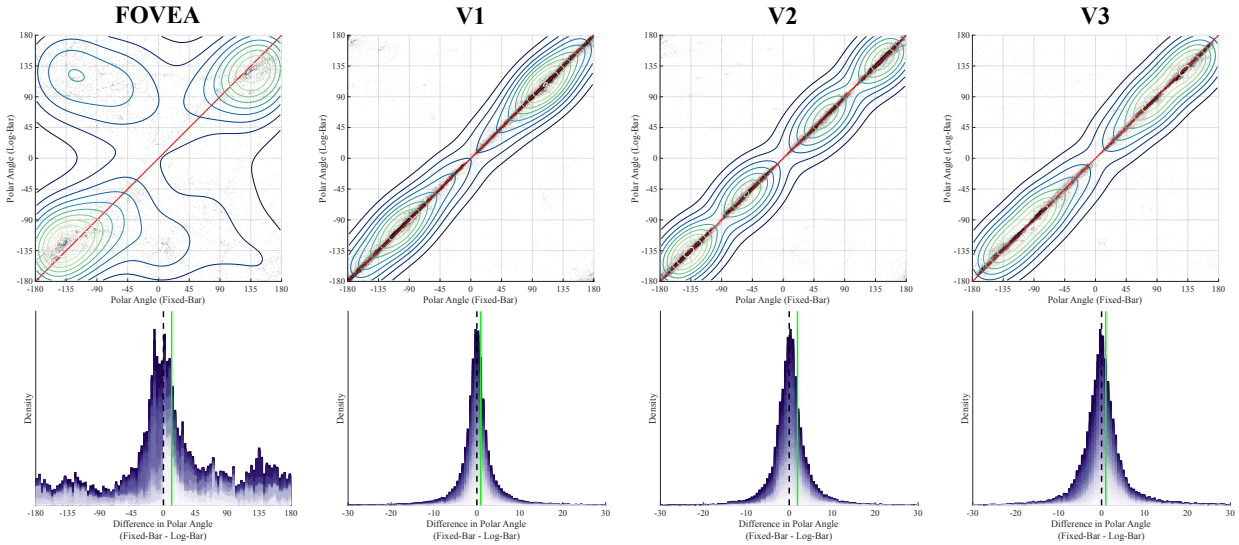

Figure 4.6: Difference in pRF polar angle estimates across visual areas. (Top row) Isodensity curves between the fixed-bar and log-bar polar angle estimates. (Bottom row) Histogram of differences between fixed-bar to log-bar polar angle estimates. Difference values were computed as fixed-bar minus log-bar values. The dashed black line indicates zero difference, the red line indicates the mean difference, and colors represent individual hemispheres.

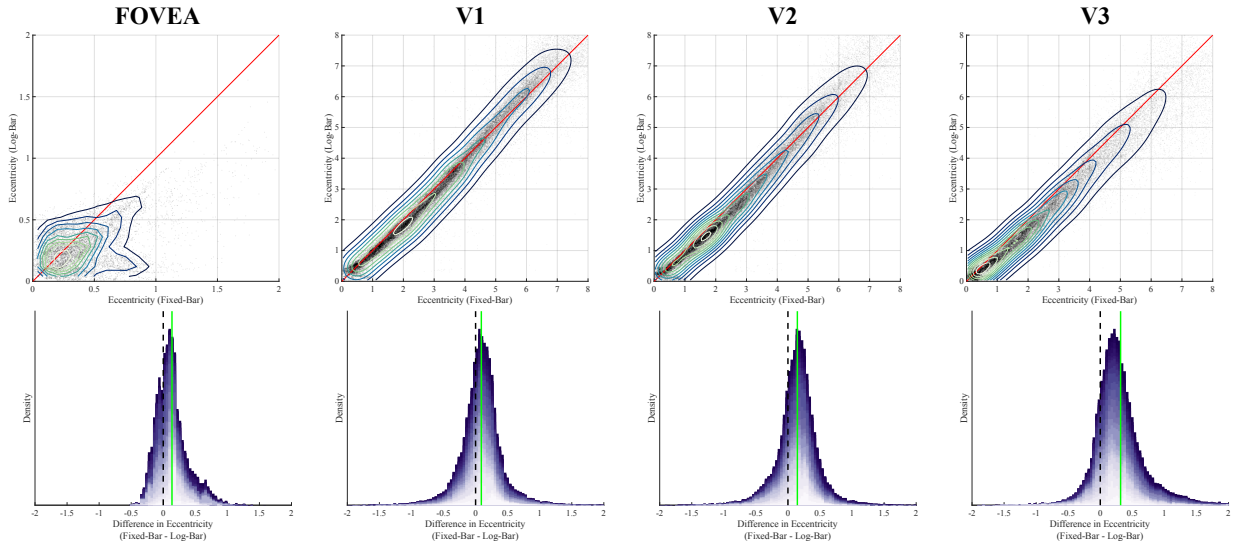

Figure 4.7: Difference in pRF eccentricity estimates across visual areas. Same configuration as Figure 4.6.

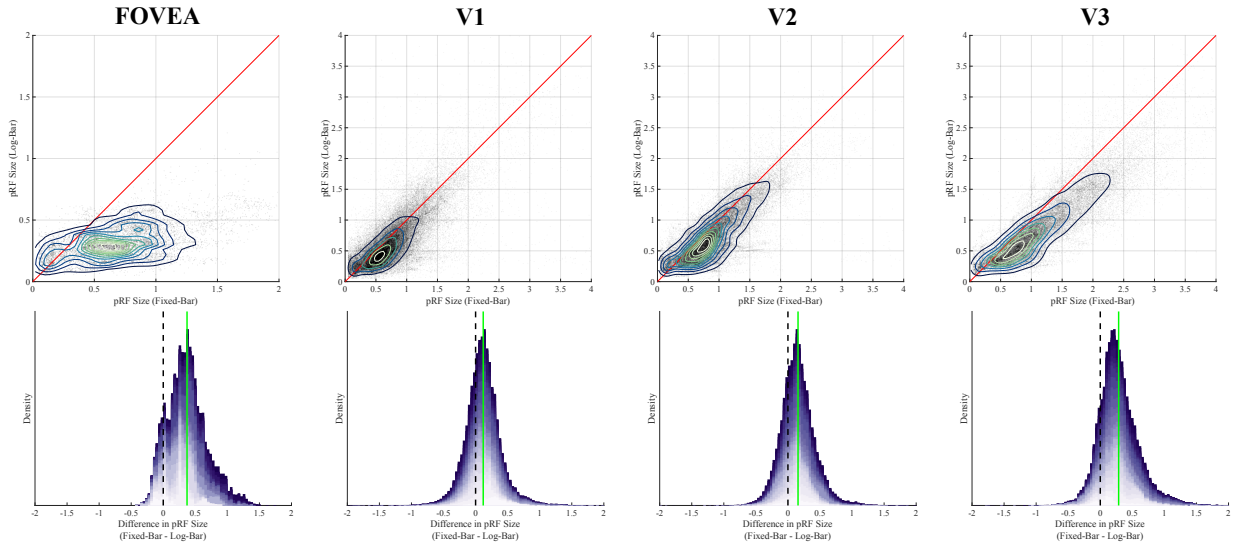

Figure 4.8: Difference in pRF size estimates across visual areas. Same configuration as Figure 4.6.

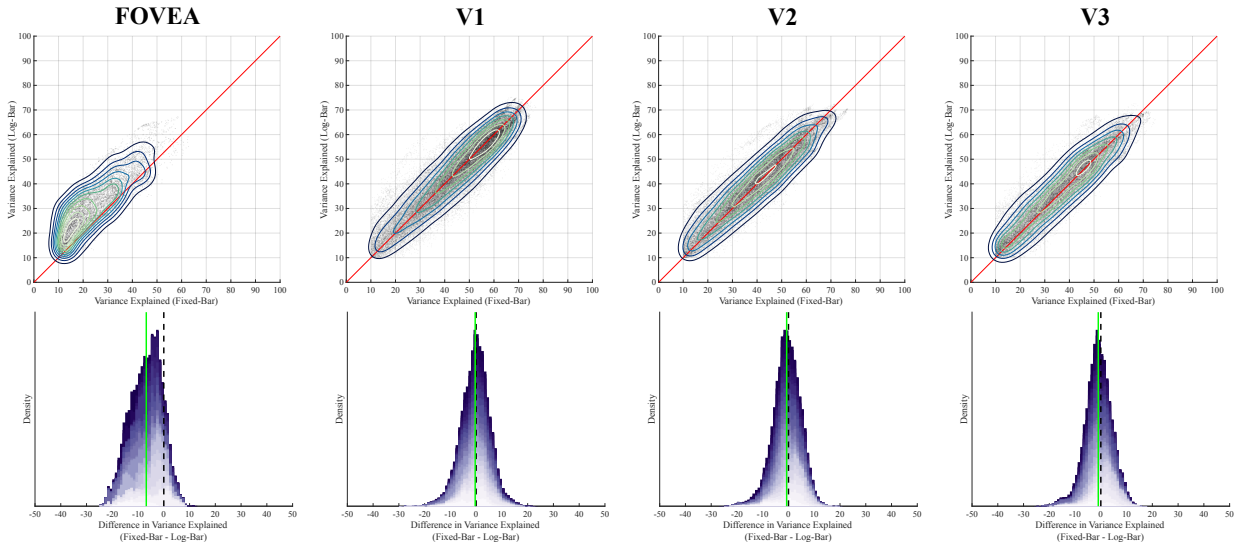

Figure 4.9: Difference in variance explained across visual areas. Same configuration of Figure 4.6.

values in the left ($t(47) = 8.2987$, $p < 0.0001$) and right ($t(47) = 8.5955$, $p < 0.0001$) hemispheres were significantly larger when estimated from the fixed-bar stimulus than the log-bar stimulus. Similarly, eccentricity values were significantly larger for the fixed-bar stimulus than the log-bar stimulus in the foveal confluence ($t(23) = 6.0663$, $p < 0.0001$), V2 ($t(23) = 6.7668$, $p < 0.0001$), and V3 ($t(23) = 12.1683$, $p < 0.0001$). Eccentricity was marginally larger for the fixed-bar stimulus versus the log-bar stimulus in V1, $t(23) = 3.5048$, $p = 0.0019$.

pRF Size

There was a significant main effect of hemisphere ($F\,(1, 77) = 7.0569$, $p = 0.0096$) where pRF size differences were smaller in the left hemisphere than the right hemisphere. There was a significant main effect of ROI ($F(3, 77) = 23.3607$, $p < 0.0001$) on the differences in pRF size estimates (Figure 4.8). Bonferrroni-corrected post-hoc paired t-tests ($\alpha^{'} = \frac{0.01}{6} = 0.0017$) revealed that pRF size estimates were also significantly larger for the fixed-bar stimulus than the log-bar stimulus in the foveal confluence ($t(23) = 8.7417$, $p < 0.0001$), V1 ($t(23) = 6.4849$, $p < 0.0001$), V2 ($t(23) = 8.0437$, $p < 0.0001$), and V3 ($t(23) = 11.8887$, $p < 0.0001$).

Additionally, there was a significant interaction effect of hemisphere and ROI ($F\,(3, 77) = 4.4849$, $p = 0.0059$). A post-hoc Tukey-Kramer analysis revealed that pRF size estimate differences in the foveal confluence from both hemispheres, but especially the right hemisphere, were significantly larger than all other hemisphere and ROI combinations.

Variance Explained

There was a significant main effect of ROI ($F(3, 77) = 50.19$, $p < 0.0001$) on difference on variance explained (Figure 4.9). Bonferrroni-corrected post-hoc paired t-tests for each ROI ($\alpha^{'} = \frac{0.01}{4} = 0.0025$) revealed that variance explained was significantly larger when using the log-bar stimuli within the foveal confluence, $t(23) = -7.2173$, $p < 0.0001$.

In summary, the fixed-bar stimulus produced pRF estimates that were larger and more peripheral that the pRF parameters estimated with the log-bar stimulus. Model variance

explained were similar across stimulus types, but favored the foveal confluence, which had greater variance explained for the log-bar stimulus.

4.3.5 pRF Size, Cortical Magnification Factor, and Eccentricity

We examined pRF size, CMF, and pPI as a function of eccentricity across stimulus types and visual areas (Figure 4.10). For each equation parameter from Equation 4.6 (a, b) and Equation 4.7 (c, d), we performed a mixed-effects ANOVA with the parameter as the dependent variable and treating subject as a random-effects variable and hemisphere, stimulus type, and ROIs as fixed-effects variables. Only significant results are reported in-text (see Appendix B.4 and B.5 for full results) and a summary of the equation parameters are reported in Table 4.2.

There was a main effect of ROI on the slope (a) between pRF size and eccentricity, $F(1, 165) = 8.4201$, $p < 0.0001$. The slope increased from V1 to V2 to V3 and the fovea has the second steepest slope value. There was a main effect of stimulus type ($F(1, 165) = 152.5007$, $p < 0.0001$), and ROI ($F(3, 165) = 7.0913$, $p = 0.0002$) on the intercept (b) of pRF size by eccentricity. The intercept parameter was smaller for the log-bar stimulus than the fixed-bar stimulus. The smallest intercept values were from V1 and V2, followed by V3, and then the fovea. There was an interaction effect of hemisphere and ROI on intercept values ($F(3, 165) = 3.9090$, $p = 0.0099$). A simple effects analysis by ROI was conducted to examine the interaction effect. The interaction effect was driven by the fovea where the left hemisphere intercepts were significantly larger than the right hemisphere, $F(1, 165) = 17.4167$, $p < 0.0001$. The differences in the individual pRF size equation parameters were reflected in the differences in pRF size at 1° (see Appendix B.5).

There was a significant main effect of ROI on the CMF slope parameter (c), $F(3, 165) = 21.8163$, $p < 0.0001$. The estimated CMF slope parameter increased from in order from V1, V2, V3, to the foveal confluence. There was a main effect of stimulus type ($F(1, 165) = 171.2824$, $p < 0.0001$) and ROI ($F(3, 165) = 12.8569$, $p < 0.0001$) on the CMF intercept parameter (d). Intercept values were smaller for log-bar stimulus than the fixed-bar stim-

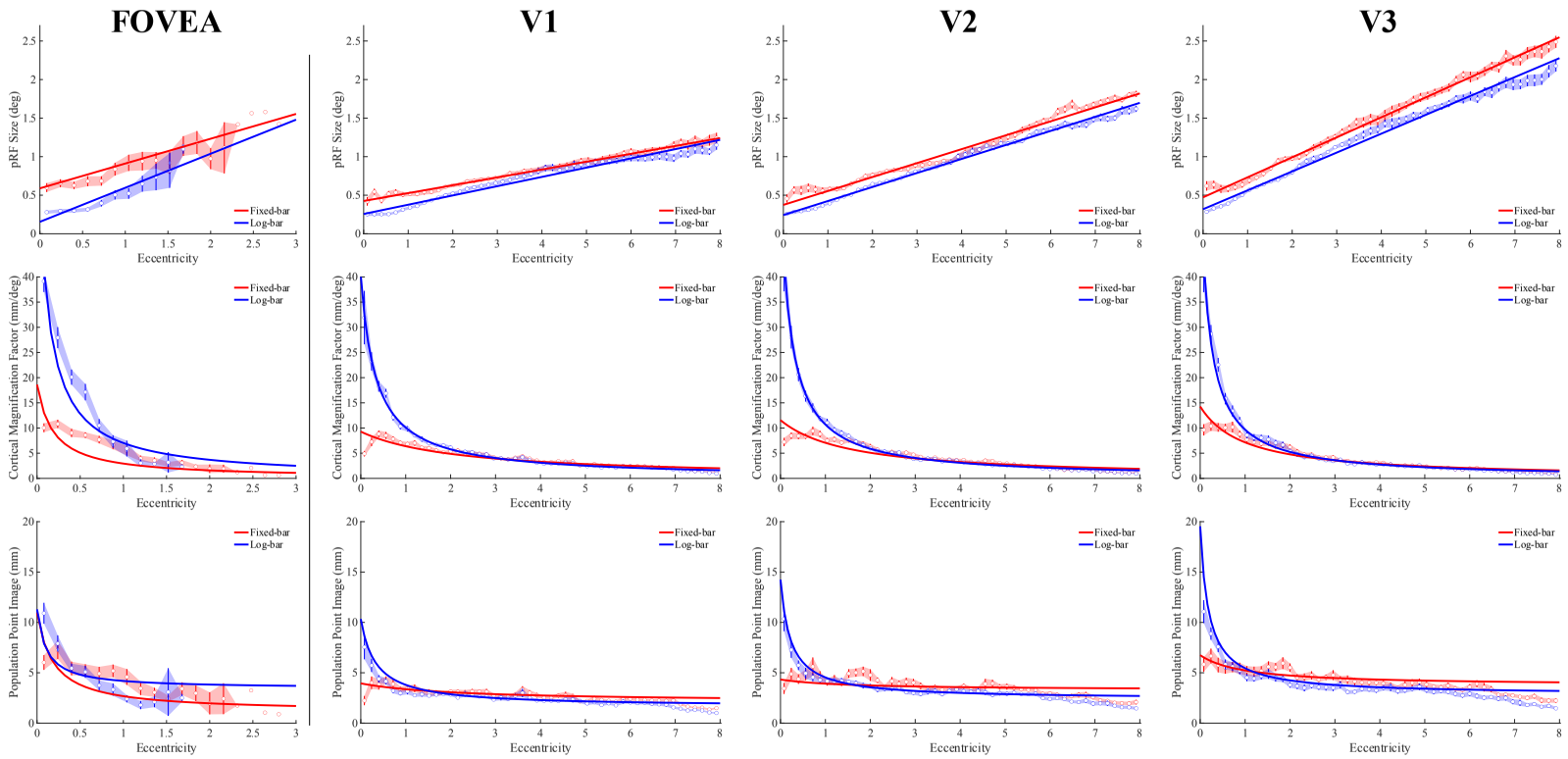

Figure 4.10: pRF size, cortical magnification factor, and population point image as a function of eccentricity across visual areas. The top row depicts average pRF size, middle row depicts cortical magnification factor, and the bottom row depicts the population point image across eccentricity. Red represents the fixed-bar stimulus and blue represents the log-bar stimulus. The dots represent the average within an eccentricity bin, the shaded regions represent the standard error of the mean. Solid lines represent the 4.6, 4.7 and 4.8 fit to the averaged data and are only for illustrative purposes.

	Fovea		V1		V2		V3	
	fixed-bar	log-bar	fixed-bar	log-bar	fixed-bar	log-bar	fixed-bar	log-bar
pRF (Eq. 4.6)								
$a(^\circ/^\circ)$	0.31 (0.34)	0.17 (0.25)	0.10 (0.05)	0.12 (0.04)	0.17 (0.03)	0.19 (0.03)	0.26 (0.06)	0.25 (0.03)
b $(^\circ)$	0.54 (0.29)	0.25 (0.10)	0.41 (0.15)	0.22 (0.09)	0.39 (0.14)	0.21 (0.09)	0.47 (0.17)	0.28 (0.09)
pRF size at 1° $(^\circ)$	0.85 (0.36)	0.42 (0.24)	0.51 (0.11)	0.34 (0.07)	0.56 (0.1187)	0.40 (0.06)	0.72 (0.13)	0.53 (0.08)
CMF (Eq. 4.7)								
c (mm^{-1})	0.16 (0.15)	0.14 (0.09)	0.05 (0.01)	0.08 (0.02)	0.06 (0.01)	0.08 (0.01)	0.07 (0.02)	0.10 (0.01)
d $(^\circ/\text{mm})$	0.08 (0.06)	0.01 (0.01)	0.14 (0.06)	0.03 (0.01)	0.10 (0.02)	0.03 (0.03)	0.10 (0.06)	0.02 (0.01)
CMF at 1° $(\text{mm}/^\circ)$	5.40 (3.51)	7.90 (3.67)	5.73 (1.18)	9.36 (0.98)	6.57 (0.92)	9.71 (1.55)	6.17 (1.17)	8.63 (0.82)

Table 4.2: Summary of pRF size and CMF by eccentricity equation parameters and pRF size and CMF at 1° eccentricity. Reported parameter means and standard deviation in parenthesis.

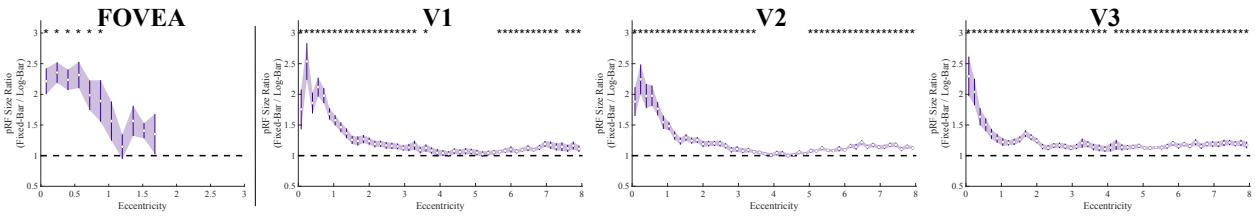

Figure 4.11: pRF size ratio as a function of eccentricity across visual areas. The graphs show the ratio (fixed-bar over log-bar) of pRF sizes where positive values represent larger pRF sizes from the fixed-bar stimulus and negative values represent larger values for the log-bar stimulus. Asterisks (*) represent bins that were significantly different from 1. Solid lines represent the average across subjects and the shaded area represents the ±1 standard error of the mean.

ulus. Intercept values were decreased from V1, V2, V3, to the foveal confluence. There were significant main effects of stimulus type ($F(1, 165) = 112.5906$, $p < 0.0001$) and ROI ($F(3, 165) = 4.8850$, $p = 0.0028$) on CMF at 1° eccentricity. The predicted CMF at 1o was smaller for the fixed-bar stimulus than the log-bar stimulus. The predicted CMF at 1o also increased from the foveal confluence, V3, V1, to V2.

We found that the pPI was slightly decreased as eccentricity increased within the range of 0° to 8° and the rate of change was similar for both stimulus configurations. The largest difference occurs from 0° to 1° where the log-bar pPI rapidly decreases whereas the fixed-bar pPI stays flat.

4.3.6 pRF Size Comparison as a Function of Eccentricity

We computed the ratio of pRF sizes by normalizing the fixed-bar pRF sizes by log-bar pRF sizes across eccentricity.

We performed one-sample t-tests on each eccentricity bin on the pRF size ratio values to compare if pRF sizes were significantly different depending on the stimulus type (Figure 4.11). Within the foveal confluence, pRF sizes were significantly larger under the fixed-bar stimulus than the log-bar stimulus for pRFs from 0° to 1° . Likewise, pRF sizes exhibited the largest different in pRF size estimates from 0° to 2° within V1, V2, and V3. On average

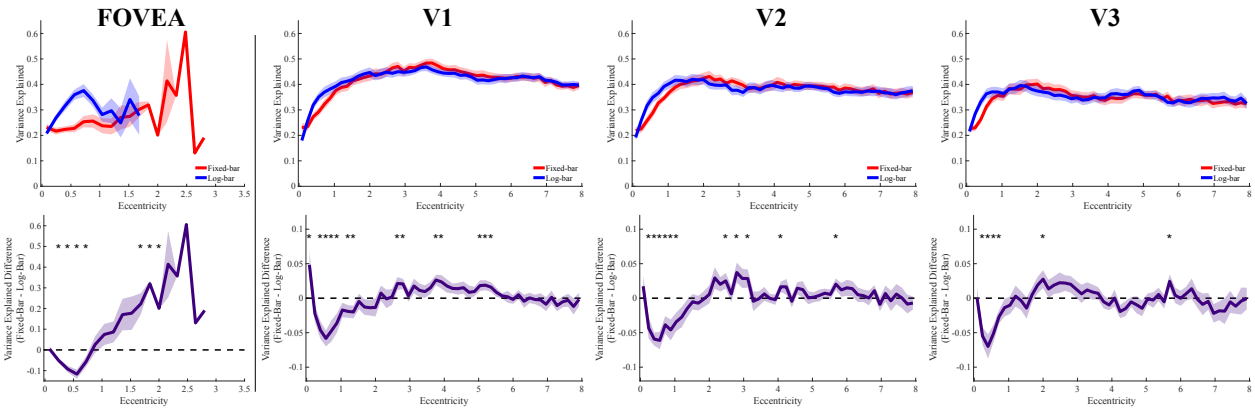

Figure 4.12: Variance explained as a function of eccentricity across visual areas. (Top) depicts average variance explained across eccentricity separated by stimulus type (red = fixed-bar, blue = log-bar). (Bottom) Difference between the fixed-bar and log-bar variance explained where positive values mean larger variance explained values for the fixed-bar stimulus and negative values represent larger values for the log-bar stimulus. Asterisks (*) represent bins that were significantly different than 0. Solid lines represent the average across subjects and the shaded area represents the ± 1 standard error of the mean.

across visual areas, pRF size estimates were 1.6× larger for the fixed-bar than the log-bar stimulus within this eccentricity range.

4.3.7 Variance Explained as a Function of Eccentricity

We examined variance explained as a function of eccentricity across all visual areas to examine if goodness-of-fit could explain the difference in pRF size estimates. For each stimulus type and ROI, the average variance explained was binned by eccentricity as described previously. Afterwards, the difference in variance explained was calculated by subtracting log-bar from fixed-bar values (Figure 4.12).

Paired t-tests were then conducted on the difference in variance explained for each eccentricity bin. Across all visual areas, there was a significant difference in variance explained from 0° to 1° eccentricity, such that variance explained was larger for log-bar stimuli than fixed-bar stimuli. Variance explained was not significantly different between the fixed-bar

and log-bar for eccentricities $> 1°$.

4.3.8 pRF Simulations

We estimated pRFs from simulated fMRI time courses to compare the effects of stimulus types on pRF estimates when there is a known ground truth. Our simulations qualitatively replicated the difference in fixed-bar versus log-bar estimates from our collected dataset (Figure 4.13).

The simulated pRF results displayed larger estimates of pRF size for the fixed-bar stimulus than the log-bar stimulus for pRFs that were located $< 2°$ eccentricity. When we compared the ratio of simulated pRF sizes to the ground truth for pRFs, the results also mimicked the actual human data. Simulated pRF sizes from the fixed-bar stimulus were estimated to be approximately $3\times$ larger than the ground truth for pRFs located from $0°$ to $2°$ eccentricity. In comparison, log-bar simulated pRF sizes qualitatively matched ground truth more closely.

We then took a closer look at the ratio of simulated pRF size to ground truth for pRFs that were located from $0°$ to $2°$ eccentricity across stimulus types (Figure 4.13C, D). The fixed-bar ratio values were positively skewed and displayed a larger standard deviation of values than the log-bar stimulus. The log-bar ratio values displayed a tight normal distribution around the ground truth pRF size. This observation suggests that for smaller pRFs, the fixed-bar stimulus produced more variable and biased estimates of pRF size than the log-bar stimulus.

It is noteworthy that although the fixed-bar simulated pRFs were able to estimate smaller eccentricity values than the log-bar stimulus, the corresponding fixed-bar pRF size estimates were more biased towards larger pRF sizes at the smaller eccentricities than the log-bar stimulus. The log-bar simulated pRFs at the same smaller eccentricities were removed from the analysis due to lower variance explained.

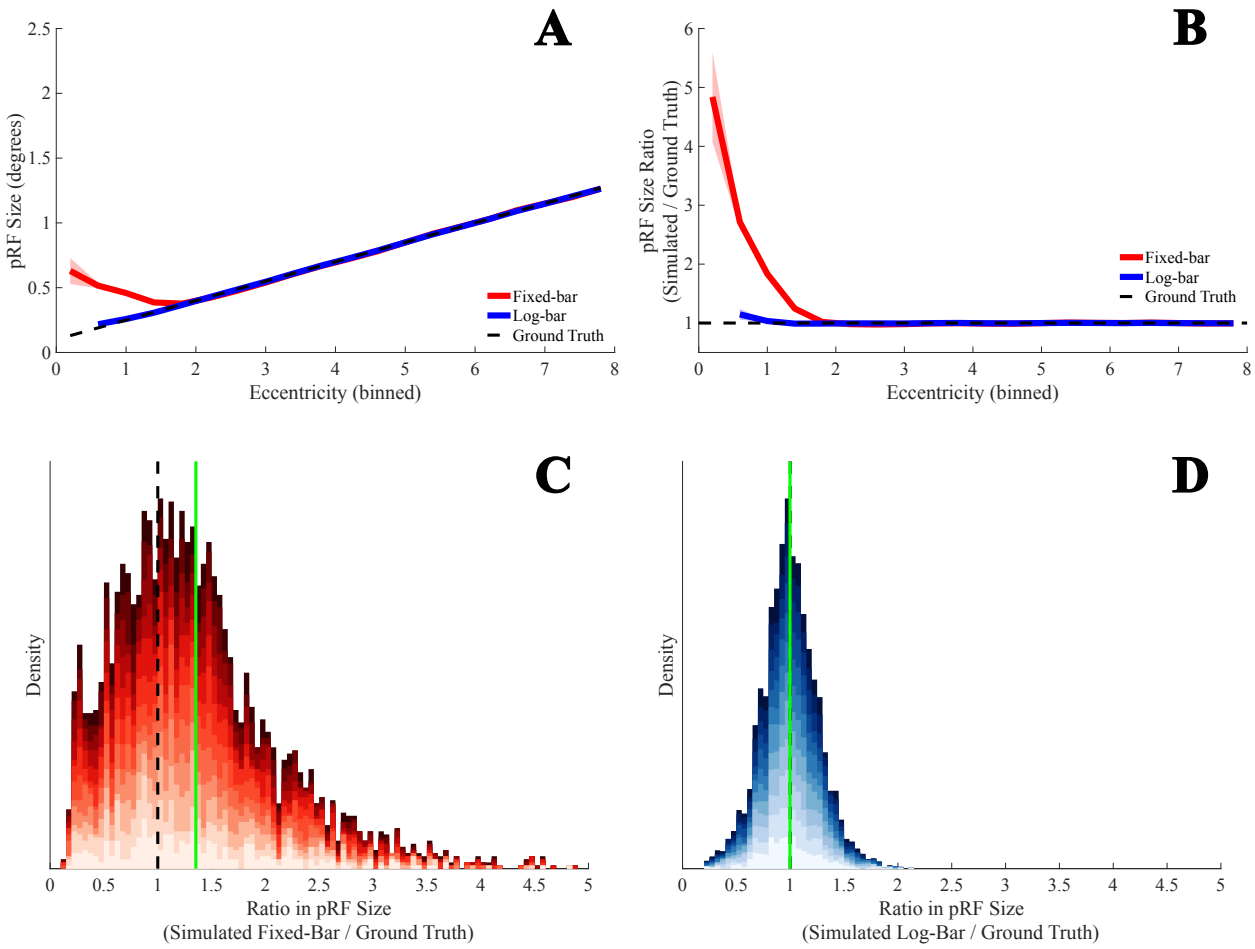

Figure 4.13: Simulated pRF size estimate comparisons to ground truth. (A) Simulated pRF size as a function of eccentricity. (B) pRF size ratio over the ground truth pRF size. The solid lines indicate pRF estimates from the fixed-bar (red), log-bar (blue), and ground truth (dashed black). (C) Histogram of pRF size ratio values for the (C) fixed-bar and (D) log-bar stimulus. The green line indicates the mean of the distribution.

4.4 Discussion

This study examined the differences in the pRF estimates with (1) a fixed size drifting bar (fixed-bar) stimulus and (2) logarithmically-distorted drifting bar (log-bar) stimulus to address pRF estimate reliability and pRF size estimate stability.

4.4.1 pRF Estimate Reliability

On average, the intersession reliability of polar angle and eccentricity were excellent ($r > 0.9$) for the fixed-bar and log-bar in V1 to V3. These results are consistent with reported values for polar angle and eccentricity and support that pRF location estimates are robust and stable across acquisitions (Benson et al., 2018; Lage-Castellanos et al., 2020; Senden et al., 2014; van Dijk et al., 2016). The intersession reliability of pRF size was good ($r > 0.7$) for the fixed-bar stimulus, but even greater for the log-bar stimulus ($r > 0.88$) in V1 to V3. Our log-bar stimulus data are the first to show such high reliability coefficients for pRF size estimates. We infer that the log-bar stimulus was effective in eliciting more reliable activation throughout the visual field, which resulted in the greater stability in pRF size estimates.

This study also examined a foveal confluence region of interest. We found poor intersession reliability for all pRF estimates when using the fixed-bar stimulus ($r \simeq 0.5 - 0.6$). Reliability was good for polar angle and eccentricity ($r \simeq 0.8$), but pRF size had moderate ($r \simeq 0.6$) intersession reliability with the log-bar stimulus. It has been shown that pRF location estimates are more robust than pRF size estimates (Lage-Castellanos et al., 2020), so it is expected that the polar angle and eccentricity estimates would have better reliability than pRF size. Interestingly, the log-bar was able to achieve increased performance over the fixed-bar within the foveal confluence. We hypothesize that the poor pRF size intersession reliability in the foveal confluence might be due to the high degree of CMF (Dougherty et al., 2003). Cortex that represents central vision, like the foveal confluence, exhibits the most CMF scaling. In the human brain, this relationship translates to a large section of cortex containing the smallest pRFs. It is plausible that our chosen eccentricity distortion factor

did not compress the foveal component enough to elicit a reliable signal for the smallest receptive fields in the foveal confluence.

4.4.2 pRF Estimate Differences by Stimulus Type

Our results demonstrated several differences in pRF estimates when comparing the fixed-bar and the log-bar stimuli. On average, pRFs estimated from the fixed-bar stimulus had larger eccentricities and larger pRF sizes than log-bar pRFs. This result demonstrates a systematic bias towards more peripheral and larger pRFs when estimating with a drifting bar stimulus. As we hypothesized, the log-bar stimulus was able to estimate more pRFs that represented central vision. This tendency was reflected in the observation that more of the log-bar pRFs located within 0° to 2° eccentricity were retained after thresholding, and there was more variance explained across visual areas for these pRFs.

The results for foveal locations matched our pRF simulations. In the simulated pRF estimates, the fixed-bar stimulus produced larger pRF size estimates than the log-bar stimulus. The bias of enlarged pRF sizes was most prominent in pRFs with small eccentricities. The simulation results support our hypothesis that the log-bar was able to produce a more reliable response for smaller pRFs located at smaller eccentricities.

Individual CMF by eccentricity was also dependent on stimulus type. The CMF at a near foveal position of 1° was always larger for the log-bar than the fixed-bar stimulus. This result is consistent with larger CMF at the smallest eccentricity, although the decay rate was similar across stimulus types. As the local change in cortical distance was the same within each subject, the difference in measured CMF across stimulus types must come from the difference in local change in pRF location. Under this logic, the local change in pRF locations for the log-bar stimulus was smaller than for the fixed-bar stimulus. The CMF relationship with eccentricity that was measured in this study from the log-bar stimulus is consistent with CMF measurements made in humans with implanted electrodes (Cowey & Rolls, 1974).

We found pPI to be near constant, with pPI slightly decreasing as a function of eccentric-

ity for V1 to V3 within 1° to 8° eccentricity. This observation is consistent with previously reported pPI measured using the pRF method (Clavagnier et al., 2015; Harvey & Dumoulin, 2011). Since we were able to estimate pRFs located $< 1°$ eccentricity, we were also able to reconstruct the pPI within this range. Our results showed that pPI was still near constant when estimated from the fixed-bar stimulus, but rapidly decreases when using the log-bar stimulus.

We also report differences in pRF size estimates across hemispheres. We found that pRF size estimates were smaller from the left hemisphere than the right hemisphere. This translates to smaller pRF estimates in the right visual hemisphere than the left. This is consistent with previous work demonstrating asymmetric representation of pRF size in the visual field (Silva et al., 2018). Our results differ from Silva et al. (2018) in that we report the largest visual field asymmetry in pRF size estimates within the foveal confluence rather than in later visual areas.

4.4.3 Limitations

The limitations of the current study arise from technical capabilities and design choices. First, we were unable to stimulate the visual field beyond 8° eccentricity due to equipment constraints, and we chose to distort the log-bar to approximately match CMF properties of human early visual cortex. Therefore, we are unable to consider the effects the log-bar stimulus would have in more eccentric visual locations and in visual areas beyond early visual cortex (i.e., V4 – V7). It is possible that our distortion factor would not generalize to extrastriate visual cortex, and these higher order visual areas may require their own optimized stimulus configuration. Second, we did not implement other pRF models that incorporate non-linear visual computations like compressive spatial (Kay et al., 2013) or temporal (Zhou et al., 2018) summation, surround suppression (Zuiderbaan et al., 2012), or normalization (Aqil et al., 2021). The nonlinear pRF models may account for the differences in pRF sizes across the fixed-bar and log-bar at peripheral locations ($> 2°$ eccentricity) as this was an aspect of the data our simulations did not capture with a linear pRF model. Third, we used

a 100% contrast flickering checkerboard as the background texture for our stimuli. Flickering checkerboard stimuli are known to drive neural activity, however, the optimal background texture for visual neurons can vary. Visual cortex has demonstrated tuning for $1/f$ spectrum noise (Isherwood et al., 2017) and the Human Connectome Project implemented their stimulus with $1/f$ noise with embedded objects (Benson et al., 2018). It is possible that a combination of an optimized background texture and optimized stimulus aperture, like our log-bar stimulus, could lead to better pRF estimates and model performance, especially in higher-order visual areas.

4.4.4 Conclusion

In summary, this study presents an improvement to the stimulus types to be used for retinotopic mapping. Our logarithmically-distorted drifting bar produced highly reliable and more accurate pRF estimates than a standard drifting bar stimulus. Our results emphasize the importance of cortical magnification on pRF size estimate stability, especially for pRFs located near central vision. Here, we provide a fast and robust stimulus configuration that is suitable for investigating the organization of human visual cortex.

REFERENCES

Aitkin, L. M., Anderson, D. J., & Brugge, J. F. (1970). Tonotopic organization and discharge characteristics of single neurons in nuclei of the lateral lemniscus of the cat. *Journal of Neurophysiology*, *33*(3), 421–440. https://doi.org/10.1152/jn.1970.33.3.421

Aitkin, L. M., Fryman, S., Blake, D. W., & Webster, W. R. (1972). Responses of neurones in the rabbit inferior colliculus. I. Frequency-specificity and topographic arrangement. *Brain Research*, *47*(1), 77–90. https://doi.org/10.1016/0006-8993(72)90253-3

Aitkin, L. M., & Webster, W. R. (1971). Tonotopic organization in the medial geniculate body of the cat. *Brain Research*, *26*(2), 402–405. https://doi.org/10.1016/S0006-8993(71)80015-X

Allen, E. J., Mesik, J., Kay, K. N., & Oxenham, A. J. (2022). Distinct representations of tonotopy and pitch in human auditory cortex. *Journal of Neuroscience*, *42*(3), 416–434. https://doi.org/10.1523/JNEUROSCI.0960-21.2021

Allen, E. J., Moerel, M., Lage-Castellanos, A., De Martino, F., Formisano, E., & Oxenham, A. J. (2018). Encoding of natural timbre dimensions in human auditory cortex. *NeuroImage*, *166*, 60–70. https://doi.org/10.1016/j.neuroimage.2017.10.050

Alvarez, I., De Haas, B., Clark, C., Rees, G., & Schwarzkopf, D. (2015). Comparing different stimulus configurations for population receptive field mapping in human fMRI. *Frontiers in Human Neuroscience*, *9*. https://doi.org/10.3389/fnhum.2015.00096

Amano, K., Wandell, B. A., & Dumoulin, S. O. (2009). Visual field maps, population receptive field sizes, and visual field coverage in the human MT+ complex. *Journal of Neurophysiology*, *102*(5), 2704–2718. https://doi.org/10.1152/jn.00102.2009

Andersson, J. L., Skare, S., & Ashburner, J. (2003). How to correct susceptibility distortions in spin-echo echo-planar images: Application to diffusion tensor imaging. *NeuroImage*, *20*(2), 870–888. https://doi.org/10.1016/S1053-8119(03)00336-7

Aqil, M., Knapen, T., & Dumoulin, S. O. (2021). Divisive normalization unifies disparate response signatures throughout the human visual hierarchy. *Proceedings of the National Academy of Sciences*, *118*(46), e2108713118. https://doi.org/10.1073/pnas.2108713118

Arlen, H., & Harburg, E. Y. (1939). Over the Rainbow [Song featured in the MGM Picture]. *The Wizard of Oz*, Leo Feist.

Atilgan, H., Collignon, O., & Hasson, U. (2017). Structural neuroplasticity of the superior temporal plane in early and late blindness. *Brain and Language*, *170*, 71–81. https://doi.org/10.1016/j.bandl.2017.03.008

Avants, B., Epstein, C., Grossman, M., & Gee, J. (2008). Symmetric diffeomorphic image registration with cross-correlation: Evaluating automated labeling of elderly and neurodegenerative brain. *Medical Image Analysis*, *12*(1), 26–41. https://doi.org/10.1016/j.media.2007.06.004

Azzopardi, P., & Cowey, A. (1993). Preferential representation of the fovea in the primary visual cortex. *Nature*, *361*(6414), 719–721. https://doi.org/10.1038/361719a0

Baker, C. I., Dilks, D. D., Peli, E., & Kanwisher, N. (2008). Reorganization of visual processing in macular degeneration: Replication and clues about the role of foveal loss. *Vision Research*, *48*(18), 1910–1919. https://doi.org/10.1016/j.visres.2008.05.020

Baker, C. I., Peli, E., Knouf, N., & Kanwisher, N. G. (2005). Reorganization of visual processing in macular degeneration. *Journal of Neuroscience*, *25*(3), 614–618. https://doi.org/10.1523/JNEUROSCI.3476-04.2005

Barton, B., Venezia, J. H., Saberi, K., Hickok, G., & Brewer, A. A. (2012). Orthogonal acoustic dimensions define auditory field maps in human cortex. *Proceedings of the National Academy of Sciences*, *109*(50), 20738–20743. https://doi.org/10.1073/pnas.1213381109

Baseler, H. A., Gouws, A., Haak, K. V., Racey, C., Crossland, M. D., Tufail, A., Rubin, G. S., Cornelissen, F. W., & Morland, A. B. (2011). Large-scale remapping of visual cortex is absent in adult humans with macular degeneration. *Nature Neuroscience*, *14*(5), 649–655. https://doi.org/10.1038/nn.2793

Baumann, S., Griffiths, T. D., Sun, L., Petkov, C. I., Thiele, A., & Rees, A. (2011). Orthogonal representation of sound dimensions in the primate midbrain. *Nature Neuroscience*, *14*(4), 423–425. https://doi.org/10.1038/nn.2771

Behzadi, Y., Restom, K., Liau, J., & Liu, T. T. (2007). A component based noise correction method (CompCor) for BOLD and perfusion based fMRI. *NeuroImage*, *37*(1), 90–101. https://doi.org/10.1016/j.neuroimage.2007.04.042

Benson, N. C., Jamison, K. W., Arcaro, M. J., Vu, A. T., Glasser, M. F., Coalson, T. S., Van Essen, D. C., Yacoub, E., Ugurbil, K., Winawer, J., & Kay, K. (2018). The Human Connectome Project 7 Tesla retinotopy dataset: Description and population receptive field analysis. *Journal of Vision*, *18*(13), 23–23. https://doi.org/10.1167/18.13.23

Benson, N. C., Kupers, E. R., Barbot, A., Carrasco, M., & Winawer, J. (2021). Cortical magnification in human visual cortex parallels task performance around the visual field. *eLife*, *10*, e67685. https://doi.org/10.7554/eLife.67685

Benson, N. C., & Winawer, J. (2018). Bayesian analysis of retinotopic maps. *eLife*, *7*, e40224. https://doi.org/10.7554/eLife.40224

Bilecen, D., Scheffler, K., Schmid, N., Tschopp, K., & Seelig, J. (1998). Tonotopic organization of the human auditory cortex as detected by BOLD-FMRI. *Hearing Research*, *126*(1), 19–27. https://doi.org/10.1016/S0378-5955(98)00139-7

Binda, P., Thomas, J. M., Boynton, G. M., & Fine, I. (2013). Minimizing biases in estimating the reorganization of human visual areas with BOLD retinotopic mapping. *Journal of Vision*, *13*(7), 13–13. https://doi.org/10.1167/13.7.13

Boynton, G. M., Engel, S. A., Glover, G. H., & Heeger, D. J. (1996). Linear systems analysis of functional magnetic resonance imaging in human V1. *Journal of Neuroscience*, *16*(13), 4207–4221. https://doi.org/10.1523/JNEUROSCI.16-13-04207.1996

Boynton, G. M., Engel, S. A., & Heeger, D. J. (2012). Linear systems analysis of the fMRI signal. *NeuroImage*, *62*(2), 975–984. https://doi.org/10.1016/j.neuroimage.2012.01.082

Brainard, D. H. (1997). The psychophysics toolbox. *Spatial vision*, *10*(4), 433–436.

Brewer, A. A., & Barton, B. (2012). Effects of healthy aging on human primary visual cortex. *Health*, *4*(9A), 695–702. https://doi.org/10.4236/health.2012.429109

Brindley, G. S., & Lewin, W. S. (1968). The sensations produced by electrical stimulation of the visual cortex. *The Journal of Physiology*, *196*(2), 479–493. https://doi.org/10.1113/jphysiol.1968.sp008519

Chang, K. H., Thomas, J. M., Boynton, G. M., & Fine, I. (2017). Reconstructing tone sequences from functional magnetic resonance imaging blood-oxygen level dependent responses within human primary auditory cortex. *Frontiers in Psychology*, *8*. https://doi.org/10.3389/fpsyg.2017.01983

Clavagnier, S., Dumoulin, S. O., & Hess, R. F. (2015). Is the cortical deficit in amblyopia due to reduced cortical magnification, loss of neural resolution, or neural disorganization? *Journal of Neuroscience*, *35*(44), 14740–14755. https://doi.org/10.1523/JNEUROSCI.1101-15.2015

Clopton, B. M., Winfield, J. A., & Flammino, F. J. (1974). Tonotopic organization: Review and analysis. *Brain Research*, *76*(1), 1–20. https://doi.org/10.1016/0006-8993(74)90509-5

Coullon, G. S. L., Emir, U. E., Fine, I., Watkins, K. E., & Bridge, H. (2015). Neurochemical changes in the pericalcarine cortex in congenital blindness attributable to bilateral anophthalmia. *Journal of Neurophysiology*, *114*(3), 1725–1733. https://doi.org/10.1152/jn.00567.2015

Cowey, A., & Rolls, E. T. (1974). Human cortical magnification factor and its relation to visual acuity. *Experimental Brain Research*, *21*(5), 447–454. https://doi.org/10.1007/BF00237163

Cox, R. W., & Hyde, J. S. (1997). Software tools for analysis and visualization of fMRI data. *NMR Biomed*, *10*(4-5), 171–178. https://doi.org/10.1002/(sici)1099-1492(199706/08)10:4/5<171::aid-nbm453>3.0.co;2-l

Da Costa, S., Saenz, M., Clarke, S., & van der Zwaag, W. (2015). Tonotopic gradients in human primary auditory cortex: Concurring evidence from high-resolution 7 T and 3 T fMRI. *Brain Topography*, *28*(1), 66–69. https://doi.org/10.1007/s10548-014-0388-0

Da Costa, S., van der Zwaag, W., Marques, J. P., Frackowiak, R. S. J., Clarke, S., & Saenz, M. (2011). Human primary auditory cortex follows the shape of Heschl's gyrus. *Journal of Neuroscience*, *31*(40), 14067–14075. https://doi.org/10.1523/JNEUROSCI.2000-11.2011

Da Costa, S., van der Zwaag, W., Miller, L. M., Clarke, S., & Saenz, M. (2013). Tuning in to sound: Frequency-selective attentional filter in human primary auditory cortex. *Journal of Neuroscience*, *33*(5), 1858–1863. https://doi.org/10.1523/JNEUROSCI.4405-12.2013

Dale, A. M., Fischl, B., & Sereno, M. I. (1999). Cortical surface-based analysis: I. Segmentation and surface reconstruction. *NeuroImage*, *9*(2), 179–194. https://doi.org/10.1006/nimg.1998.0395

Daniel, P. M., & Whitteridge, D. (1961). The representation of the visual field on the cerebral cortex in monkeys. *J Physiol*, *159*(2), 203–221. https://doi.org/10.1113/jphysiol.1961.sp006803

De Angelis, V., De Martino, F., Moerel, M., Santoro, R., Hausfeld, L., & Formisano, E. (2018). Cortical processing of pitch: Model-based encoding and decoding of auditory fMRI responses to real-life sounds. *NeuroImage*, *180*, 291–300. https://doi.org/10.1016/j.neuroimage.2017.11.020

De Volder, A. G., Bol, A., Blin, J., Robert, A., Arno, P., Grandin, C., Michel, C., & Veraart, C. (1997). Brain energy metabolism in early blind subjects: Neural activity in the visual cortex. *Brain Research*, *750*(1), 235–244. https://doi.org/10.1016/S0006-8993(96)01352-2

DeSimone, K., Viviano, J. D., & Schneider, K. A. (2015). Population receptive field estimation reveals new retinotopic maps in human subcortex. *Journal of Neuroscience*, *35*(27), 9836–9847. https://doi.org/10.1523/JNEUROSCI.3840-14.2015

DeYoe, E. A., Bandettini, P., Neitz, J., Miller, D., & Winans, P. (1994). Functional magnetic resonance imaging (FMRI) of the human brain. *Journal of Neuroscience Methods*, *54*(2), 171–187. https://doi.org/10.1016/0165-0270(94)90191-0

Dick, F., Taylor Tierney, A., Lutti, A., Josephs, O., Sereno, M. I., & Weiskopf, N. (2012). In vivo functional and myeloarchitectonic mapping of human primary auditory areas. *Journal of Neuroscience*, *32*(46), 16095–16105. https://doi.org/10.1523/JNEUROSCI.1712-12.2012

Dilks, D. D., Baker, C. I., Peli, E., & Kanwisher, N. (2009). Reorganization of visual processing in macular degeneration is not specific to the "preferred retinal locus". *Journal of Neuroscience*, *29*(9), 2768–2773. https://doi.org/10.1523/JNEUROSCI.5258-08.2009

Dilks, D. D., Julian, J. B., Peli, E., & Kanwisher, N. (2014). Reorganization of visual processing in age-related macular degeneration depends on foveal loss. *Optometry and Vision Science*, *91*(8). https://doi.org/10.1097/opx.0000000000000325

Dobelle, W., Turkel, J., Henderson, D., & Evans, J. (1979). Mapping the representation of the visual field by electrical stimulation of human visual cortex. *American journal of ophthalmology*, *88*(4), 727–735. https://doi.org/10.1016/0002-9394(79)90673-1

Dormal, G., Lepore, F., Harissi-Dagher, M., Albouy, G., Bertone, A., Rossion, B., & Collignon, O. (2015). Tracking the evolution of crossmodal plasticity and visual functions before and after sight restoration. *Journal of Neurophysiology*, *113*(6), 1727–1742. https://doi.org/10.1152/jn.00420.2014

Dougherty, R. F., Koch, V. M., Brewer, A. A., Fischer, B., Modersitzki, J., & Wandell, B. A. (2003). Visual field representations and locations of visual areas V1/2/3 in human visual cortex. *Journal of Vision*, *3*(10), 1–1. https://doi.org/10.1167/3.10.1

Dow, B. M., Snyder, A. Z., Vautin, R. G., & Bauer, R. (1981). Magnification factor and receptive field size in foveal striate cortex of the monkey. *Experimental Brain Research*, *44*(2), 213–228. https://doi.org/10.1007/BF00237343

Dumoulin, S. O., & Wandell, B. A. (2008). Population receptive field estimates in human visual cortex. *NeuroImage*, *39*(2), 647–660. https://doi.org/10.1016/j.neuroimage.2007.09.034

Elbert, T., Sterr, A., Rockstroh, B., Pantev, C., Müller, M. M., & Taub, E. (2002). Expansion of the tonotopic area in the auditory cortex of the blind. *Journal of Neuroscience*, *22*(22), 9941–9944. https://doi.org/10.1523/JNEUROSCI.22-22-09941.2002

Engel, S. A., Glover, G. H., & Wandell, B. A. (1997). Retinotopic organization in human visual cortex and the spatial precision of functional MRI. *Cerebral Cortex*, *7*(2), 181–192. https://doi.org/10.1093/cercor/7.2.181

Engel, S. A., Rumelhart, D. E., Wandell, B. A., Lee, A. T., Glover, G. H., Chichilnisky, E.-J., & Shadlen, M. N. (1994). fMRI of human visual cortex. *Nature*, *369*(6481), 525–525. https://doi.org/10.1038/369525a0

Esteban, O., Markiewicz, C. J., Blair, R. W., Moodie, C. A., Isik, A. I., Erramuzpe, A., Kent, J. D., Goncalves, M., DuPre, E., Snyder, M., Oya, H., Ghosh, S. S., Wright, J., Durnez, J., Poldrack, R. A., & Gorgolewski, K. J. (2019). fMRIPrep: A robust preprocessing pipeline for functional MRI. *Nature Methods*, *16*(1), 111–116. https://doi.org/10.1038/s41592-018-0235-4

Ethofer, T., Van De Ville, D., Scherer, K., & Vuilleumier, P. (2009). Decoding of emotional information in voice-sensitive cortices. *Current Biology*, *19*(12), 1028–1033. https://doi.org/10.1016/j.cub.2009.04.054

Fisher, R. A. (1915). Frequency distribution of the values of the correlation coefficient in samples from an indefinitely large population. *Biometrika*, *10*(4), 507–521. https://doi.org/10.2307/2331838

Formisano, E., Kim, D.-S., Di Salle, F., van de Moortele, P.-F., Ugurbil, K., & Goebel, R. (2003). Mirror-symmetric tonotopic maps in human primary auditory cortex. *Neuron*, *40*(4), 859–869. https://doi.org/10.1016/S0896-6273(03)00669-X

Formisano, E., Martino, F. D., Bonte, M., & Goebel, R. (2008). "Who" is saying "what"? Brain-based decoding of human voice and speech. *Science*, *322*(5903), 970–973. https://doi.org/10.1126/science.1164318

Fox, P., Miezin, F., Allman, J., Van Essen, D., & Raichle, M. (1987). Retinotopic organization of human visual cortex mapped with positron- emission tomography. *Journal of Neuroscience*, *7*(3), 913–922. https://doi.org/10.1523/JNEUROSCI.07-03-00913.1987

Friston, K., Fletcher, P., Josephs, O., Holmes, A., Rugg, M., & Turner, R. (1998). Event-related fMRI: Characterizing differential responses. *NeuroImage*, *7*(1), 30–40. https://doi.org/10.1006/nimg.1997.0306

Friston, K., Mechelli, A., Turner, R., & Price, C. (2000). Nonlinear responses in fMRI: The Balloon model, Volterra kernels, and other hemodynamics. *NeuroImage*, *12*(4), 466–477. https://doi.org/10.1006/nimg.2000.0630

Goebel, R., Esposito, F., & Formisano, E. (2006). Analysis of functional image analysis contest (FIAC) data with Brainvoyager QX: From single-subject to cortically aligned group general linear model analysis and self-organizing group independent component analysis. *Human Brain Mapping*, *27*(5), 392–401. https://doi.org/10.1002/hbm.20249

Goldstein, M. H., Abeles, M., Daly, R. L., & McIntosh, J. (1970). Functional architecture in cat primary auditory cortex: Tonotopic organization. *Journal of Neurophysiology*, *33*(1), 188–197. https://doi.org/10.1152/jn.1970.33.1.188

Gougoux, F., Belin, P., Voss, P., Lepore, F., Lassonde, M., & Zatorre, R. J. (2009). Voice perception in blind persons: A functional magnetic resonance imaging study. *Neuropsychologia*, *47*(13), 2967–2974. https://doi.org/10.1016/j.neuropsychologia.2009.06.027

Gougoux, F., Lepore, F., Lassonde, M., Voss, P., Zatorre, R. J., & Belin, P. (2004). Pitch discrimination in the early blind. *Nature*, *430*(6997), 309–309. https://doi.org/10.1038/430309a

Greve, D. N., & Fischl, B. (2009). Accurate and robust brain image alignment using boundary-based registration. *NeuroImage*, *48*(1), 63–72. https://doi.org/10.1016/j.neuroimage.2009.06.060

Griswold, M. A., Jakob, P. M., Heidemann, R. M., Nittka, M., Jellus, V., Wang, J., Kiefer, B., & Haase, A. (2002). Generalized autocalibrating partially parallel acquisitions (GRAPPA). *Magnetic Resonance in Medicine*, *47*(6), 1202–1210. https://doi.org/10.1002/mrm.10171

Haak, K. V., Cornelissen, F. W., & Morland, A. B. (2012). Population receptive field dynamics in human visual cortex. *PLOS ONE*, *7*(5), 1–8. https://doi.org/10.1371/journal.pone.0037686

Hackett, T. A. (2008). Anatomical organization of the auditory cortex. *J Am Acad Audiol*, *19*(10), 774–779. https://doi.org/10.3766/jaaa.19.10.5

Hackett, T., Stepniewska, I., & Kaas, J. (1998). Subdivisions of auditory cortex and ipsilateral cortical connections of the parabelt auditory cortex in macaque monkeys. *Journal of Comparative Neurology*, *394*(4), 475–495. https://doi.org/10.1002/(SICI)1096-9861(19980518)394:4<475::AID-CNE6>3.0.CO;2-Z

Harline, L., Washington, N., Disney, W., Edwards, C., Langford, F., Lawrence, J., & Sosnik, H. (1940). When you Wish Upon a Star [Song from Walt Disney's "Pinocchio"]. *Pinocchio*, Decca.

Harvey, B. M., & Dumoulin, S. O. (2011). The relationship between cortical magnification factor and population receptive field size in human visual cortex: Constancies in cortical architecture. *Journal of Neuroscience*, *31*(38), 13604–13612. https://doi.org/10.1523/JNEUROSCI.2572-11.2011

Himmelberg, M. M., Kurzawski, J. W., Benson, N. C., Pelli, D. G., Carrasco, M., & Winawer, J. (2021). Cross-dataset reproducibility of human retinotopic maps. *NeuroImage*, *244*, 118609. https://doi.org/10.1016/j.neuroimage.2021.118609

Holm, S. (1979). A simple sequentially rejective multiple test procedure. *Scandinavian Journal of Statistics*, *6*(2), 65–70. http://www.jstor.org/stable/4615733

Holmes, G. (1918). Disturbances of visual orientation. *Br J Ophthalmol*, *2*(9), 449–468. https://doi.org/10.1136/bjo.2.9.449

Horton, J. C., & Hoyt, W. F. (1991). The representation of the visual field in human striate cortex: A revision of the classic Holmes map. *Archives of Ophthalmology*, *109*(6), 816–824. https://doi.org/10.1001/archopht.1991.01080060080030

Hubel, D. H., & Wiesel, T. N. (1962). Receptive fields, binocular interaction and functional architecture in the cat's visual cortex. *J Physiol*, *160*(1), 106–154. https://doi.org/10.1113/jphysiol.1962.sp006837

Hubel, D. H., & Wiesel, T. N. (1974). Uniformity of monkey striate cortex: A parallel relationship between field size, scatter, and magnification factor. *Journal of Comparative Neurology*, *158*(3), 295–305. https://doi.org/10.1002/cne.901580305

Huber, E., Chang, K., Alvarez, I., Hundle, A., Bridge, H., & Fine, I. (2019). Early blindness shapes cortical representations of auditory frequency within auditory cortex. *Journal of Neuroscience*, *39*(26), 5143–5152. https://doi.org/10.1523/JNEUROSCI.2896-18.2019

Huber, E., Jiang, F., & Fine, I. (2019). Responses in area hMT+ reflect tuning for both auditory frequency and motion after blindness early in life. *Proceedings of the National Academy of Sciences*, *116*(20), 10081–10086. https://doi.org/10.1073/pnas.1815376116

Hummer, A., Ritter, M., Tik, M., Ledolter, A., Woletz, M., Holder, G., Dumoulin, S., Schmidt-Erfurth, U., & Windischberger, C. (2016). Eyetracker-based gaze correction for robust mapping of population receptive fields. *NeuroImage*, *142*, 211–224. https://doi.org/10.1016/j.neuroimage.2016.07.003

Humphries, C., Liebenthal, E., & Binder, J. R. (2010). Tonotopic organization of human auditory cortex. *NeuroImage*, *50*(3), 1202–1211. https://doi.org/10.1016/j.neuroimage.2010.01.046

Infanti, E., & Schwarzkopf, D. S. (2020). Mapping sequences can bias population receptive field estimates. *NeuroImage*, *211*, 116636. https://doi.org/10.1016/j.neuroimage.2020.116636

Jammalamadaka, S. R., & Sengupta, A. (2001). *Topics in circular statistics* (Vol. 5). World Scientific.

Jenkinson, M., Bannister, P., Brady, M., & Smith, S. (2002). Improved optimization for the robust and accurate linear registration and motion correction of brain images. *NeuroImage*, *17*(2), 825–841. https://doi.org/10.1006/nimg.2002.1132

Jiang, F., Stecker, G. C., & Fine, I. (2014). Auditory motion processing after early blindness. *Journal of Vision*, *14*(13), 4–4. https://doi.org/10.1167/14.13.4

Josef Golubic, S., Susac, A., Grilj, V., Ranken, D., Huonker, R., Haueisen, J., & Supek, S. (2011). Size matters: MEG empirical and simulation study on source localization of the earliest visual activity in the occipital cortex. *Medical & Biological Engineering & Computing*, *49*(5), 545–554. https://doi.org/10.1007/s11517-011-0764-9

Kay, K. N., Naselaris, T., Prenger, R. J., & Gallant, J. L. (2008). Identifying natural images from human brain activity. *Nature*, *452*(7185), 352–355. https://doi.org/10.1038/nature06713

Kay, K. N., Weiner, K. S., & Grill-Spector, K. (2015). Attention reduces spatial uncertainty in human ventral temporal cortex. *Current Biology*, *25*(5), 595–600. https://doi.org/10.1016/j.cub.2014.12.050

Kay, K. N., Winawer, J., Mezer, A., & Wandell, B. A. (2013). Compressive spatial summation in human visual cortex. *Journal of Neurophysiology*, *110*(2), 481–494. https://doi.org/10.1152/jn.00105.2013

Klein, A., Ghosh, S. S., Bao, F. S., Giard, J., Häme, Y., Stavsky, E., Lee, N., Rossa, B., Reuter, M., Chaibub Neto, E., & Keshavan, A. (2017). Mindboggling morphometry of human brains. *PLOS Computational Biology*, *13*(2), 1–40. https://doi.org/10.1371/journal.pcbi.1005350

Klein, B. P., Harvey, B. M., & Dumoulin, S. O. (2014). Attraction of position preference by spatial attention throughout human visual cortex. *Neuron*, *84*(1), 227–237. https://doi.org/10.1016/j.neuron.2014.08.047

Kleiner, M., Brainard, D., & Pelli, D. (2007). What's new in Psychtoolbox-3? [30th European Conference on Visual Perception (ECVP 2007)]. *Perception*, *36*, 14.

Korte, M., & Rauschecker, J. P. (1993). Auditory spatial tuning of cortical neurons is sharpened in cats with early blindness. *Journal of Neurophysiology*, *70*(4), 1717–1721. https://doi.org/10.1152/jn.1993.70.4.1717

Kujala, T., Alho, K., Paavilainen, P., Summala, H., & Näätänen, R. (1992). Neural plasticity in processing of sound location by the early blind: An event-related potential study. *Electroencephalography and Clinical Neurophysiology/Evoked Potentials Section*, *84*(5), 469–472. https://doi.org/10.1016/0168-5597(92)90034-9

Kujala, T., Huotilainen, M., Sinkkonen, J., Ahonen, A. I., Alho, K., Hämälä:inen, M. S., Ilmoniemi, R. J., Kajola, M., Knuutila, J. E., Lavikainen, J., Salonen, O., Simola, J., Standertskjöld-Nordenstam, C.-G., Tiitinen, H., Tissari, S. O., & Näätänen, R. (1995). Visual cortex activation in blind humans during sound discrimination. *Neuroscience Letters*, *183*(1), 143–146. https://doi.org/10.1016/0304-3940(94)11135-6

Lage-Castellanos, A., De Martino, F., Ghose, G. M., Gulban, O. F., & Moerel, M. (2022). Selective attention sharpens population receptive fields in human auditory cortex. *Cerebral Cortex*. https://doi.org/10.1093/cercor/bhac427

Lage-Castellanos, A., Valente, G., Senden, M., & De Martino, F. (2020). Investigating the reliability of population receptive field size estimates using fMRI. *Frontiers in Neuroscience*, *14*. https://doi.org/10.3389/fnins.2020.00825

Langers, D. R., Krumbholz, K., Bowtell, R. W., & Hall, D. A. (2014). Neuroimaging paradigms for tonotopic mapping (I): The influence of sound stimulus type. *NeuroImage*, *100*, 650–662. https://doi.org/10.1016/j.neuroimage.2014.07.044

Langers, D. R., Sanchez-Panchuelo, R. M., Francis, S. T., Krumbholz, K., & Hall, D. A. (2014). Neuroimaging paradigms for tonotopic mapping (II): The influence of acqui-

sition protocol. *NeuroImage*, *100*, 663–675. https://doi.org/10.1016/j.neuroimage.2014.07.042

Langers, D. R., & van Dijk, P. (2011). Mapping the tonotopic organization in human auditory cortex with minimally salient acoustic stimulation. *Cerebral Cortex*, *22*(9), 2024–2038. https://doi.org/10.1093/cercor/bhr282

Langner, G., Sams, M., Heil, P., & Schulze, H. (1997). Frequency and periodicity are represented in orthogonal maps in the human auditory cortex: Evidence from magnetoencephalography. *Journal of Comparative Physiology A*, *181*(6), 665–676. https://doi.org/10.1007/s003590050148

Langner, G., Dinse, H., & Godde, B. (2009). A map of periodicity orthogonal to frequency representation in the cat auditory cortex. *Frontiers in Integrative Neuroscience*, *3*. https://doi.org/10.3389/neuro.07.027.2009

Lauter, J. L., Herscovitch, P., Formby, C., & Raichle, M. E. (1985). Tonotopic organization in human auditory cortex revealed by positron emission tomography. *Hearing Research*, *20*(3), 199–205. https://doi.org/10.1016/0378-5955(85)90024-3

Lerma-Usabiaga, G., Benson, N., Winawer, J., & Wandell, B. A. (2020). A validation framework for neuroimaging software: The case of population receptive fields. *PLOS Computational Biology*, *16*(6), 1–18. https://doi.org/10.1371/journal.pcbi.1007924

Linhardt, D., Pawloff, M., Hummer, A., Woletz, M., Tik, M., Ritter, M., Schmidt-Erfurth, U., & Windischberger, C. (2021). Combining stimulus types for improved coverage in population receptive field mapping. *NeuroImage*, *238*, 118240. https://doi.org/10.1016/j.neuroimage.2021.118240

Lister, W. T., & Holmes, G. (1916). Disturbances of vision from cerebral lesions, with special reference to the cortical representation of the macula. *Proceedings of the Royal Society of Medicine*, *9*(Sect_Ophthalmol), 57–96. https://doi.org/10.1177/003591571600901711

MATLAB. (2022). *Version 9.13.0 (r2022a)*. The MathWorks Inc.

Meng, X., Kao, J. P. Y., Lee, H.-K., & Kanold, P. O. (2017). Intracortical circuits in thalamorecipient layers of auditory cortex refine after visual deprivation. *eNeuro*, *4*(2). https://doi.org/10.1523/ENEURO.0092-17.2017

Meng, X., Kao, J. P., Lee, H.-K., & Kanold, P. O. (2015). Visual deprivation causes refinement of intracortical circuits in the auditory cortex. *Cell Reports*, *12*(6), 955–964. https://doi.org/10.1016/j.celrep.2015.07.018

Miyawaki, Y., Uchida, H., Yamashita, O., Sato, M.-a., Morito, Y., Tanabe, H. C., Sadato, N., & Kamitani, Y. (2008). Visual image reconstruction from human brain activity using a combination of multiscale local image decoders. *Neuron*, *60*(5), 915–929. https://doi.org/10.1016/j.neuron.2008.11.004

Moeller, S., Yacoub, E., Olman, C. A., Auerbach, E., Strupp, J., Harel, N., & Uğurbil, K. (2010). Multiband multislice GE-EPI at 7 Tesla, with 16-fold acceleration using partial parallel imaging with application to high spatial and temporal whole-brain fMRI. *Magnetic Resonance in Medicine*, *63*(5), 1144–1153. https://doi.org/10.1002/mrm.22361

Moerel, M., De Martino, F., & Formisano, E. (2012). Processing of natural sounds in human auditory cortex: Tonotopy, spectral tuning, and relation to voice sensitivity. *Journal of Neuroscience*, *32*(41), 14205–14216. https://doi.org/10.1523/JNEUROSCI.1388-12.2012

Moerel, M., De Martino, F., & Formisano, E. (2014). An anatomical and functional topography of human auditory cortical areas. *Frontiers in Neuroscience*, *8*. https://doi.org/10.3389/fnins.2014.00225

Moerel, M., De Martino, F., Kemper, V. G., Schmitter, S., Vu, A. T., Uğurbil, K., Formisano, E., & Yacoub, E. (2018). Sensitivity and specificity considerations for fMRI encoding, decoding, and mapping of auditory cortex at ultra-high field. *NeuroImage*, *164*, 18–31. https://doi.org/10.1016/j.neuroimage.2017.03.063

Moerel, M., De Martino, F., Santoro, R., Ugurbil, K., Goebel, R., Yacoub, E., & Formisano, E. (2013). Processing of natural sounds: Characterization of multipeak spectral tuning

in human auditory cortex. *Journal of Neuroscience*, *33*(29), 11888–11898. https://doi.org/10.1523/JNEUROSCI.5306-12.2013

Moerel, M., De Martino, F., Santoro, R., Yacoub, E., & Formisano, E. (2015). Representation of pitch chroma by multi-peak spectral tuning in human auditory cortex. *NeuroImage*, *106*, 161–169. https://doi.org/10.1016/j.neuroimage.2014.11.044

Naselaris, T., & Kay, K. N. (2015). Resolving ambiguities of MVPA using explicit models of representation. *Trends in Cognitive Sciences*, *19*(10), 551–554. https://doi.org/10.1016/j.tics.2015.07.005

Naselaris, T., Kay, K. N., Nishimoto, S., & Gallant, J. L. (2011). Encoding and decoding in fMRI. *NeuroImage*, *56*(2), 400–410. https://doi.org/10.1016/j.neuroimage.2010.07.073

Naselaris, T., Prenger, R. J., Kay, K. N., Oliver, M., & Gallant, J. L. (2009). Bayesian reconstruction of natural images from human brain activity. *Neuron*, *63*(6), 902–915. https://doi.org/10.1016/j.neuron.2009.09.006

Nishimoto, S., Vu, A. T., Naselaris, T., Benjamini, Y., Yu, B., & Gallant, J. L. (2011). Reconstructing visual experiences from brain activity evoked by natural movies. *Current Biology*, *21*(19), 1641–1646. https://doi.org/10.1016/j.cub.2011.08.031

Norman, L., & Thaler, L. (2017). Human echolocation - spatial resolution and signal properties. In *Biologically-inspired radar and sonar: Lessons from nature* (pp. 209–227). Institution of Engineering; Technology. https://doi.org/10.1049/sbra514e_ch10

Ogawa, S., Lee, T. M., Kay, A. R., & Tank, D. W. (1990). Brain magnetic resonance imaging with contrast dependent on blood oxygenation. *Proceedings of the National Academy of Sciences*, *87*(24), 9868–9872. https://doi.org/10.1073/pnas.87.24.9868

Ogawa, S., & Lee, T.-M. (1990). Magnetic resonance imaging of blood vessels at high fields: In vivo and in vitro measurements and image simulation. *Magnetic Resonance in Medicine*, *16*(1), 9–18. https://doi.org/10.1002/mrm.1910160103

Ogawa, S., Lee, T.-M., Nayak, A. S., & Glynn, P. (1990). Oxygenation-sensitive contrast in magnetic resonance image of rodent brain at high magnetic fields. *Magnetic Resonance in Medicine*, *14*(1), 68–78. https://doi.org/10.1002/mrm.1910140108

Pelli, D. G. (1997). The VideoToolbox software for visual psychophysics: Transforming numbers into movies. *Spatial Vision*, *10*(4), 437–442. https://doi.org/10.1163/156856897X00366

Petrus, E., Isaiah, A., Jones, A. P., Li, D., Wang, H., Lee, H.-K., & Kanold, P. O. (2014). Crossmodal induction of thalamocortical potentiation leads to enhanced information processing in the auditory cortex. *Neuron*, *81*(3), 664–673. https://doi.org/10.1016/j.neuron.2013.11.023

Puckett, A. M., Bollmann, S., Junday, K., Barth, M., & Cunnington, R. (2020). Bayesian population receptive field modeling in human somatosensory cortex. *NeuroImage*, *208*, 116465. https://doi.org/10.1016/j.neuroimage.2019.116465

Rademacher, J., Morosan, P., Schormann, T., Schleicher, A., Werner, C., Freund, H.-J., & Zilles, K. (2001). Probabilistic mapping and volume measurement of human primary auditory cortex. *NeuroImage*, *13*(4), 669–683. https://doi.org/10.1006/nimg.2000.0714

Recanzone, G. H., Jenkins, W. M., Hradek, G. T., & Merzenich, M. M. (1992). Progressive improvement in discriminative abilities in adult owl monkeys performing a tactile frequency discrimination task. *Journal of Neurophysiology*, *67*(5), 1015–1030. https://doi.org/10.1152/jn.1992.67.5.1015

Recanzone, G., Schreiner, C., & Merzenich, M. (1993). Plasticity in the frequency representation of primary auditory cortex following discrimination training in adult owl monkeys. *Journal of Neuroscience*, *13*(1), 87–103. https://doi.org/10.1523/JNEUROSCI.13-01-00087.1993

Rokem, A., Yeatman, J. D., Pestilli, F., Kay, K. N., Mezer, A., van der Walt, S., & Wandell, B. A. (2015). Evaluating the accuracy of diffusion mri models in white matter. *PLOS ONE*, *10*(4), 1–26. https://doi.org/10.1371/journal.pone.0123272

Romani, G. L., Williamson, S. J., & Kaufman, L. (1982). Tonotopic organization of the human auditory cortex. *Science*, *216*(4552), 1339–1340. https://doi.org/10.1126/science.7079770

Rose, J. E., Greenwood, D. D., Goldberg, J. M., & Hind, J. E. (1963). Some discharge characteristics of single neurons in the inferior colliculus of the cat. I. Tonotopical organization, relation of spike-counts to tone intensity, and firing patterns of single elements. *Journal of Neurophysiology*, *26*(2), 294–320. https://doi.org/10.1152/jn.1963.26.2.294

Sadagopan, S., & Wang, X. (2009). Nonlinear spectrotemporal interactions underlying selectivity for complex sounds in auditory cortex. *Journal of Neuroscience*, *29*(36), 11192–11202. https://doi.org/10.1523/JNEUROSCI.1286-09.2009

Saenz, M., & Langers, D. R. (2014). Tonotopic mapping of human auditory cortex. *Hearing Research*, *307*, 42–52. https://doi.org/10.1016/j.heares.2013.07.016

Santoro, R., Moerel, M., De Martino, F., Goebel, R., Ugurbil, K., Yacoub, E., & Formisano, E. (2014). Encoding of natural sounds at multiple spectral and temporal resolutions in the human auditory cortex. *PLOS Computational Biology*, *10*(1), 1–14. https://doi.org/10.1371/journal.pcbi.1003412

Santoro, R., Moerel, M., Martino, F. D., Valente, G., Ugurbil, K., Yacoub, E., & Formisano, E. (2017). Reconstructing the spectrotemporal modulations of real-life sounds from fMRI response patterns. *Proceedings of the National Academy of Sciences*, *114*(18), 4799–4804. https://doi.org/10.1073/pnas.1617622114

Satterthwaite, T. D., Elliott, M. A., Gerraty, R. T., Ruparel, K., Loughead, J., Calkins, M. E., Eickhoff, S. B., Hakonarson, H., Gur, R. C., Gur, R. E., & Wolf, D. H. (2013). An improved framework for confound regression and filtering for control of motion artifact in the preprocessing of resting-state functional connectivity data. *NeuroImage*, *64*, 240–256. https://doi.org/10.1016/j.neuroimage.2012.08.052

Schellekens, W., Thio, M., Badde, S., Winawer, J., Ramsey, N., & Petridou, N. (2021). A touch of hierarchy: Population receptive fields reveal fingertip integration in Brod-

mann areas in human primary somatosensory cortex. *Brain Structure and Function*, *226*(7), 2099–2112. https://doi.org/10.1007/s00429-021-02309-5

Schellekens, W., Petridou, N., & Ramsey, N. F. (2018). Detailed somatotopy in primary motor and somatosensory cortex revealed by Gaussian population receptive fields. *NeuroImage*, *179*, 337–347. https://doi.org/10.1016/j.neuroimage.2018.06.062

Schira, M. M., Wade, A. R., & Tyler, C. W. (2007). Two-dimensional mapping of the central and parafoveal visual field to human visual cortex. *Journal of Neurophysiology*, *97*(6), 4284–4295. https://doi.org/10.1152/jn.00972.2006

Schönwiesner, M., & Zatorre, R. J. (2009). Spectro-temporal modulation transfer function of single voxels in the human auditory cortex measured with high-resolution fMRI. *Proceedings of the National Academy of Sciences*, *106*(34), 14611–14616. https://doi.org/10.1073/pnas.0907682106

Schwarzkopf, D. S., Anderson, E. J., de Haas, B., White, S. J., & Rees, G. (2014). Larger extrastriate population receptive fields in autism spectrum disorders. *Journal of Neuroscience*, *34*(7), 2713–2724. https://doi.org/10.1523/JNEUROSCI.4416-13.2014

Senden, M., Reithler, J., Gijsen, S., & Goebel, R. (2014). Evaluating population receptive field estimation frameworks in terms of robustness and reproducibility. *PLOS ONE*, *9*(12), 1–30. https://doi.org/10.1371/journal.pone.0114054

Sereno, M. I., Dale, A. M., Reppas, J. B., Kwong, K. K., Belliveau, J. W., Brady, T. J., Rosen, B. R., & Tootell, R. B. H. (1995). Borders of multiple visual areas in humans revealed by functional magnetic resonance imaging. *Science*, *268*(5212), 889–893. https://doi.org/10.1126/science.7754376

Silva, M. F., Brascamp, J. W., Ferreira, S., Castelo-Branco, M., Dumoulin, S. O., & Harvey, B. M. (2018). Radial asymmetries in population receptive field size and cortical magnification factor in early visual cortex. *NeuroImage*, *167*, 41–52. https://doi.org/10.1016/j.neuroimage.2017.11.021

Sprague, T. C., & Serences, J. T. (2013). Attention modulates spatial priority maps in the human occipital, parietal and frontal cortices. *Nature Neuroscience*, *16*(12), 1879–1887. https://doi.org/10.1038/nn.3574

Stevens, A. A., & Weaver, K. E. (2009). Functional characteristics of auditory cortex in the blind. *Behavioural Brain Research*, *196*(1), 134–138. https://doi.org/10.1016/j.bbr.2008.07.041

Striem-Amit, E., Hertz, U., & Amedi, A. (2011). Extensive cochleotopic mapping of human auditory cortical fields obtained with phase-encoding fMRI. *PLOS ONE*, *6*(3), 1–18. https://doi.org/10.1371/journal.pone.0017832

Talavage, T. M., Sereno, M. I., Melcher, J. R., Ledden, P. J., Rosen, B. R., & Dale, A. M. (2004). Tonotopic organization in human auditory cortex revealed by progressions of frequency sensitivity. *Journal of Neurophysiology*, *91*(3), 1282–1296. https://doi.org/10.1152/jn.01125.2002

Temperley, D. (2008). A probabilistic model of melody perception. *Cognitive Science*, *32*(2), 418–444. https://doi.org/10.1080/03640210701864089

Temperley, D. (2014). Probabilistic models of melodic interval. *Music Perception*, *32*(1), 85–99. https://doi.org/10.1525/mp.2014.32.1.85

Thomas, J. M., Huber, E., Stecker, G. C., Boynton, G. M., Saenz, M., & Fine, I. (2015). Population receptive field estimates of human auditory cortex. *NeuroImage*, *105*, 428–439. https://doi.org/10.1016/j.neuroimage.2014.10.060

Tisdall, M. D., Hess, A. T., Reuter, M., Meintjes, E. M., Fischl, B., & van der Kouwe, A. J. W. (2012). Volumetric navigators for prospective motion correction and selective reacquisition in neuroanatomical MRI. *Magnetic Resonance in Medicine*, *68*(2), 389–399. https://doi.org/10.1002/mrm.23228

Tustison, N. J., Avants, B. B., Cook, P. A., Zheng, Y., Egan, A., Yushkevich, P. A., & Gee, J. C. (2010). N4ITK: Improved N3 bias correction. *IEEE Transactions on Medical Imaging*, *29*(6), 1310–1320. https://doi.org/10.1109/TMI.2010.2046908

Uppenkamp, S., & Röhl, M. (2014). Human auditory neuroimaging of intensity and loudness. *Hearing Research*, *307*, 65–73. https://doi.org/10.1016/j.heares.2013.08.005

van Dijk, J. A., de Haas, B., Moutsiana, C., & Schwarzkopf, D. S. (2016). Intersession reliability of population receptive field estimates. *NeuroImage*, *143*, 293–303. https://doi.org/10.1016/j.neuroimage.2016.09.013

van Es, D. M., van der Zwaag, W., & Knapen, T. (2019). Topographic maps of visual space in the human cerebellum. *Current Biology*, *29*(10), 1689–1694.e3. https://doi.org/10.1016/j.cub.2019.04.012

Van Essen, D. C., Newsome, W. T., & Maunsell, J. H. (1984). The visual field representation in striate cortex of the macaque monkey: Asymmetries, anisotropies, and individual variability. *Vision Research*, *24*(5), 429–448. https://doi.org/10.1016/0042-6989(84)90041-5

Vanni, S., Henriksson, L., & James, A. (2005). Multifocal fMRI mapping of visual cortical areas. *NeuroImage*, *27*(1), 95–105. https://doi.org/10.1016/j.neuroimage.2005.01.046

Veraart, C., De Volder, A., Wanet-Defalque, M., Bol, A., Michel, C., & Goffinet, A. (1990). Glucose utilization in human visual cortex is abnormally elevated in blindness of early onset but decreased in blindness of late onset. *Brain Research*, *510*(1), 115–121. https://doi.org/10.1016/0006-8993(90)90735-T

Victor, J. D., Purpura, K., Katz, E., & Mao, B. (1994). Population encoding of spatial frequency, orientation, and color in macaque V1. *Journal of Neurophysiology*, *72*(5), 2151–2166. https://doi.org/10.1152/jn.1994.72.5.2151

Voss, P., & Zatorre, R. J. (2011). Occipital cortical thickness predicts performance on pitch and musical tasks in blind individuals. *Cerebral Cortex*, *22*(11), 2455–2465. https://doi.org/10.1093/cercor/bhr311

Wan, C. Y., Wood, A. G., Reutens, D. C., & Wilson, S. J. (2010). Early but not late-blindness leads to enhanced auditory perception. *Neuropsychologia*, *48*(1), 344–348. https://doi.org/10.1016/j.neuropsychologia.2009.08.016

Wandell, B. A., Dumoulin, S. O., & Brewer, A. A. (2007). Visual field maps in human cortex. *Neuron*, *56*(2), 366–383. https://doi.org/10.1016/j.neuron.2007.10.012

Wandell, B. A., & Winawer, J. (2015). Computational neuroimaging and population receptive fields. *Trends in Cognitive Sciences*, *19*(6), 349–357. https://doi.org/10.1016/j.tics.2015.03.009

Wanet-Defalque, M.-C., Veraart, C., De Volder, A., Metz, R., Michel, C., Dooms, G., & Goffinet, A. (1988). High metabolic activity in the visual cortex of early blind human subjects. *Brain Research*, *446*(2), 369–373. https://doi.org/10.1016/0006-8993(88)90896-7

Wang, L., Zhang, Z., Okada, T., Li, C., Chen, D., Funahashi, S., Wu, J., & Yan, T. (2021). Population receptive field characteristics in the between- and within-digit dimensions of the undominant hand in the primary somatosensory cortex. *Cerebral Cortex*, *31*(10), 4427–4438. https://doi.org/10.1093/cercor/bhab097

Watkins, K. E., Shakespeare, T. J., O'Donoghue, M. C., Alexander, I., Ragge, N., Cowey, A., & Bridge, H. (2013). Early auditory processing in area V5/MT+ of the congenitally blind brain. *Journal of Neuroscience*, *33*(46), 18242–18246. https://doi.org/10.1523/JNEUROSCI.2546-13.2013

Weaver, K., Richards, T., Saenz, M., Petropoulos, H., & Fine, I. (2013). Neurochemical changes within human early blind occipital cortex. *Neuroscience*, *252*, 222–233. https://doi.org/10.1016/j.neuroscience.2013.08.004

Wessinger, C. M., Buonocore, M. H., Kussmaul, C. L., & Mangun, G. R. (1997). Tonotopy in human auditory cortex examined with functional magnetic resonance imaging. *Human Brain Mapping*, *5*(1), 18–25. https://doi.org/10.1002/(SICI)1097-0193(1997)5:1<18::AID-HBM3>3.0.CO;2-Q

Woods, D. L., Stecker, G. C., Rinne, T., Herron, T. J., Cate, A. D., Yund, E. W., Liao, I., & Kang, X. (2009). Functional maps of human auditory cortex: Effects of acoustic features and attention. *PLOS ONE*, *4*(4), 1–19. https://doi.org/10.1371/journal.pone.0005183

Zeidman, P., Silson, E. H., Schwarzkopf, D. S., Baker, C. I., & Penny, W. (2018). Bayesian population receptive field modelling. *NeuroImage*, *180*, 173–187. https://doi.org/10.1016/j.neuroimage.2017.09.008

Zhang, Y., Brady, M., & Smith, S. (2001). Segmentation of brain MR images through a hidden Markov random field model and the expectation-maximization algorithm. *IEEE Transactions on Medical Imaging*, *20*(1), 45–57. https://doi.org/10.1109/42.906424

Zhou, J., Benson, N. C., Kay, K. N., & Winawer, J. (2018). Compressive temporal summation in human visual cortex. *Journal of Neuroscience*, *38*(3), 691–709. https://doi.org/10.1523/JNEUROSCI.1724-17.2017

Zuiderbaan, W., Harvey, B. M., & Dumoulin, S. O. (2012). Modeling center–surround configurations in population receptive fields using fMRI. *Journal of Vision*, *12*(3), 10–10. https://doi.org/10.1167/12.3.10

Appendix A

SUBJECT INFORMATION TABLES

Appendix A contains subject information tables.

Subject No.	Sex	Location	Stimuli	Age (yr)	Clinical Description
EB01	Male	University of Washington	Stationary/ moving	32	Leber's congenital amaurosis, low light perception
EB02	Female	University of Washington	Stationary/ moving	38	Retinopathy of prematurity, no light perception in right eye, minimal peripheral light perception in left eye, 3 months premature
EB03	Female	University of Washington	Stationary/ moving	55	Retinopathy of prematurity, low light perception until retina detached at age 25, 2 months premature
EB04	Male	University of Washington	Stationary/ moving	52	Congenital glaucoma, no light perception
ANO1	Male	Oxford	Moving	36	Isolated bilateral anophthalmia
ANO2	Female	Oxford	Moving	39	Isolated bilateral anophthalmia
ANO3	Male	Oxford	Moving	26	Isolated bilateral anophthalmia
ANO5	Male	Oxford	Moving	30	Isolated bilateral anophthalmia
ANO6	Male	Oxford	Moving	31	Isolated bilateral anophthalmia

Table A.1: Chaper 3 Subject demographics and clinical descriptions

Subject	Left Hemisphere						Right Hemisphere					
No.	δ	α_1	α_2	β_1	β_2	c	δ	α_1	α_2	β_1	β_2	c
01	0.0047	1.3653	5.0776	0.3717	0.4271	1.3653	0.0037	1.4028	3.8913	0.5937	0.3376	1.4028
02	0.0046	1.6035	6.9897	0.4777	0.5818	1.6035	0.0041	1.4915	5.0853	0.5764	0.4429	1.4915
03	0.0048	1.5692	3.6149	0.5675	0.3116	1.5692	0.0044	1.5301	3.6024	0.5746	0.3261	1.5301
04	0.0079	1.5958	3.8405	0.2309	0.2745	1.5958	0.0071	1.7038	4.8951	0.2030	0.3220	1.7038
05	0.0037	1.3728	3.1016	0.6462	0.2847	1.3728	0.0035	1.5385	4.7842	0.3441	0.3933	1.5385
06	0.0062	1.4754	7.8398	0.2812	0.6062	1.4754	0.0045	1.5884	7.3543	0.3091	0.6103	1.5884
07	0.0039	1.4236	9.1731	0.2860	0.5649	1.4236	0.0047	1.3320	7.6656	0.2923	0.4819	1.3320
08	0.0060	1.6475	5.6016	0.2212	0.4002	1.6475	0.0057	1.5671	5.2267	0.2317	0.3646	1.5671
09	0.0041	1.4831	3.3762	0.6410	0.2818	1.4831	0.0018	1.9397	8.0992	0.4394	0.6322	1.9397
10	0.0039	1.2469	3.3498	0.6188	0.2474	1.2469	0.0034	1.3286	4.3091	0.5444	0.3472	1.3286
11	0.0035	1.4483	9.4080	0.3173	0.5580	1.4483	0.0046	1.3380	6.5470	0.3280	0.4046	1.3380
12	0.0055	1.4504	6.8744	0.2674	0.4464	1.4504	0.0058	1.4199	6.0276	0.2676	0.3759	1.4199

Table A.2: Subject HRF parameters for Chaper 4

Appendix B

ANOVA TABLES

Appendix B contains full ANOVA tables for the statistics calculated in Chapter 4.

		Polar Angle				Eccentricity			
	df	*MS*	*F*	*p*	η^2	*MS*	*F*	*p*	η^2
Hemisphere	1	0.0048	0.0246	0.8756	0.0000	0.0004	0.0042	0.9485	0.0000
Stimulus	1	6.2675	32.0187	< 0.0001	0.0428	1.2841	15.0649	0.0001	0.0114
ROI	3	28.6360	146.2925	< 0.0001	0.5867	29.4537	345.5603	< 0.0001	0.7847
Hemi.×Stim.	1	1.8626	9.5155	0.0024	0.0127	0.0282	0.3309	0.5659	0.0003
Hemi.×ROI	3	0.0534	0.2726	0.8451	0.0011	0.0282	0.3031	0.8231	0.0007
Stim.×ROI	3	0.2667	1.3623	0.2562	0.0055	0.7954	9.3316	< 0.0001	0.0212
Hemi.×Stim.×ROI	3	0.0860	0.4393	0.7252	0.0018	0.0125	0.1472	0.9314	0.0003
Error	165	0.1957				0.0852			

	pRF Size			
	df	*MS*	*F*	*p*	η^2
Hemisphere	1	0.0332	0.5987	0.4402	0.0007
Stimulus	1	5.8963	106.2833	< 0.0001	0.1211
ROI	3	7.8382	141.2880	< 0.0001	0.4830
Hemi.×Stim.	1	0.0055	0.0986	0.7539	0.0001
Hemi.×ROI	3	0.0525	0.9468	0.4195	0.0032
Stim.×ROI	3	0.6909	12.4545	< 0.0001	0.0426
Hemi.×Stim.×ROI	3	0.0371	0.6692	0.5721	0.0023
Error	165	0.0555			

Table B.1: Intersession reliability of pRF estimates ANOVA table

		Number of Estimated pRFs			
	df	*MS*	*F*	*p*	η^2
Hemisphere	1	4991.9000	0.0444	0.8333	0.0000
Stimulus	1	5992180.0052	53.3137	< 0.0001	0.0270
ROI	3	60876049.2691	541.6269	< 0.0001	0.8228
Hemi.×Stim.	1	804.4219	0.0072	0.9327	0.0000
Hemi.×ROI	3	252410.2552	2.2457	0.0849	0.0034
Stim.×ROI	3	13229.0469	0.1177	0.9496	0.0002
Hemi.×Stim.×ROI	3	14848.3524	0.1321	0.9409	0.0002
Error	165	112394.8113			

Table B.2: Number of estimated pRFs ANOVA table

		Polar Angle				Eccentricity			
	df	*MS*	*F*	*p*	η^2	*MS*	*F*	*p*	η^2
Hemisphere	1	120.8881	0.4459	0.5063	0.0046	0.0604	8.0386	0.0058	0.0322
ROI	3	746.0852	2.7523	0.0483	0.0855	0.2280	30.3408	< 0.0001	0.3642
Hemi.×ROI	3	51.5676	0.1902	0.9028	0.0059	0.0152	2.0217	0.1178	0.0243
Error	77	271.0817				0.0075			

		pRF Size				Variance Explained			
	df	*MS*	*F*	*p*	η^2	*MS*	*F*	*p*	η^2
Hemisphere	1	0.0780	7.0569	0.0096	0.0333	0.0010	1.9813	0.1633	0.0059
ROI	3	0.2803	23.3607	< 0.0001	0.3589	0.0249	50.1947	< 0.0001	0.4466
Hemi.×ROI	3	0.0496	4.4849	0.0059	0.0635	0.0003	0.5402	0.6562	0.0048
Error	77	0.0111				0.0005			

Table B.3: Difference in pRF estimates (fixed-bar – log-bar) ANOVA table

		a				***b***			
	df	*MS*	*F*	*p*	η^2	*MS*	*F*	*p*	η^2
Hemisphere	1	0.0080	0.3511	0.5543	0.0015	0.0840	5.9680	0.0156	0.0123
Stimulus	1	0.0374	1.6512	0.2006	0.0072	2.1331	151.5007	< 0.0001	0.3111
ROI	3	0.1908	8.4201	< 0.0001	0.1105	0.0998	7.0913	0.0002	0.0437
Hemi.×Stim.	1	0.0457	2.0177	0.1574	0.0088	0.0608	4.3213	0.0392	0.0089
Hemi.×ROI	3	0.0125	0.5514	0.6479	0.0072	0.0550	3.9090	0.0099	0.0241
Stim.×ROI	3	0.0705	3.1121	0.0279	0.0409	0.0311	2.2092	0.0890	0.0136
Hemi.×Stim.×ROI	3	0.0411	1.8122	0.1469	0.0238	0.0545	3.8683	0.0105	0.0238
Error	165	0.0227				0.0141			

		pRF size at 1°			
	df	*MS*	*F*	*p*	η^2
Hemisphere	1	0.0403	1.6197	0.2049	0.0038
Stimulus	1	2.7356	110.0205	< 0.0001	0.2612
ROI	3	0.5109	20.5456	< 0.0001	0.1463
Hemi.×Stim.	1	0.0011	0.0434	0.8353	0.0001
Hemi.×ROI	3	0.0164	0.6612	0.5770	0.0047
Stim.×ROI	3	0.1940	7.8040	0.0001	0.0556
Hemi.×Stim.×ROI	3	0.0038	0.1515	0.9286	0.0011
Error	165	0.0249			

Table B.4: pRF size equation parameters by eccentricity and pRF size at 1° ANOVA table

		c				***d***			
	df	*MS*	*F*	*p*	η^2	*MS*	*F*	*p*	η^2
Hemisphere	1	0.0068	1.8059	0.1808	0.0068	0.0015	1.0462	0.3079	0.0023
Stimulus	1	0.0143	3.7945	0.0531	0.0143	0.3263	226.6941	< 0.0001	0.4999
ROI	3	0.0821	21.8163	< 0.0001	0.2465	0.0109	7.5944	0.0001	0.0502
Hemi.×Stim.	1	0.0009	0.2293	0.6327	0.0009	0.0051	3.5140	0.0626	0.0077
Hemi.×ROI	3	0.0081	2.1602	0.0947	0.0244	0.0015	1.0270	0.3822	0.0068
Stim.×ROI	3	0.0059	1.5616	0.2007	0.0176	0.0037	2.5728	0.0559	0.0170
Hemi.×Stim.×ROI	3	0.0002	0.0664	0.9777	0.0008	0.0011	0.7794	0.5070	0.0052
Error	165	0.0038				0.0014			

		CMF at 1°			
	df	*MS*	*F*	*p*	η^2
Hemisphere	1	0.2656	0.0724	0.7882	0.0002
Stimulus	1	413.0927	112.5906	< 0.0001	0.3309
ROI	3	17.9231	4.8850	0.0028	0.0431
Hemi.×Stim.	1	1.5462	0.4214	0.5171	0.0012
Hemi.×ROI	3	6.8236	1.8598	0.1384	0.0164
Stim.×ROI	3	3.7683	1.0271	0.3822	0.0091
Hemi.×Stim.×ROI	3	0.8284	0.2258	0.8784	0.0020
Error	165	3.6690			

Table B.5: CMF equation parameters by eccentricity and CMF size at 1° ANOVA table